

ANALYSIS AND DESIGN OF MICROWAVE DEVICES
BASED ON RIDGE GAP WAVEGUIDE TECHNOLOGY

SHOKRY I. SHAMSELDIN

A THESIS
IN
THE DEPARTMENT
OF
ELECTRICAL AND COMPUTER ENGINEERING

PRESENTED IN PARTIAL FULFILLMENT OF THE REQUIREMENTS
FOR THE DEGREE OF DOCTOR OF PHILOSOPHY
CONCORDIA UNIVERSITY
MONTRÉAL, QUÉBEC, CANADA

AUGUST 2016

© SHOKRY I. SHAMSELDIN, 2016

CONCORDIA UNIVERSITY
School of Graduate Studies

This is to certify that the thesis prepared

By: **Mr. Shokry I. Shamseldin**

Entitled: **Analysis and Design of Microwave Devices based on
Ridge Gap Waveguide Technology**

and submitted in partial fulfillment of the requirements for the degree of

Doctor of Philosophy (Electrical and Computer Engineering)

complies with the regulations of this University and meets the accepted standards
with respect to originality and quality.

Signed by the final examining committee:

Dr. Yahia Antar _____ External Examiner
Dr. Abdel Razik Sebak _____ Examiner
Dr. Robert Paknys _____ Examiner
Dr. Amr Yousef _____ Examiner
Dr. Ahmed A. Kishk _____ Supervisor

Approved _____
Chair of Department or Graduate Program Director

_____ July, 11, 2016 _____

Amir Asif, Ph.D., ing., Dean
Faculty of Engineering and Computer Science

Abstract

Analysis and Design of Microwave Devices based on Ridge Gap Waveguide Technology

Shokry I. Shamseldin, Ph.D.

Concordia University, 2016

The usage of high frequency microwave devices is rapidly increasing with the advances achieved in the communication systems. However, the standard guiding structures have high losses such as microstrip technology, or difficulty in manufacturing such as in the case of waveguides. The newly developed ridge gap waveguide (RGW) technology resolves the problems above as it has low losses and does not require electrical contacts as required in the waveguides. The concept of RGW is simple as it allows the wave propagations in the guiding part and eliminates the leakage in all other directions. The region that surrounds the ridge consists of two parallel surfaces; one is a perfect electric conductor (PEC) and the second is a perfect magnetic conductor (PMC). The gap between the two surfaces should be less than a quarter wavelength. Periodic conducting nails realize the PMC that practically has a possible bandwidth 2.5:1 and in some cases exceeds 3:1. Usually, the design of these surfaces relies on the unit cell analysis that is based on determining its band gap, the estimation of the band gap is performed numerically. The band gap of the cell is the operating bandwidth of the complete structure. For the first time, we presented a method to measure the band gap from s-parameter measurements. Utilization of the broadband characteristics strongly depends on the proper design of the transition between the RGW and the standard guiding structures and connectors. Most of the available transitions make use of around one-third of the possible bandwidth. Therefore, we present new transitions

that utilize the whole possible bandwidth of the RGW. The presented work can be divided into four major parts. Several microwave components are designed based on the RGW such as power divider, hybrid couplers, and a circulator. New methods are presented for efficient and accurate design of these components. One of the main contributions is related to the RGW circulator design; it's an accurate design procedure that can be used with other technologies as well. In addition, a new setup to measure the low relative permittivity of thin materials such as fabrics is presented. An example of a leaky wave antenna using split slot arrays is presented. These studies highlight the RGW advantages and can be considered as a step towards the standardization of this technology.

Acknowledgments

I would like to express my deep gratitude to my supervisor, Dr. Ahmed A. Kishk for his guidance, patience and invaluable comments.

Thanks are also due to Dr. Yahia Antar, Dr. Robert Paknys, Dr. Abdel Razik Sebak and Dr. Amr Youssef for their priceless comments and serving in my examining committee.

I would also like to thank Scientific Microwave Corporation staff, Prof. Abdelmegeid, Eng. Mohamed, Eng. Gada, Eng. Kamal and Chris for their assistance to build and measure the presented prototypes in this work.

I express my regards and blessings to my mother, my father and my sister for their limitless support during the compilation of this work.

Lastly, I offer my love to my small family Sara, Sama and Hana for their moral support in this journey.

Contents

List of Figures	x
List of Tables	xvii
List of Acronyms	xviii
List of Symbols	xx
1 Introduction	1
1.1 Historical Overview	1
1.2 Traditional Guiding Structures	2
1.3 Modern Guiding Structures	3
1.4 Periodic Structures	4
1.4.1 Soft and Hard Surfaces	4
1.4.2 Electromagnetic Band Gap structures	5
1.5 Ridge Gap Waveguide Structure	6
1.5.1 RGW Cell Analysis	8
1.5.2 The Field Distribution Along the Line	9
1.5.3 Excitation Mechanisms in Literature	10
1.6 Objectives	13
1.7 List of Contributions	14
1.8 Thesis Organization	15

2	Ridge Gap Waveguide Excitation	16
2.1	RGW Transitions For Airborne Radar Applications	16
2.2	Coaxial Line to RGW Transition	17
2.2.1	Coaxial to Ridge Gap Waveguide Direct Transition	17
2.2.2	Wideband Coaxial to Ridge Gap Waveguide Transitions	19
2.2.3	Testing the Wideband Transition	31
2.2.4	The Ridge Gap Waveguide Fed by the Proposed Transition	31
2.2.5	Experimental Validation	33
2.3	MSL to RWG Transition	37
2.3.1	The Transition Design	39
2.3.2	The Perforated Substrates Design Procedure and Verification	43
2.4	RGW Measurement Setup	46
3	RGW cell analysis and BW enhancement	47
3.1	RGW Cell Dispersion Relation in the Literature	48
3.1.1	Dispersion Relation Extraction Algorithm	50
3.1.1.1	DUT Under Single Mode Operation Conditions	50
3.1.1.2	DUT under Multi-Mode Operation Conditions	54
3.1.2	Procedure Validation on Bench-Mark Examples	56
3.1.2.1	Example1: Parallel Plate Waveguide	56
3.1.2.2	Example2: Rectangular Waveguide	57
3.1.3	Ridge Gap Waveguide Cells Dispersion Relation	61
3.1.3.1	The Multi-Mode Band Results Interpretations	64
3.1.4	Measurement Results of the RGW Dispersion Relation	65
3.1.5	Utilizing the Dispersion Relation in the RGW Design	68
3.2	Ridge Gap Waveguide Bandwidth	72
3.2.1	The Realized Bandwidth Vs the Possible Bandwidth	73
3.2.2	Gap Height Effect on RGW Bandwidth	75

3.2.2.1	The Dual Gap Height RGW	80
3.2.2.2	Nail Connected RGW Configuration "Ridge Waveguide with Periodic Walls"	83
3.2.3	Measurements Results	86
3.3	Bandwidth evaluation of RGW components	87
4	Reciprocal Devices Based on RGW Technology	91
4.1	WideBand Power Divider Based on RGW	91
4.1.1	RGW Unit Cell Analysis	92
4.1.2	Power Divider Design	93
4.2	RGW 3-dB Hybrid Coupler	94
4.2.1	Hybrid Coupler Mathematical Formulation & Empirical Design Equations	96
4.2.2	RGW Hybrid Coupler Design Procedure	99
4.2.2.1	The Ideal Model with PMC Surface	99
4.2.2.2	The Realized Structures with Periodic Cells	100
4.2.3	The Experimental Validation	102
4.3	RGW Passive Components Summary	109
5	Non-Reciprocal Devices Based on RGW Technology	110
5.1	Introduction	110
5.2	Junction Circulator Mathematical Formulations	111
5.2.1	The Ferrite Disc Field Distribution	111
5.2.2	The Junction Network Representations	115
5.3	The RGW Circulator Design	119
5.3.1	RGW Circulator with Ideal Boundary Conditions	121
5.3.2	RGW Circulator Realization with Periodic Cells	122
5.4	Summary of the Introduced Components	127

6	Applications of Ridge Gap Waveguide Devices	128
6.1	Textile Material Characterization using RGW Technology	128
6.1.1	The Measurement Setup Description	131
6.1.2	The Proposed Algorithm Mathematical Formulations	132
6.1.3	The Tolerance Analysis of the Proposed Algorithm	136
6.1.4	The Relation Between the Effective and the Relative Permittivity	140
6.1.5	The Operating Bandwidth of ϵ_r Measurement	142
6.1.6	The Proposed Algorithm Validation	143
6.1.7	The Relative Permittivity Extraction in Textile Materials . . .	146
6.1.8	The Uncertainty in the Measured Results	154
6.2	Leaky-wave Antenna Array Fed by RGW	156
6.2.1	Magic Tee Design	156
6.2.2	Ridge Gap Waveguide Analysis	156
6.2.3	The Leaky Wave Slot Array	159
7	Conclusion and Future Work	163
	Bibliography	165

List of Figures

1.1	Soft and hard surfaces with respect to the wave propagation direction.	6
1.2	RGW vertical coaxial excitation mechanism in different views.	8
1.3	(a) The unit cell structure (b) The corresponding dispersion relation.	9
1.4	The field distribution in the RGW at different frequencies.	10
1.5	RGW vertical coaxial excitation mechanism (a)3D view (b)Top view.	12
1.6	The scattering parameters of the vertical coaxial to RGW transition.	13
2.1	The 3D structure of the direct transition with open circuit termination.	19
2.2	The direct transition from coaxial line to ridge gap waveguide (a) Open circuit terminated (b) Short circuit terminated (c) The S-parameters.	20
2.3	(a) The simulated model of ridge gap waveguide excited via wave ports (b) The S-parameters.	22
2.4	A schematic of the first part of the transition. (a)Side view. (b) Front view.	26
2.5	Part 1: 2.92 to single ridge waveguide transition (a) 3D view (b) Side view cross section.	27
2.6	Part1: 2.92 to single ridge waveguide transition (a) Internal dimensions (b) S-parameters.	28
2.7	Part2: The fitting section two face dimensions.	29
2.8	The S-parameters of the fitting section alone with different values of L_{tr} (transition length).	30

2.9	The scattering parameters of the wideband coaxial to ridge with the fitting part.	30
2.10	The comparison between different conducting material in fabricating the transition in terms of S_{21} (dB).	32
2.11	The dispersion relation of the bed nail unit cell used to build up the ridge gap waveguide.	34
2.12	The RGW final structure's scattering parameters fed by a single ridge waveguide.	34
2.13	The normalized field distribution of different frequencies within the operating bandwidth normal to the ridge.	35
2.14	The internal configuration of the fabricated connector.	36
2.15	The scattering parameters of the double transition.	36
2.16	(a) The complete structure after assembly. (b) The measurement setup.	38
2.17	The S-parameters comparison for the whole structure.	39
2.18	The dispersion relation of the double cone back to back unit cell.	41
2.19	The transition between microstrip Line and ridge gap waveguide (a) Side view (b) 3D view.	42
2.20	The scattering parameters of the transition in the ideal case.	42
2.21	The relation between effective relative permittivity and the hole Diameter.	44
2.22	The extracted relative permittivity using the parallel plate model.	45
2.23	The scattering parameters of the final transition design with perforated substrate.	45
3.1	The DUT block diagram.	52
3.2	The parallel plate example block diagram.	57
3.3	Scattering parameters of the parallel plate example.	58
3.4	The parallel plate example: dispersion relation.	58

3.5	The rectangular waveguide example block diagram.	59
3.6	Scattering parameters the rectangular waveguide example.	60
3.7	The rectangular waveguide example: dispersion relation.	60
3.8	The cell configuration (a) Side view (b) 3D view.	62
3.9	The measurement setup for BNUCs testing.	63
3.10	The scattering parameters of the BNUCs inside a rectangular waveguide.	63
3.11	The comparison between the dispersion relations extracted by the proposed method and the eigenmode solution.	64
3.12	The field distribution of Mode 2.	65
3.13	The field distribution of Mode 3.	66
3.14	The field distribution inside the structure.	66
3.15	The measurement setup to extract the RGW dispersion relation.	68
3.16	Comparison between the measured and the simulated scattering parameters.	69
3.17	Comparison between the extracted experimentally and the simulated dispersion relation.	69
3.18	Straight ridge gap waveguide.	70
3.19	The scattering parameters of a straight RGW.	71
3.20	The field distribution over a cross section of the straight ridge gap waveguide.	71
3.21	The squared cross section bed nail unit cell (a) 3D structure (b) Front view. The cone shaped unit cell (c) 3D structure (d) Front view.	75
3.22	The dispersion relation of (a) Square cross-sectional unit cell. (b) Cone shaped unit cell. (c) Square cross-sectional unit cell with the ridge. (d) Cone shaped unit cell with the ridge.	76

3.23	The dispersion relation of (a) Zero base cone shape unit cell. (b) Zero base cone shape unit cell with the ridge.	76
3.24	The printed cone cell (a) 3D structure. (b) Front view. (c) Unit cell dispersion relation. (d) The dispersion relation in the presence of the ridge.	77
3.25	The grounded printed cone cell (a) 3D structure. (b) Front view. (c) Unit cell dispersion relation. (d) The dispersion relation in the presence of the ridge.	78
3.26	The relation between the bandwidth ratio and the gap height for four different cells.	80
3.27	The relation between the bandwidth ratio and the gap height for four different cells in the presence of the ridge.	81
3.28	(a) Front view of the traditional RGW. (b) Front view of the dual gap height RGW.	82
3.29	The relation between the bandwidth ratio and the gap height for four different cells in the dual gap height RGW.	82
3.30	The zero gap height RGW (a) Front view. (b) 3D structure. (c) Unit cell dispersion relation. (d) The dispersion relation in the presence of the ridge.	85
3.31	The fabricated transition between coaxial connector and RGW.	88
3.32	The dispersion relation of the grounded printed cone unit cell in the presence of the ridge.	88
3.33	The fabricated straight RGW lines (a) The traditional square cross sectional unit cell. (b) The grounded printed cone unit cell.	89
3.34	The scattering parameters of a straight line of a ridge gap waveguide (a) Surrounded by the square cross-sectional traditional cells. (b) Surrounded by grounded printed cone unit cells.	90

4.1	The AMC unit cell (a) Cross section view, (b) 3D view, and (c) Dispersion relation.	92
4.2	Power Divider configuration (a) Top view. (b) 3D structure (c) The configuration with the feeding structure.	94
4.3	The scattering parameters of the power divider fed by the MSL to RGW transition.	95
4.4	The short slot rectangular waveguide hybrid coupler (a) 3D view (b) 3D sectional view.	98
4.5	The RGW hybrid coupler with ideal boundary conditions (a) Structure top view. (b) Simulated scattering parameters.	101
4.6	The unit cell (a) Front view. (b) 3D structure (c) Dispersion relation.	103
4.7	The simulated RGW hybrid coupler (a)3D model upper ground is removed (b) Scattering parameters.	104
4.8	The measurement setup components (a) The custom through. (b) Coax to single ridge transition. (c) Single ridge matched load.	105
4.9	The Coaxial to RGW transition (a) Connected back to back (b) Back to back measured scattering parameters.	106
4.10	The matched load evaluation (a) Measurement setup. (b) Scattering parameters.	107
4.11	The final RGW hybrid coupler (a) measurement setup (b) comparison of the simulated response.	108
5.1	A schematic for the junction circulator.	118
5.2	The simulated model of the RGW circulator.	123
5.3	The comparison between the analytical and the simulated response of the RGW circulator with ideal PMC around the ridge. (a) Design example 1. (b) Design example 2.	124

5.4	The unit cell (a)Front view. (b) 3D view. (c) Cell 1 dispersion relation. (c) Cell 1 dispersion relation.	125
5.5	The realized RGW circulator (a) 3D structure. (b) Design 1 scattering parameters. (b) Design 2 scattering parameters.	126
6.1	The simulated model of the complete setup (a) Cross section. (b) 3D model.	132
6.2	The SUT block diagram.	133
6.3	The error in the relative permittivity with both the material conduc- tivity and the measurement frequency.	139
6.4	The RGW dimensions.	141
6.5	The relation between the effective and the relative permittivities. . .	142
6.6	The dispersion relation of an air filled RGW in the existence of the ridge.	144
6.7	The dispersion relation of a partially filled RGW in the existence of the ridge ($\varepsilon_r = 2$).	144
6.8	The dispersion relation of a partially filled RGW in the existence of the ridge ($\varepsilon_r = 3$).	145
6.9	The setup validation model.	147
6.10	The scattering parameters of dielectric filled RGW between two air filled RGWs.	147
6.11	The extracted dispersion relation of three standard substrates. . . .	148
6.12	The customized TRL calibration kit parts.	148
6.13	The measurement setup with a sample under the test of RO5880 LZ substrate.	149
6.14	Comparison between the simulated & measured scattering parameters of a partially filled RGW with 5880LZ substrate.	149
6.15	The dispersion relation extracted through the measurement setup. . .	150

6.16	The textile samples under test.	151
6.17	The measurement setup with the textile samples.	152
6.18	The measurement setup of the textile material.	152
6.19	The scattering parameters of a partially filled RGW with two different samples of textile materials.	153
6.20	The dispersion relation extracted through the measurement setup for two textile material samples.	153
6.21	The extracted relative permittivities of the textile material samples Vs frequency.	154
6.22	The structure of the magic tee component.	157
6.23	The magic tee scattering parameters.	157
6.24	The unit cell dispersion diagram.	158
6.25	The RGW fed by the magic tee (a) 3D structure (b) The field distribution.	159
6.26	The leaky wave slot (a)3D structure (b)Field distribution.	160
6.27	The radiation pattern for the whole leaky-wave slot array.	160
6.28	The return loss and the array gain vs frequency.	160
6.29	The radiation pattern in E-plane.	161
6.30	The radiation pattern in E-plane.	161
6.31	The radiation pattern in E-plane.	162
6.32	The radiation pattern in E-plane.	162

List of Tables

2.1	The final dimensions of the matching network sections in millimeters.	25
2.2	The wideband short circuit dimensions in millimeters.	26
2.3	The final dimensions of both matching sections	45
3.1	The bed nail unit cell dimensions.	63
3.2	The unit cell dimensions of the ridge gap waveguide.	75
3.3	The dimensions of the nail connected ridge gap waveguide.	86
4.1	RGW unit cell dimension.	93
4.2	The dimensions of the RGW hybrid coupler with ideal PMC boundaries.	100
4.3	The dimensions of the unit cell.	102
5.1	Permeability tensor important expressions	116
5.2	The bed of nail unit cell dimensions.	123
6.1	The available RGW dimensions in the lab.	141
6.2	The dimensions of the unit cell design	158

List of Acronyms

1D	One-Dimensional
3D	Three-Dimensional
ADS	Advanced Design System
AMC	Artificial Magnetic Conductor
BNUC	Bed Nail Unit Cell
BW	Bandwidth
CST MWS	Computer Simulation Technology Microwave Studio
DUT	Device Under Test
EBG	Electromagnetic Band Gap
EM	Electromagnetic
FEM	Finite Element Method
FDTD	Finite Difference Time Domain
FIT	Finite Integration Technique
FSS	Frequency Selective Structure
HFSS	High Frequency Structure Simulator
IEEE	Institute of Electrical and Electronics Engineers
MSL	Microstrip Line
PMC	Perfect Magnetic Conductor
RGW	Ridge Gap Waveguide
Rx	Receiver
TEM	Transverse Electromagnetic Wave

TE	Transverse Electric Wave
TM	Transverse Magnetic Wave
Tx	Transmitter

List of Symbols

ε_r	Relative permittivity of dielectric
σ	Electric conductivity
Z_s	Surface impedance
S	Siemens
Ω	Ohm
D	Antenna directivity
G	Antenna gain
λ	Wavelength
η_0	Intrinsic impedance of free-space
S	S-parameter
$\tan \delta$	Loss tangent
j	$\sqrt{-1}$
ω	Angular frequency
f_0	Resonance frequency of the unloaded resonator
Q_0	Unloaded quality factor
Q_a	Quality factor of the antenna
Q_w	Quality factor of the antenna inside the Wheeler cap
Γ_a	Reflection coefficient of the antenna in free-space

Chapter 1

Introduction

1.1 Historical Overview

Guiding structures of microwave signals are always one of the most challenging topics in the RF microwave field of research. Although the basic ideas of the guiding structures are discussed, almost, along with the introduction of Maxwell equations in the 19th century, but the advances in the communication systems generally and in the microwave engineering especially always demand enhancements to overcome the limitations of the existing structures or presenting new types. In 1864, James Clerk Maxwell observed that electromagnetic disturbance travels with the speed of light. Maxwell introduced twenty equations involving twenty variables. These equations summarized the work of Hans C. Oersted, Carl F. Gauss, Andre M. Ampere, Michael Faraday and others. Maxwell not only summarized the contributions of these scientists, but also added the concept of displacement current to complete the theory. Maxwell's original equations were modified by Heinrich Hertz to be four equations involving four variables. Oliver Heaviside then introduced these equations in vector form. Hertz proved the predictions of Maxwell experimentally and these brilliant experiments managed to obtain the universal acceptance of this theory. After this

verification, the primary principles of the wave propagation inside guided and unguided structures were well established [1, 2]. Based on these four equations, the wave equations were directly obtained by Helmholtz in 1886. The wave equations are second order differential equations that bound the electric field and the magnetic field behavior inside any structure. Solving these differential equations and applying the boundary conditions of the structure will result in a full description of the electric field and the magnetic field inside this structure, which will be presented as a summation of TE, TM, TEM and hybrid modes inside the structure. This solution is addressed in hundreds of references in many different structures like parallel plate waveguide, rectangular waveguides, circular waveguides, etc. [3]. The transmission lines are a subgroup of the guiding structure in which the TEM mode can propagate. The TEM mode has no intramodal dispersion, which is preferred in communication systems.

1.2 Traditional Guiding Structures

The term "microwave frequencies" is used to describe the frequency range of 300 MHz to 300 GHz. In the MHz range of frequencies, transmission lines are preferred to be used as they carry the signal in the form of TEM waves. The TEM mode is not subjected to any dispersion, which gives this mode a great advantage. Moreover, the TEM mode has a cutoff frequency of zero Hertz, which enables this mode to carry any signal at any frequency. As the carrier frequency increases the losses in the transmission lines increase. This leads to the use of other types of guiding structures such as waveguides. Although these types of guiding structures do not support the TEM mode (except the coaxial transmission lines), but they have much lower losses. The lower losses enable these types of guiding structures to be used in higher frequency ranges. The major disadvantage of these waveguides is the dependency on

TE (most likely) as a dominant mode, which is subjected to intra-modal dispersion. The bandwidth of these waveguides is limited to the stable band. The stable band is the frequency band between the cutoff frequency of the dominant mode and the cutoff frequency of the next higher order mode. It is important to mention that, typically, the practical operating bandwidth should start higher than the lowest mode and less than the next higher order mode to have some safety factors. It is important to operate far from the cutoff frequency of both modes. This safety factor will ensure neither having an evanescent mode nor having propagating higher order mode.

1.3 Modern Guiding Structures

A lot of guiding structures are addressed in the microwave applications. The microstrip lines and the coplanar waveguides are examples for the substrate printed guided structures. Being easy in fabrication as well as their low cost enables these types of structures to replace the traditional types in many applications. In the previous few decades, many modern guiding structures were introduced to replace the traditional types, especially at high frequency ranges. The substrate integrated waveguides (SIW) and the ridge gap waveguides (RGWs) were introduced to be used in high frequency applications. These types are not well-established standard compared to the traditional types of guiding structures. The main concern of this work is about the RGW and the reasons behind this choice will be discussed later. Both the SIW and the RGW have advantages and disadvantages compared to each other. The RGW carries TEM mode, while the SIW propagating mode is the TE mode, which results in a more dispersion. The RGW has no dielectric loss where the signal propagates inside an air gap. Regarding the conductor loss, although the RGW has a wider current distribution on the upper ground, the SIW has conductor losses inside from the vias that surround the guide. In terms of the size, the width of the

RGW with two rows is about the size of the SIW for the same frequency band. The fabrication is much easier in the case of the SIW. However the mechanical durability of the RGW component is much higher for the same components based on SIW.

1.4 Periodic Structures

The periodic structures concept is a very old concept in the electromagnetic field of research. The periodicity of the structure adds some features and properties for the propagation inside. In addition, utilizing the periodicity of the structure to achieve some requirements in the device itself is a well-known procedure in microwaves. One of the most famous examples is the filter design, and there are many applications based on the concept of periodic structures. Some of the periodic structures are given a special name based on their configuration, behavior or basic operation. In the following subsections, a brief explanation will be shown for two main categories of periodic structures.

1.4.1 Soft and Hard Surfaces

The concept of soft and hard surfaces was introduced by Kildal in 1988 [4]. This concept is used to describe the propagation of electromagnetic waves along these corrugated surfaces. The choice of this terminology is based on the analogy with soft surfaces and hard surfaces in acoustics. The soft surfaces are the transversely corrugated surfaces where the power flux density at the surface is equal to zero. This means that this kind of corrugation stops the electromagnetic wave propagation. The reason behind this feature is that this kind of corrugation eliminates both the transverse electric field and the transverse magnetic field. Eliminating both transverse field components will stop the field propagation. On the other hand, the hard surfaces eliminate only the longitudinal field components and this support the propagation

of the only TEM mode. The corrugation consists of successive strips of metallic conductors and grooves. The grooves are of quarter guided wavelength depth at the operating frequency, and this implements a PMC surface. Finally, within the soft and hard bands, these surfaces act as periodic strips of PEC-PMC surface. However, for hard surfaces the corrugation must be filled with dielectric material that has a dielectric constant larger than the permittivity of the medium above the surface. The direction of the wave propagation relative to the direction of the corrugation determines whether it enables or prevents the wave propagation at the surface [5]. Figure 1.1 shows the classification of the corrugated surface graphically into soft and hard relative to the electromagnetic wave propagation direction. The red arrow indicates the direction in which the signal propagation is prevented, while the green arrow indicates the enabled propagation direction. A lot of applications are based on this concept, since it has been introduced in 1988, especially in the antenna field of research [6]. By controlling the corrugation in the antenna feeding structure or in the antenna itself, it is easy, based on this idea, to control the mode or the field distribution of the antenna aperture. This enables the antenna designer to control the antenna parameters like the radiation pattern, the gain, the half power beam width, etc. The soft and hard surfaces describe a 1D periodic structure where the PEC-PMC strips are repeated in one direction. There are other periodic structures that implement the periodicity in two dimensions. These structures called Electromagnetic Band Gap (EBG) structures. A brief discussion about the EBG structures will be addressed in the following section.

1.4.2 Electromagnetic Band Gap structures

The terminology of EBG structures was proposed in [7] to describe the 2D frequency selective structures (FSS). They are periodic structures that prevent the wave propagation of all polarizations and in all directions within the stop band. This terminology

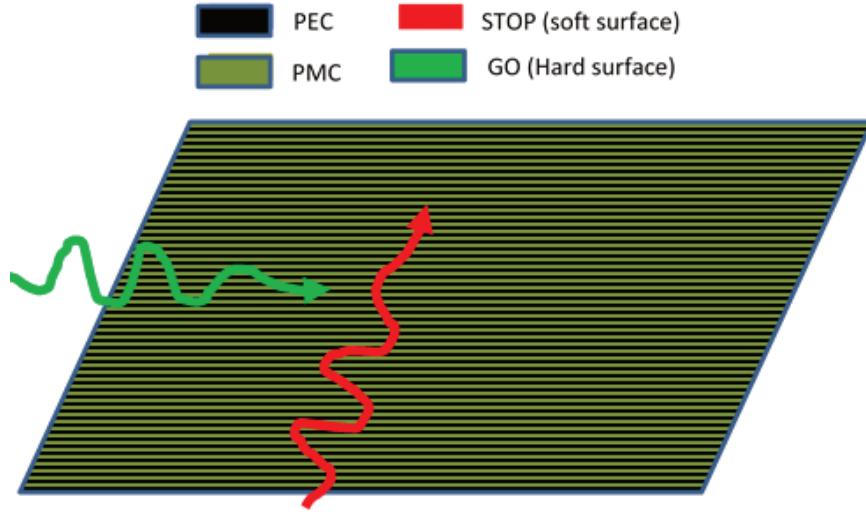


Figure 1.1: Soft and hard surfaces with respect to the wave propagation direction.

is based on the analogy with the Photonic Band Gap (PBG) in optics. A lot of work was done in this research area to design and analyze the cell that is repeated in such a structure. Also, much work was done to utilize the frequency selective property of these cells in microwave and antenna applications.

1.5 Ridge Gap Waveguide Structure

The ridge gap waveguide structure was published by Kildal in 2009 [8]. A 3D view of an example of this structure is shown in Figure 1.2 with the upper ground plane removed to show the configuration details. It was patented by the same professor in 2010. This technology can be considered as a normal extension of the soft and hard surface or an application of this concept but in 2D periodicity. The idea is based on having nails of quarter wavelength to form a PMC surface. These nails are covered by a ground plane made of a conducting material as shown in Figure 1.2. These nails form a PMC surface and in between these nails a PEC ridge is passing through to guide the signal. The signal path is a parallel plate-like structure and surrounded by PEC-PMC parallel plate through which the propagation of the electromagnetic signal is

prohibited. This figure clarifies that there is a band gap in which the wave propagation inside the periodic cells is eliminated. Recently, gap-waveguides have been considered as guiding structures in high frequency applications. These guiding structures carry the signal in the form of a quasi-TEM mode while the artificial PMC around the signal path prevents the leakage. Since the ridge gap waveguides were proposed a few years ago, it became the focus of the attention due to its own advantages. These guiding structures support signal propagation inside an air gap and due to this fact, the gap waveguides are subjected to lower losses than both microstrip lines and SIW as the signal in both configurations passes through a dielectric substrate. The artificial PMC that surrounds the signal path plays an essential role in guiding the signal and inhibit the leakage, which gives the gap waveguides another advantage over the microstrip lines. One of the key elements in the gap waveguide configuration is the design of the unit cell that constructs the PMC surface. The operating bandwidth of the gap waveguide is controlled by the stop band of the cell structure that forms the artificial magnetic conductor surface, which creates the need of having unit cells with the highest possible stop band. In the coming section, more detailed discussions will be provided regarding the unit cell analysis. In the same section, the dispersion relation associated as well as the stop band of the bed nail unit cell (BNUC) will be illustrated. A lot of work has been done in this area, introducing different shapes of unit cells, achieving a bandwidth ratio about 2:1 and in some cases the bandwidth ratio might exceed a ratio of 3:1. One common need is a transition between the ridge gap waveguide and the standard connectors. In almost all of the published work, the used transitions are always responsible for limiting the bandwidth of the ridge gap waveguide. This limitation, in many cases, is about one-third of the possible bandwidth. In the following section, some of the published excitation mechanisms will be highlighted and criticized.

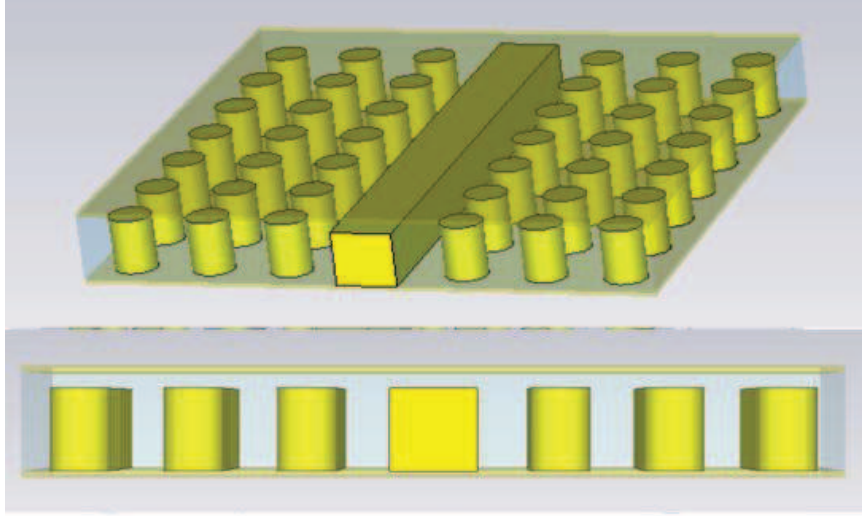


Figure 1.2: RGW vertical coaxial excitation mechanism in different views.

1.5.1 RGW Cell Analysis

The unit cell is the basic building block of the RGWs. These cells can be of many shapes to have different operating frequency ranges. The basic shape published in the first trials of the ridge gap waveguides is the nail with circular and rectangular cross section, which is called the BNUC [8]. Other shapes were introduced to increase the operating band like pyramid shape and also other trials were done to combine this technology with the microstrip line technology in the packaging process [9]. As mentioned before the stop band of the unit cell represents the bandwidth in which the structure prevents the leakage outside the ridge. This means that the stop band of the unit cell corresponds to the possible operating bandwidth of the whole ridge gap waveguide structure. This can also be called the maximum ideal band gap. The operating band of the RGW or the stop band of the unit cell is obtained numerically with the help of the eigenmode solver of any of the microwave packages. All simulations presented in this work are performed by CST MWS or HFSS. Figure 1.3 (a) represents the cell structure where a , b , d , and h represent the cell size, the nail width, the nail height and the air gap height, respectively. The dispersion relation

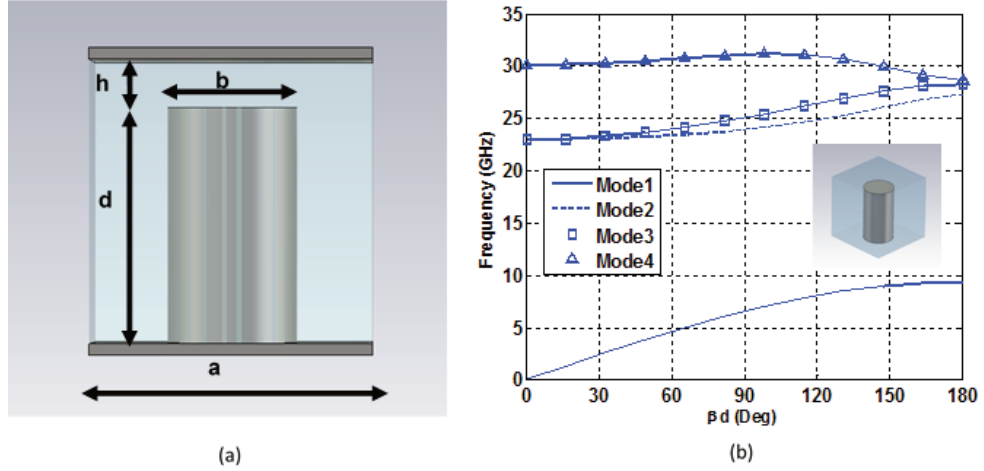


Figure 1.3: (a) The unit cell structure (b) The corresponding dispersion relation.

of a sample of the BNUCs is illustrated in the same figure part (b). This figure illustrates the first four modes inside the cell through the eigenmode solution. In this figure, it is very clear that the range of frequencies between 10GHz and 23GHz has no corresponding values for the phase constant, which means that this is the stop band of the BNUC or the operating bandwidth of the RGW based on this cell. Of course, the ideal bandwidth of the structure is a function of the BNUC dimensions and the mentioned values here are just a numerical example to simplify the concept of giving a BNUC sample to be studied.

1.5.2 The Field Distribution Along the Line

Another level of verification for the previously introduced concept is to study the field distribution along the ridge surrounded by the BNUCs. This simulation objective is to make sure that the fields are bounded by the ridge itself inside the operating frequencies, while it is not limited to this ridge at higher or lower frequencies. It can be seen easily from Figure 1.4 that the electric field is tightly bounded to the ridge at frequencies 10GHz and 13GHz in (b) and (c), while the leakage occurs beyond the operating bandwidth at 3GHz as shown in the same figure part (a).

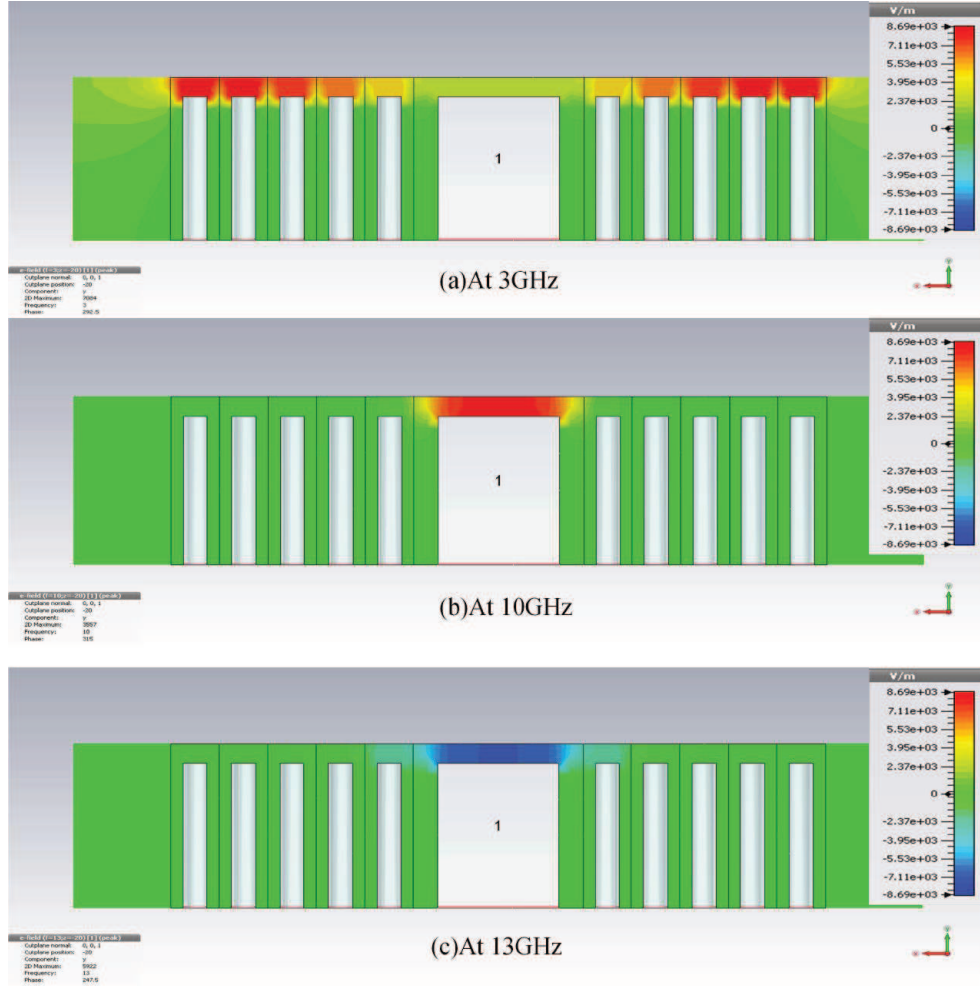


Figure 1.4: The field distribution in the RGW at different frequencies.

1.5.3 Excitation Mechanisms in Literature

The transitions presented in the literature used a simple tuning circuit to perform the matching. The transitions are mostly to transfer the signal from the coaxial connector to the ridge. This type of transition is proposed in [10–12]. The basic idea of this transition was to have a vertical probe coming out of the coaxial connector and located in a hole inside the ridge itself. By modifying the dimensions of the hole and the probe, the matching could be achieved. Regarding the ridge in this transition, it is extended with a half wavelength in one direction with an open circuit termination. This led to direct the signal in only one direction, which is the required objective. The transition

structure is illustrated in Figure 1.5 in top view and 3D view, while the upper ground plane is removed to show the structure details. Although this excitation technique was tested many times in different applications, it had a clear disadvantage of limiting the operating bandwidth of the RGW to one-third of the possible bandwidth. This can be noticed clearly in Figure 1.6. In this figure the operating bandwidth at -15 dB is about 2.5 GHz and 4.5GHz at -10dB. By considering the -10dB level, even it is not sufficient matching level of such transition, the operating bandwidth utilizes only about 34 % of the possible bandwidth of the BNUCs. The same transition was discussed in a lot of work [10,13–15]. The mentioned references are just some samples of the work that made use of the first published work of Kildal and deployed it in their applications. Some other transitions were presented previously to connect the RGWs and other types of connectors like coplanar waveguides or microstrip lines. Some of these connectors have shown better performance than the traditional one. The transition between the coplanar waveguide and the RGW was presented in [16]. The transition is based on a coupling between a rectangular patch at the end of the coplanar waveguide and the ground plane of the RGW. This shape behaves also like a resonant circuit, where the dimensions of this patch are the key elements to achieve the matching. The published results of this transition showed a bandwidth ratio about 1.2:1, which is not covering the possible bandwidth provided from the cells. However, it should be stated that this transition is for the W-band (100 GHz). The operating bandwidth resulted in having a wide absolute bandwidth of the transition (about 10GHz) in spite of the small bandwidth ratio. Other trials were presented to connect the RGW and the microstrip lines. The transition presented in [18] is one of the best transitions in terms of the operating bandwidth as it covered the whole band, but it still suffered from the poor matching level and insertion loss. The transition basic idea is to connect the ridge and the microstrip line with a ridge section of the same height of the ridge and the same width of the microstrip line. The microstrip

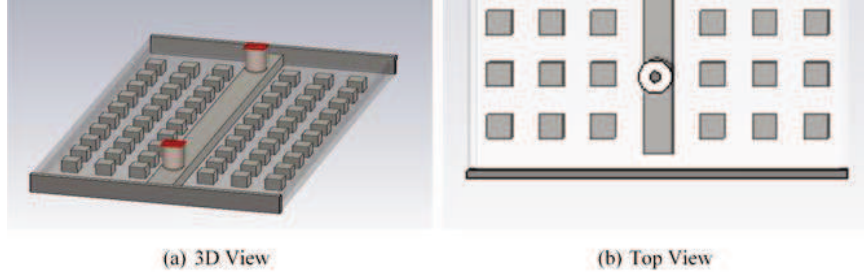


Figure 1.5: RGW vertical coaxial excitation mechanism (a)3D view (b)Top view.

line is packed with two rows of BNUCs to introduce smooth transition between the covered microstrip line with the BNUCs and the ridge surrounded by almost identical unit cells. It is clear that this reference is a good starting point to build up a transition between the RGW and the microstrip line, but it still needs some modifications to achieve a better matching level. After this discussion, it is clear that lots of transitions were presented in the literature to connect between the RGWs and other connectors. The most popular transition is the one presented by Kildal in his first experimental setup to test the RGWs. It is a connector between a vertical coaxial connector and the RGW. This transition is used and tested a lot in different references, but it covered only a small part of the possible bandwidth provided by the BNUCs. Also, other transitions were proposed to connect between the RGWs and other lines like the transition between the RGW and the coplanar waveguide. Another transition is the one connected between the RGW and the microstrip line. The common feature among all the presented transitions is that they all failed to provide a good matching level, below -20 dB, for the ideal bandwidth supported by the BNUCs. The presented transitions either provide a good matching level for a small part of the expected band or cover the whole band with an insufficient matching level.

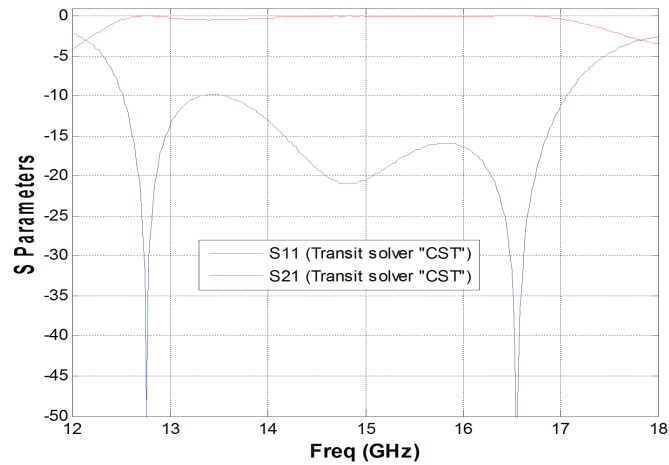


Figure 1.6: The scattering parameters of the vertical coaxial to RGW transition.

1.6 Objectives

As mentioned before, this work is a step toward the RGW standardization. The previous survey indicates that the presented transitions are band limited as they cannot utilize the provided bandwidth of the periodic cells. Hence, these transitions limit the proposed devices based on this technology. A wideband microwave device is not fully used with all its bandwidth as long as it is excited through a narrow band transition. The objectives of this work can be classified into five parts, where each part is to be discussed in a separate chapter in this thesis. The first objective is to propose wideband transitions to utilize the whole bandwidth supported by the unit cells. The second part is to propose different analysis techniques to measure and enhance the operating bandwidth of the RGW. The third and the fourth goals are to introduce reciprocal and nonreciprocal microwave devices, respectively. The last goal in this work is deploying this technology in different applications such as the material characterizations and antenna applications.

The work to be presented can be scaled to any frequency band. However, most of the proposed structures cover the frequency bands of airborne radar applications.

These bands are centered at 13.75 GHz and 16 GHz. Hence the actual frequency band, in this work is the Ku-band.

1.7 List of Contributions

This work can be considered as a step toward the standardization of the ridge gap waveguide. The work contributions can be summarized as follows:

- Two different transitions for the ridge gap waveguide with a deep matching level. These transitions can form an excellent measurement setup for the ridge gap waveguide components.
- An experimental validation procedure for the unit cell dispersion relation.
- An accurate way to evaluate the bandwidth of the ridge gap waveguide. This enables the designer to build up various components based on an accurate estimation of the bandwidth.
- Novel cell configuration as well as a novel type of the ridge gap waveguide is presented with dual gap height.
- Wideband power divider based on ridge gap waveguides is introduced to cover the whole Ku-band and a part of both X-band and K-band.
- Novel 3-dB Hybrid coupler based on ridge gap waveguide
- Wideband RGW circulators are presented based on a novel closed-form solution for the middle junction.
- A new technique for textile material characterization based on RGW measurement setup
- A leaky wave antenna fed by RGW structure that is able to scan the beam with frequency without having any grating lobes.

1.8 Thesis Organization

The thesis is divided into seven chapters. This chapter covers the basic concepts, the motivation, and the objectives. The coming chapter presents two different transitions. One of them connects between the RGW and a standard coaxial connector and the second one transfers the signal in between the microstrip line (MSL) and the RGW. Both transitions are able to cover the possible bandwidth of the unit cells. Chapter three describes a new methodology to determine the cell behavior experimentally. The same chapter also criticizes the traditional methods for identifying the possible bandwidth of the structure and introduces low cost printed cells to enhance the bandwidth of the whole structure. In Chapter four, two different microwave devices are to be presented. A wideband power divider and a hybrid coupler are two samples of passive microwave devices implemented based on the RGW technology. In chapter five, the junction circulators are studied in detail. A closed-form solution is obtained for the first time to this problem. This closed form solution is applied to the design of RGW circulators. Two different applications are studied in Chapter six. The first application is to use the straight RGW and the transitions in the dielectric constant measurement of textile material. The second application is a grating lobe free RGW slot antenna array. The last chapter summarizes the results obtained in this thesis and suggested further developments.

Chapter 2

Ridge Gap Waveguide Excitation

2.1 RGW Transitions For Airborne Radar Applications

The ridge gap waveguide technology can be deployed in many systems, but this fact is highly affected by the existence of high-performance transitions and components that are compatible with this type of technology. The selected frequency band, in this work, aims to serve airborne radar applications in Ku band. These applications utilize the frequency bands 13.25 – 14.2 GHz and 15.5 – 17.5 GHz. This work is a part of a complete project to propose high-performance ridge gap waveguide transitions and components to replace the existing guiding structures in the airborne radar applications due to their advantages over other types of the well-known structures. The lower losses, the less dispersion and less need for perfect electrical contacts are the motivation to use ridge gap waveguide in radar systems. The selected dimensions of the ridge gap waveguide structure are 6.5 mm, 3 mm, and 1 mm for the cell size, the pin width, and the gap height, respectively, which leads to a possible operating frequency band from 10 GHz to 23 GHz to cover the required application frequency bands.

The proposed transitions in this work are divided into two types: The first one is a transition from a 2.92 mm coaxial connector to RGW. The second one is an MSL to RGW transition. They are addressed in the subsequent sections in details.

2.2 Coaxial Line to RGW Transition

2.2.1 Coaxial to Ridge Gap Waveguide Direct Transition

Since ridge gap waveguides had been introduced in 2009, many experimental setups are established to test such structures [10]. The previously published transitions are designed to use a hole inside the ridge with a probe coming from the inner conductor of the coaxial cable to form a matching section configuration. An optimization process is performed to adjust the dimension of the probe and the hole to achieve matching in the required frequency band. Having an open circuit (OC) at one end of the ridge at a distance of a half wavelength directs the signal constructively in the required direction. Figures 2.1 and 2.2 (a) show the 3D structure and the top view of the direct transition from a coaxial connector to ridge gap waveguide, taking into consideration that the upper and the lower metal sheets are removed to illustrate the internal details of the structure. This configuration, vertical coaxial with OC termination, limits the bandwidth of the ridge gap waveguide to be 12.5 : 17 GHz (at -10 dB threshold), which is about one-third the possible band of the ridge gap waveguide. The dimensions of this transition can be found in [10]. The S-parameters for a double transition of this configuration is shown in Figure 2.2 (c). This ridge gap waveguide has a bandwidth of 10 : 23 GHz and this will be discussed in more detail in a later section. It is very important to mention that taking -10 dB as a threshold to evaluate the bandwidth is not sufficient, and this is a clear drawback in the previously proposed transition, so the threshold in the following work will be taken as -15 dB for the double transition. A remarkable improvement can be obtained by having a

short circuit (SC) at a distance of a quarter wavelength at one end instead of the open circuit. This is based on the fact that leaving the terminal of the guided structure with no connection will not ensure the open circuit termination. The fringing fields will form some reactance part, and this will affect the matching level. Connecting the ridge to the backward wall and ensuring the electrical contact will give better performance. The short circuit solution has a shorter distance to the back wall. Figures 2.2 (b) and (c) show the modified configuration with short circuit termination and the S-parameters of double connection, respectively. It can be seen from this figure that the bandwidth of the modified structure is 11.5 : 19 GHz, which is about half of the possible bandwidth of the ridge gap waveguide at -10 dB. Taking the bandwidth threshold at -15 dB the bandwidth of both transitions is 23% and 34% in the case of the open circuit and the short circuit terminated transitions respectively. By visual comparison between the S-parameters of both configurations, it is easy to notice the performance improvement in the short circuit termination configuration. It has a wider bandwidth and a lower reflection level in the out of band region. The only drawback will be the procedure used to ensure the electrical contacts and this can be easily done if the lower half of the structure will be fabricated out of one piece of conductor.

Both techniques presented in this section have similar disadvantages. They are not covering the whole possible frequency band. Moreover, they have a poor matching level within the operating bandwidth as the provided matching level is about -10 dB, which is not sufficient in straight line guided structures. Finally, both depend on connecting an SMA connector with a probe to be placed in a specific hole in the ridge with a certain height. The matching level is very sensitive to the height of this probe. This increases the difficulty of the fabrication process and reduces its flexibility and tolerance.

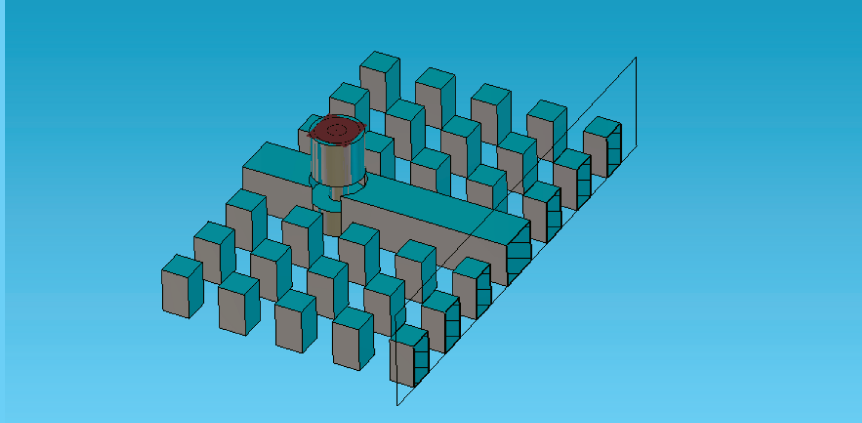


Figure 2.1: The 3D structure of the direct transition with open circuit termination.

2.2.2 Wideband Coaxial to Ridge Gap Waveguide Transitions

The main contribution of this work is introducing a new technique to excite the ridge gap waveguide structure. The main idea is initiated upon a simple observation. In simulating a ridge gap waveguide using any of the commercial tools, it is better to use a wave port. In this case, the possible bandwidth is almost entirely covered. Some previous work was presented, in the literature, regarding the size of the numerical port deployed in the ridge gap waveguide simulation [17]. The optimum dimensions that separate between the port and the first row of pins are followed here. On the other hand, the work presented in [17] has a fixed height of the numerical wave port from wall to wall. In addition, the optimization process is performed on the port height and width. Figure 2.3 (a) illustrates the simulated model of the ridge gap waveguide with wave port technique. It is evident that the operating bandwidth in Figure 2.3 (b) is almost entirely covered with a pretty good matching level. The possible bandwidth of the bed of nail unit cell used in this structure is 13 GHz. The starting frequency is 10 GHz and it ends at 23 GHz, which will be discussed in more detail in the subsequent section. This possible bandwidth is calculated in the ideal case, where the infinite periodicity is assumed. On the other hand, the simulation using a wave port considers a finite periodicity, that somehow limits the operating bandwidth

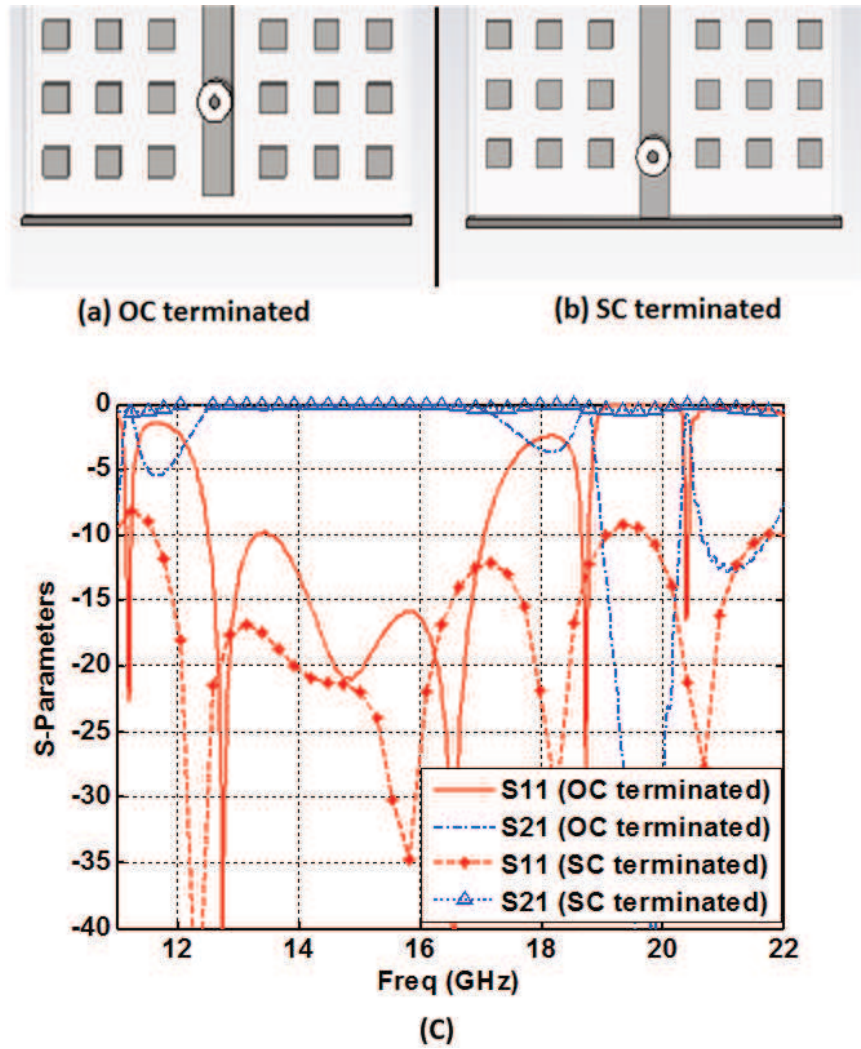


Figure 2.2: The direct transition from coaxial line to ridge gap waveguide (a) Open circuit terminated (b) Short circuit terminated (c) The S-parameters.

to be 10.5 GHz, starting from 12.5 GHz and ending at 23 GHz. The bandwidth in this part is evaluated with -15 dB threshold, which is a more acceptable criterion in such a transition. It is important to mention that the matching level is exactly as the threshold at the first part of the bandwidth, as shown clearly in Figure 2.3 (b). Although this figure indicates that the matching is maintained beyond 23 GHz, but the theoretically expected value of the maximum operating frequency is 23 GHz, which is calculated via the eigenmode solver based on assuming infinite periodicity. The wave port in this model is very close to a single ridge waveguide. The transition design is divided into two parts. The first part is a transition from a standard coaxial connector to a single ridge waveguide with optimized dimensions to achieve a quite good matching level. Lots of old transitions were introduced long time ago to convert the coaxial connector to rectangular waveguide or double ridge waveguides [18–20]. These kinds of transitions can be considered as a guiding line or an initial point for the first part. The second part is a fitting section to convert the dimensions of the single ridge waveguide at the end of the first part to the needed dimensions suitable to act as the wave port excitation. This part, specifically, can be redesigned if there is some slight modification of the ridge gap waveguide dimensions. Dividing the transition into two parts is intentionally performed as this transition is made to provide the required excitation for various components like couplers and circulators based on ridge gap waveguide technology in a research project for introducing different types of ridge gap waveguide components in airborne radar applications. Building up the transition in two separate parts makes the transition more adaptable to the required changes in the following component dimension. The transition is designed of two successive parts to increase the design capability of being used with different ridge gap waveguide structures. The transition can be employed with other ridge gap waveguides of various heights by reproducing the second part only. As the second part has a lower cost, around half the cost of the first part, the overall cost of having

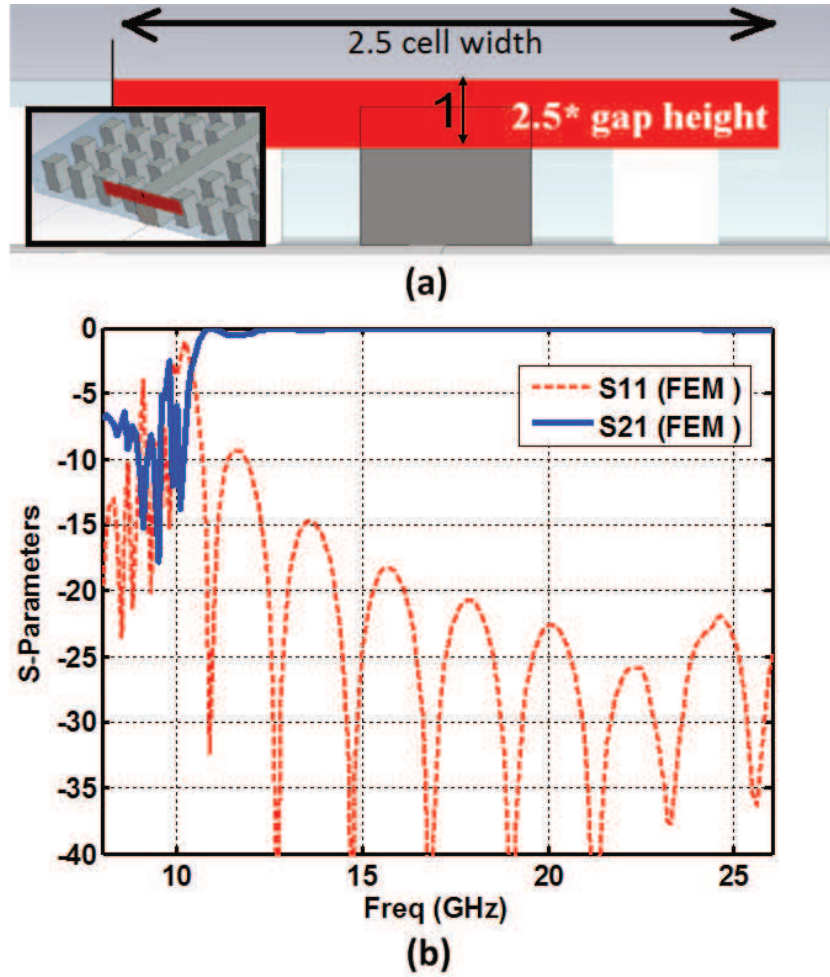


Figure 2.3: (a) The simulated model of ridge gap waveguide excited via wave ports (b) The S-parameters.

a few transitions can be reduced a lot by this design methodology. In addition, the fabrication time of the second part depends only on the CNC machining availability, while the first part is a function of both the CNC machining and the connector availability. In the following subsections, a detailed discussion is presented to explain both parts.

PART 1: A 2.92 To Single Ridge Waveguide Transition

The selected standard coaxial transition is the 2.92 mm connector. Its operating bandwidth covers up to 40 GHz. It is also compatible with SMA and 3.4 mm connectors. Figure 2.4 shows a schematic for the first part of the proposed transition. This part is constructed of an extension of the inner conductor of the standard coaxial connector to be placed in a base. The base is basically a solid cylinder of a conducting material. On one side, a wideband short circuit is placed at a distance of a quarter wavelength from the inner conductor at the center of the operating bandwidth (17.5 GHz). In the other direction, a five-section matching network is designed to achieve the required matching level. The objective bandwidth starts at 10 GHz and ends at 25 GHz to cover a bandwidth ratio of 2.5 : 1. The mathematical procedure for the impedance estimation of each section can be explained as follows.

Initial Dimensions Estimation: Mathematical Formulations

Cohn presented expressions for the cutoff frequency and the guide characteristic impedance in the case of single and double ridge waveguides [21]. Based on the cross section shown in Figure 2.4, where h , W_r are the height of the gap and the width of the single ridge waveguide, respectively, the following phases will be defined

$$\theta_1 = 2\pi \frac{(W_t - W_r)/2}{\lambda'_c} \quad \theta_2 = 2\pi \frac{W_r/2}{\lambda'_c} \quad (2.1)$$

where λ'_c is the cutoff wavelength in the presence of the ridge, which can be related to λ_c “the cutoff wavelength of the guide in the absences of the ridge” with the following equation

$$\lambda'_c = \left(\frac{\pi/2}{\theta_1 + \theta_2} \right) \lambda_c \quad (2.2)$$

which is obtained through modeling the ridge as three parallel admittances. These admittances are an open circuited line, a short-circuited line, and the discontinuity. This discontinuity is denoted by B_0 and it is modeled by Whinery and Jamieson in [22]. This leads to obtaining the first root of the following equation

$$\frac{(h + z_r)}{h} = \frac{\cot(\theta_1) - B_0/Y_{01}}{\tan(\theta_2)} \quad (2.3)$$

Defining $Z_{0,\infty}$ to be the guide impedance at infinite frequency, which is the ratio between the voltage to the total current in the upper face exactly across the center of the guide [22],

$$\begin{aligned} Z_{0,\infty} &= \frac{V_0}{I} = \frac{hE_0}{2 \int_0^{W_i/2} i \, dl} \\ &= \frac{120\pi h}{\lambda'_c \left(\sin(\theta_2) + \frac{h}{h+z_r} \cos(\theta_2) \tan(\theta_1/2) \right)} \end{aligned} \quad (2.4)$$

while the guide characteristic impedance is related to the guide impedance at ∞ through

$$Z_0 = Z_{0,\infty} \frac{1}{\sqrt{1 - (\lambda/\lambda'_c)^2}} \quad (2.5)$$

Using (2.4) and (2.5), the initial value of the characteristic impedance of the single ridge waveguide can be estimated. The values of h and W_r are 1.4 mm and 2.6 mm. The total width of the single ridge structure is $W_t = 14.5$ mm and the height of the ridge $z_r = 1$ mm. The starting dimensions can be obtained by solving a usual Chebyshev matching problem between 50 Ω line, which is the standard coaxial connector, and 200 Ω , which represents the single ridge waveguide side. All impedances are calculated exactly at the middle frequency of the band. Having the required impedance values to be placed between the coaxial line and the single ridge side, the

Table 2.1: The final dimensions of the matching network sections in millimeters.

Section i	h_i	z_i	L_i	W_i	W_{ui}
1	0.481	1.46	3.418	1.93	2.574
2	0.605	1.398	2.864	1.739	2.215
3	0.891	1.255	3.963	1.765	2.308
4	1.164	1.118	3.563	1.937	2.333
5	1.194	1.103	3.925	1.961	2.358

initial dimensions of the ridge sections can be obtained through the relation between the characteristic impedance and the gap height h . This can be simply calculated after rewriting (2.4) to be

$$h = \frac{Z_0 b \sin(\theta_2)}{120\pi b / \lambda_0 - \cos(\theta_2) \tan(\theta_1/2)} \quad (2.6)$$

where b is the distance between the upper and lower plates, which is a constant value for all ridge sections.

Starting with the initial dimensions, an optimization process is performed to obtain the required matching all over the band. The simulated model used within the optimization process with different views as well as the internal dimensions notations and the final response are shown in Figures 2.5 and 2.6, respectively. The proposed dimensions of the five sections matching network are listed in Table 2.1. In this table h_i represents the gap height, z_i represents the ridge height, L_i represents the section length, and W_i/W_{ui} are the ridge width in the lower half and the upper half, respectively. Regarding the dimensions of the wideband short circuit, they are listed in Table 2.2 where the same notation technique is used. The negative dimensions in this table mean that the ridge is just a groove in the upper and lower plates of the structure. The distance between the upper and lower walls is denoted by b in Figure 2.4, and its value is 3.4 mm for the whole design.

Table 2.2: The wideband short circuit dimensions in millimeters.

Section i	h_i	z_i	L_i	W_i	W_{ui}
1	0.908	1.246	1.159	2.067	2.441
2	3.911	-0.256	1.096	2.433	2.462
3	4.386	-0.493	1.694	3.026	3.033

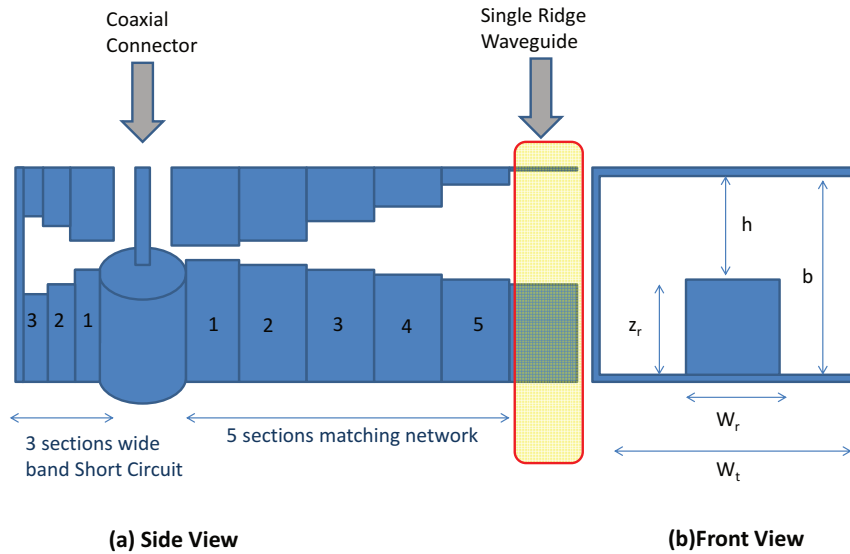


Figure 2.4: A schematic of the first part of the transition. (a) Side view. (b) Front view.

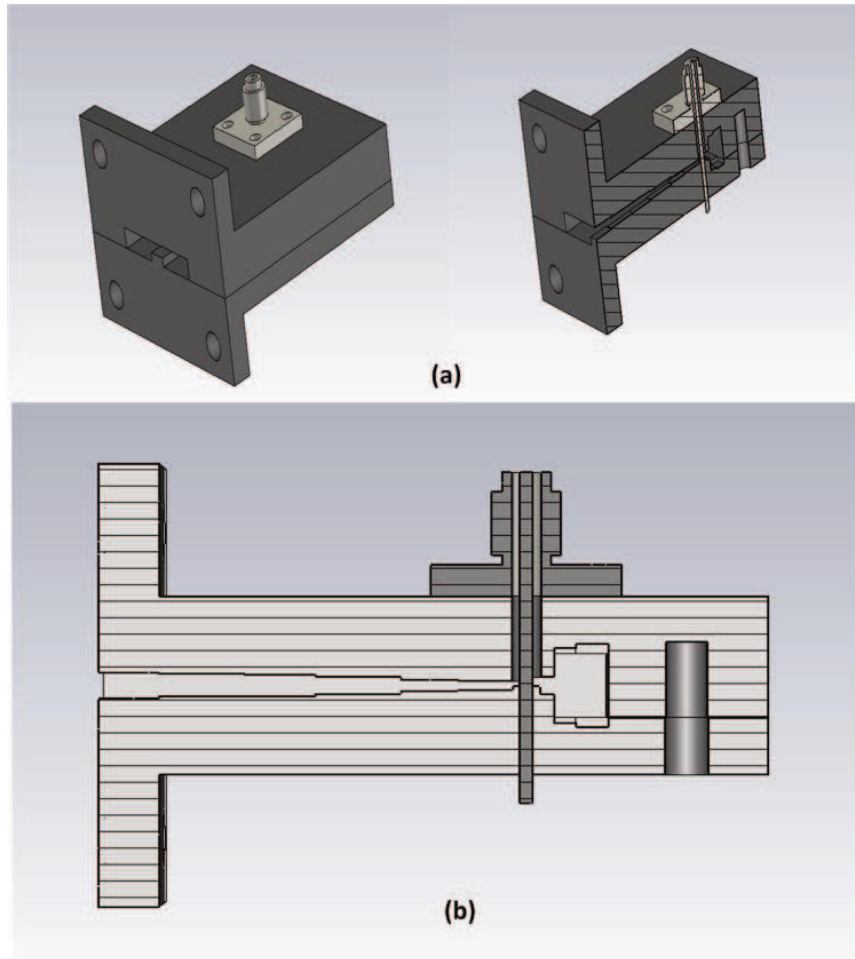


Figure 2.5: Part 1: 2.92 to single ridge waveguide transition (a) 3D view (b) Side view cross section.

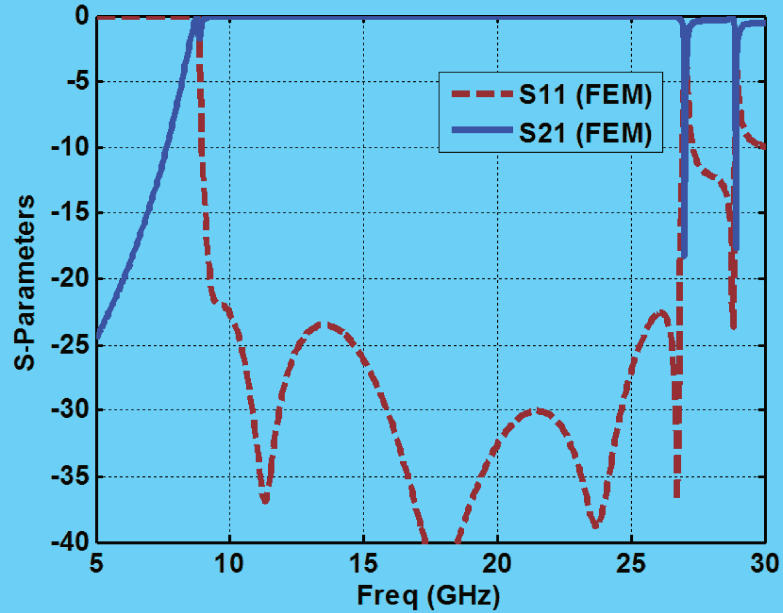


Figure 2.6: Part1: 2.92 to single ridge waveguide transition (a) Internal dimensions (b) S-parameters.

PART 2: Fitting section

The main purpose of this section is to convert the dimensions of a single ridge waveguide at the end of the first part to the dimensions of the single ridge waveguide that is suitable to feed the ridge gap waveguide structure. Figure 2.7 shows the two faces of the fitting sections with all dimensions indicated. The fitting section is a double tapered section, and its length affects the matching level. A parametric sweep is performed in this section individually to select a suitable length, which is depicted in Figure 2.8. It is clear from the presented figure that the length of the transition should exceed 20 mm at least. The selected length of the fitting section is chosen to be 25 mm to ensure a sufficient matching level around 10 GHz. It should be taken into consideration that this fitting section introduces relative high reflection in the first part of the operating bandwidth. Another optimization process is performed in the double connection transition, and it resulted in a better response in the case of having

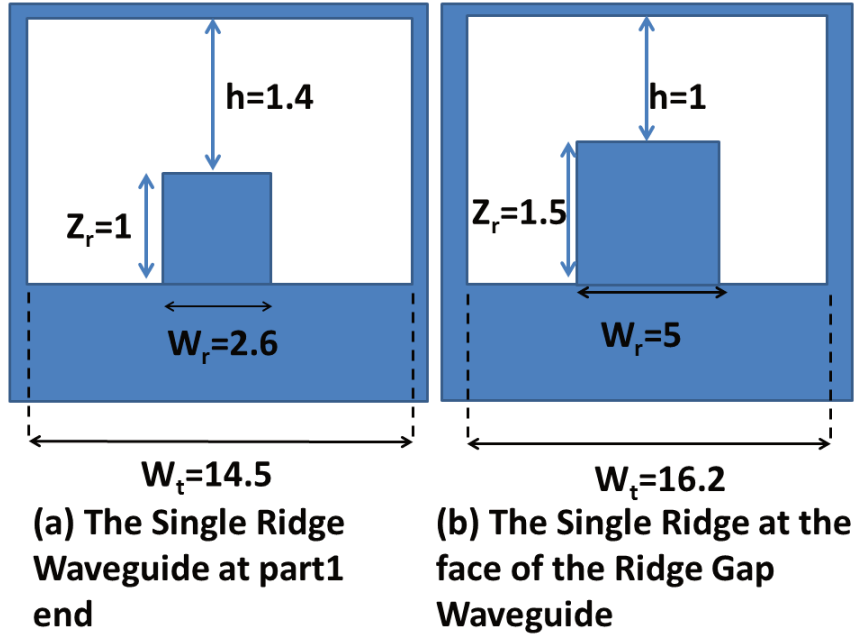


Figure 2.7: Part2: The fitting section two face dimensions.

two fitting sections of different lengths. This will be addressed again in the measurement section for the complete transition. The final transition has an asymmetric fitting section for best overall performance. In the case of deploying this transition in a ridge gap waveguide measurement, the transition effects are removed through the calibration process. This is performed whether the transitions on both ports are symmetric or not. The selected dimensions result in the best overall matching level, which gives more ability in the measurement of different RGW structures.

The wideband coaxial to single ridge waveguide with both parts and the scattering parameters are shown in Figure 2.9. One more note is that the matching level of both parts connected together is deteriorated to be around -17 dB in the frequency range of 10 GHz to 11 GHz and this is due to the fitting part alone. It should be taken into consideration that as the bandwidth threshold level is -15 dB for the double connection, the threshold for the single connection should be below -20 dB.

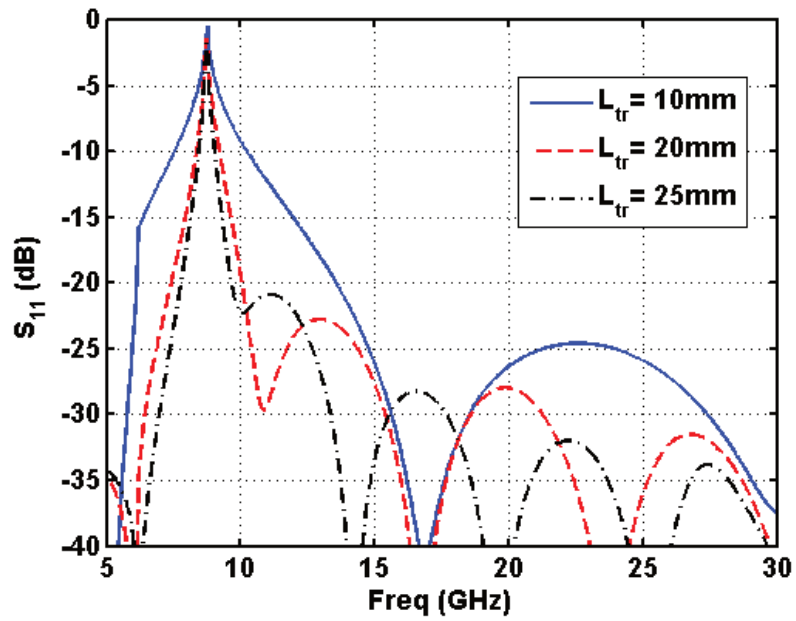


Figure 2.8: The S-parameters of the fitting section along with different values of L_{tr} (transition length).

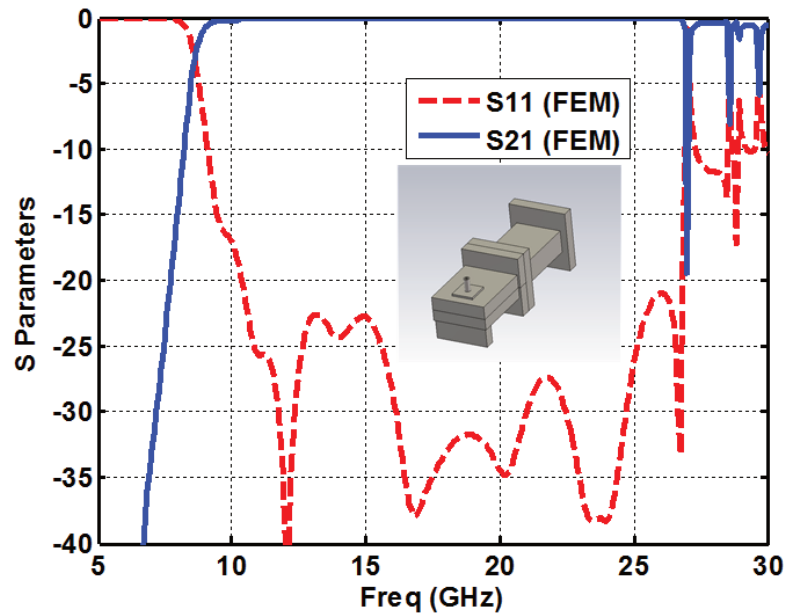


Figure 2.9: The scattering parameters of the wideband coaxial to ridge with the fitting part.

2.2.3 Testing the Wideband Transition

In the previous section, the design of the wideband transition was presented as well as the final dimensions of the proposed structure. The single transition has shown a pretty good matching level as discussed before. Another step of verification is testing the double connection. This will identify the reflection due to the excitation using the proposed configuration. After connecting this excitation to the ridge gap waveguide, which is the final goal of this work, it is a straightforward procedure to know the amount of mismatch associated with the ridge gap waveguide itself. The double connection (coaxial to single ridge waveguide to coaxial again) achieves a matching level below -16 dB for the double connection along the required bandwidth, which will be illustrated graphically in the comparison between the measurements and simulations in a coming section. Figure 2.10 shows the comparison between PEC, silver, copper, aluminum, and stainless steel. This figure shows that the insertion loss is very sensitive to the fabrication material as there is no loss due to radiation in the proposed design.

2.2.4 The Ridge Gap Waveguide Fed by the Proposed Transition

The first step is to design the ridge gap waveguide with $50\ \Omega$ characteristic impedance that has a flange with the same dimensions as that of the proposed transition. A starting value can be calculated from the parallel plate characteristics equation $Z_0 = \eta \frac{h}{W}$, but to achieve a better accuracy, the expression of the strip line can be used where [3]:

$$Z_{0,RGW} = 2Z_{stripline} = 2\frac{\eta}{4} \left[\frac{W}{2h} + 0.441 \right]^{-1} \quad (2.7)$$

The characteristic impedance of the RGW was studied before [10], and the value of

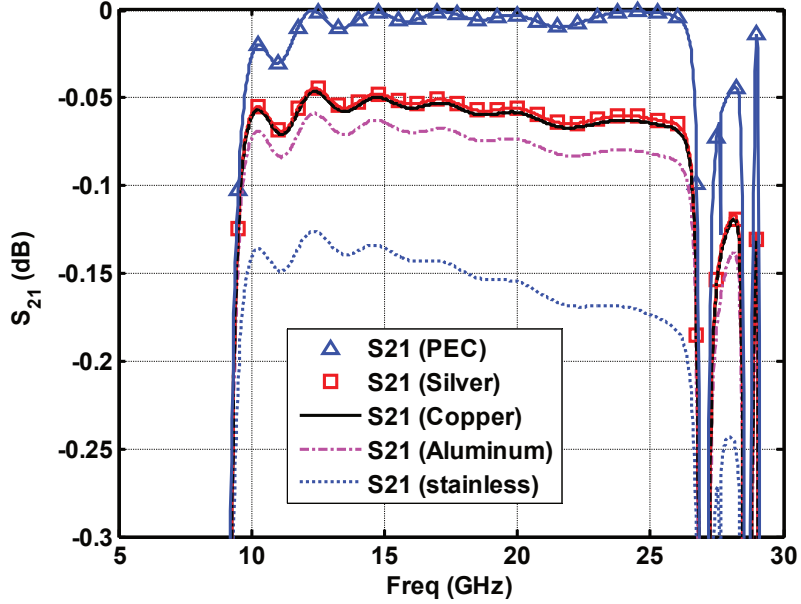


Figure 2.10: The comparison between different conducting material in fabricating the transition in terms of S_{21} (dB).

the characteristic impedance for the RGW is less than the values calculated through the stripline method. This can be compensated by decreasing the width of the ridge. The width of the ridge is 5 mm and the separation between the ridge, and the adjacent nail is the same separation between any two successive nails is $p = 3.5$ mm and the width of all nails is 3 mm. The bed nail unit cell design is based on the relations between the usable bandwidth limits and the nail dimensions [8]

$$d = \frac{\lambda_{up}}{4} \quad (2.8)$$

$$d + h = \frac{\lambda_{low}}{2} \quad (2.9)$$

Using the eigenmode solver to plot the dispersion relation of these dimensions, Figure 2.11 is obtained for both circular and square cross-sections for the nails. This figure shows that these dimensions give a bandwidth ratio about 2.3:1. As mentioned before, the possible bandwidth of these unit cells starts at 10 GHz and ends at 23

GHz. The solver assumes infinite periodicity in calculating these values, which is not applied in the real case. The finite periodicity and the ridge existence reduce the possible band to be 10.5 GHz instead of 13 GHz. This fact is illustrated in Figure 2.12, which simulates the ridge gap waveguide structure with a finite periodicity and single ridge waveguide ports. Plotting the field distribution along the cross-section of the ridge indicates that the signal is almost fully confined within the ridge, and there is no leakage, which is illustrated in Figure 2.13.

Finally, connecting the ridge gap waveguide to the proposed transition and the corresponding scattering parameters will be shown in the subsequent section to compare between the simulated and the measured results. The final scattering parameters of the ridge gap waveguide excited by the proposed transition clarify the ability of the proposed excitation mechanism to cover the operating bandwidth. The limitation in the operating bandwidth is due to the finite number of cells in the transverse direction, which results in shifting the starting frequency to be 12.5 GHz as will be shown in the subsequent section. The proposed transition is able to cover a wider bandwidth than the bandwidth provided via the realized ridge gap waveguide structure, which is the ultimate goal of this work.

2.2.5 Experimental Validation

Part 1 Validation

The key element of the proposed transition is the first part which is, simply, a wide-band coaxial to single ridge transition. Two pieces of this part are fabricated and tested in back-to-back configuration. Figure 2.14 shows the internal configuration of the fabricated connector. The measured results of the double connection are illustrated in Figure 2.15. The matching level in the fabricated double connection is below -18 dB across the entire band. This means that this transition covers the whole bandwidth with -15 dB threshold level for the double transition with an insertion

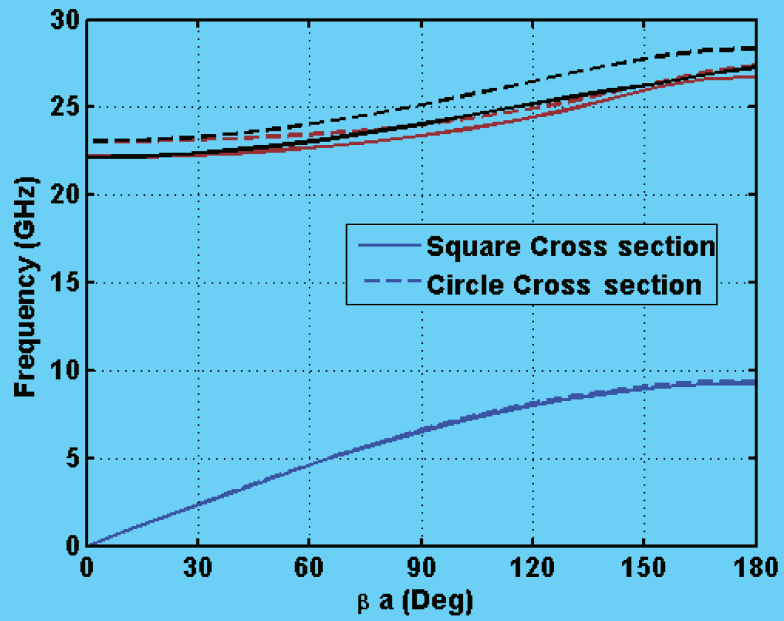


Figure 2.11: The dispersion relation of the bed nail unit cell used to build up the ridge gap waveguide.

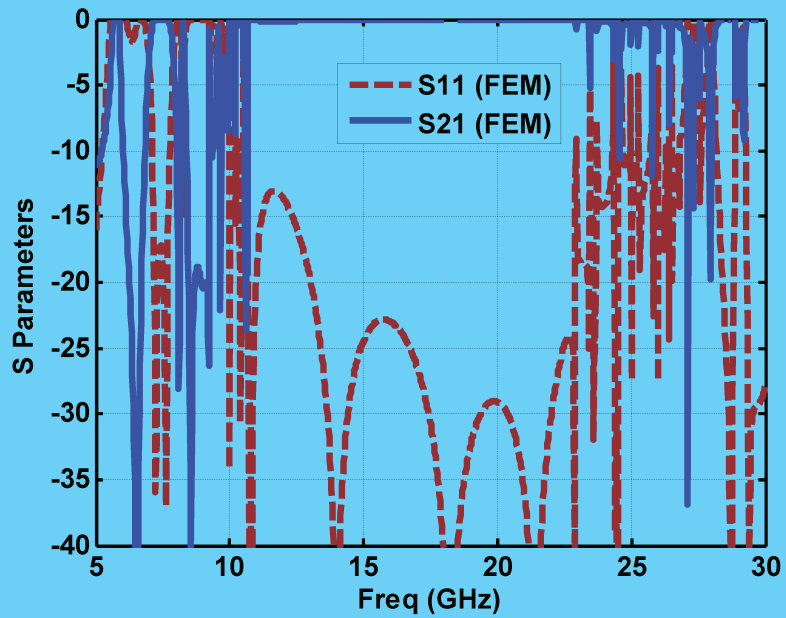


Figure 2.12: The RGW final structure's scattering parameters fed by a single ridge waveguide.

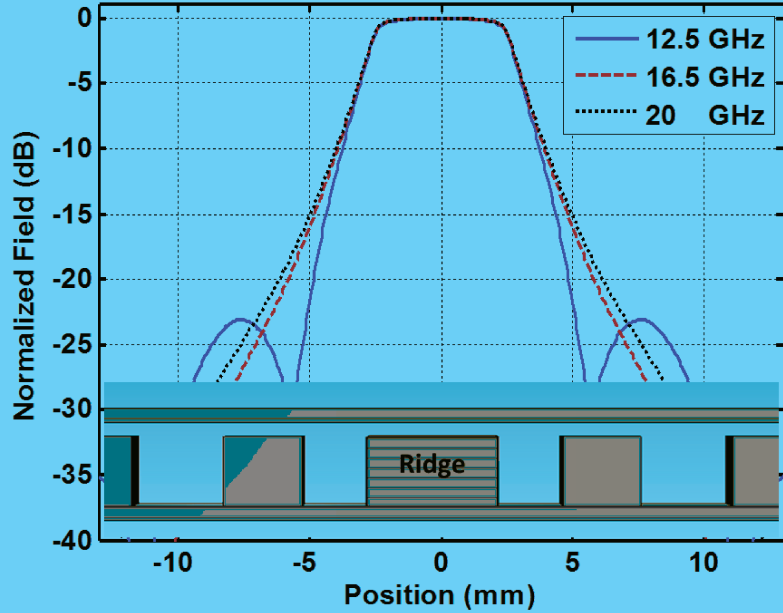


Figure 2.13: The normalized field distribution of different frequencies within the operating bandwidth normal to the ridge.

loss level about -0.15 dB for the double transition. The complete structure includes the fitting parts (transition part 2) and the ridge gap waveguide straight section of 2.5λ at the center of the band, which is discussed in the next subsection.

The Whole Structure Validation

The complete structure is fabricated and assembled. The fabricated parts are shown in Figure 2.16. The VNA is used to perform the S-parameter measurements for the whole configuration. The measured results are compared with the simulated results in Figure 2.17, which shows a very good agreement between both responses. The insertion loss is illustrated in the same figure, which indicates the insertion loss variation between -0.1 dB to -0.3 dB. Taking into consideration that the line length is around 2.5λ at the center of the band, the insertion loss varies between -0.04 to 0.12 dB per wavelength. The main reason behind the insertion loss is the connection between the inner conductor and the base of the structure, which made with a hole



Figure 2.14: The internal configuration of the fabricated connector.

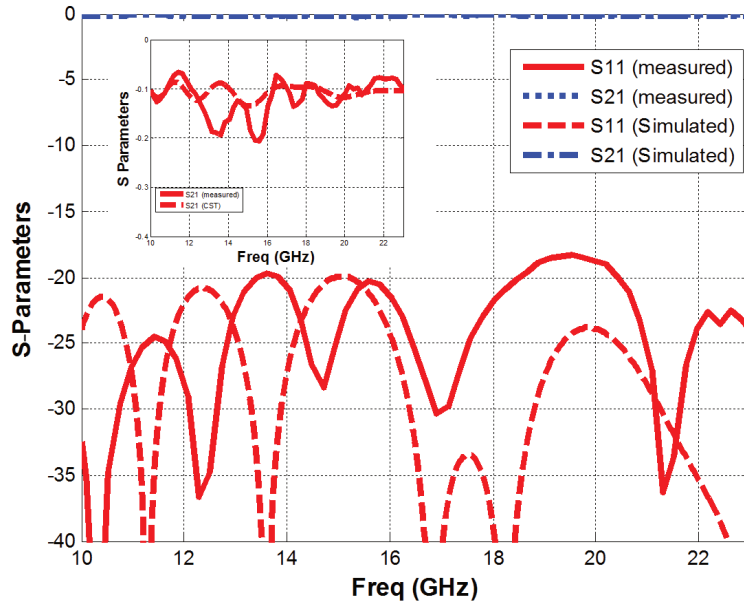
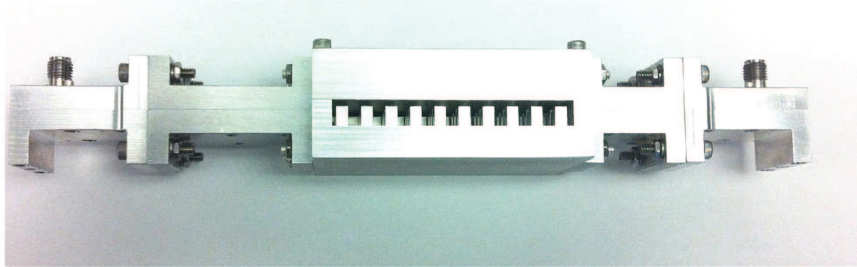
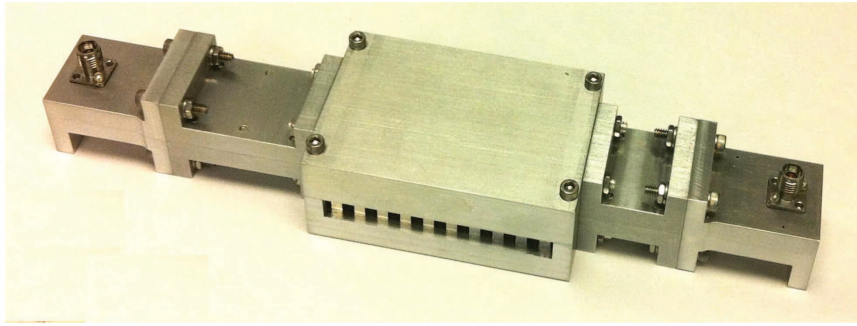


Figure 2.15: The scattering parameters of the double transition.

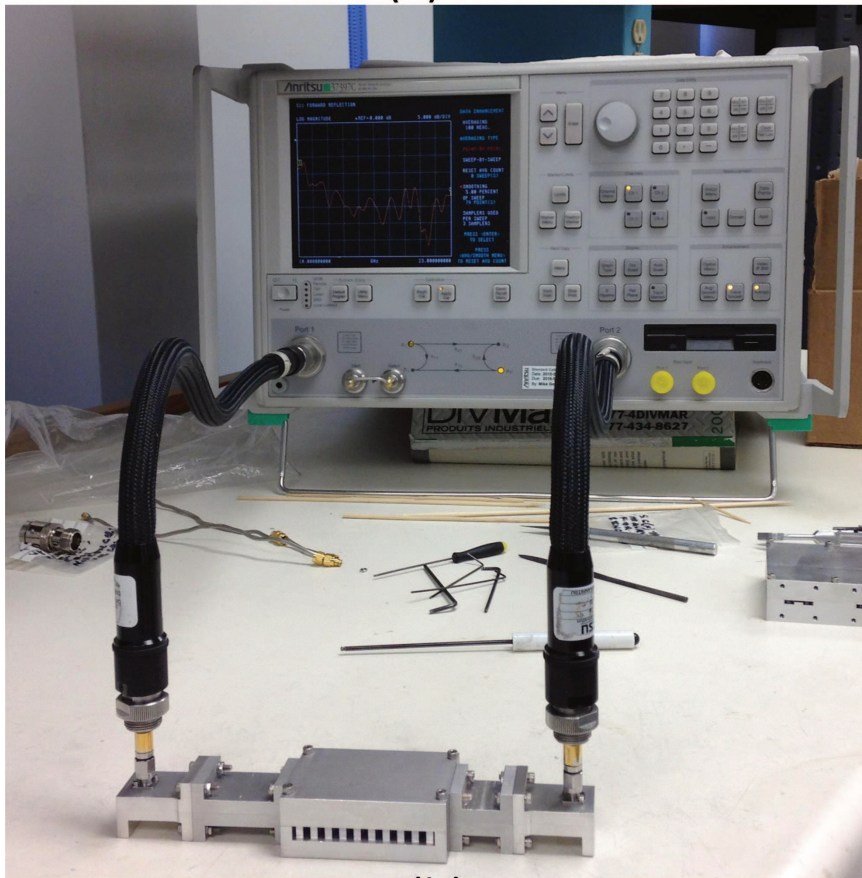
of a slightly larger diameter compared to the inner conductor of the coaxial connector. To introduce a tight fitting for the inner probe, which ensures a good electrical contact, a soldering silicon layer is used to increase the inner probe diameter. This resulted in a slight increase in the insertion loss. It is worth mentioning that all pieces are fabricated of Aluminum to reduce the fabrication cost. The insertion loss can be enhanced by changing the material and having better techniques to achieve the electrical contact between the inner conductor of the coaxial and the ridge matching sections. This indicates a better response than previously presented transitions for RWG in different applications [23, 24]. The good insertion loss is due to the absence of the radiation and the dielectric losses [25–27].

2.3 MSL to RWG Transition

Although the ridge can be designed to be $50\ \Omega$ lines [10], it is still not a straightforward procedure to attach it to a standard $50\ \Omega$ connector. In many published works in this area, the direct connection between the standard coaxial and the ridge is constructed by placing simple matching section consists of a hole in the ridge with a probe placed inside. The size of the hole and the length of the probe are the parameters used to achieve the matching, as mentioned before. Although this technique is able to achieve the matching, but this is applied only for one-third of the possible bandwidth. Another straightforward idea is to connect the ridge to a standard $50\ \Omega$ line like the microstrip line. Having a transition between microstrip lines and ridge waveguides will solve the excitation problem as connecting the standard $50\ \Omega$ connectors to the microstrip line is a simple and well-established procedure. In the following part, the transition design procedure and the dimensions will be explained in details.



(a)



(b)

Figure 2.16: (a) The complete structure after assembly. (b) The measurement setup.

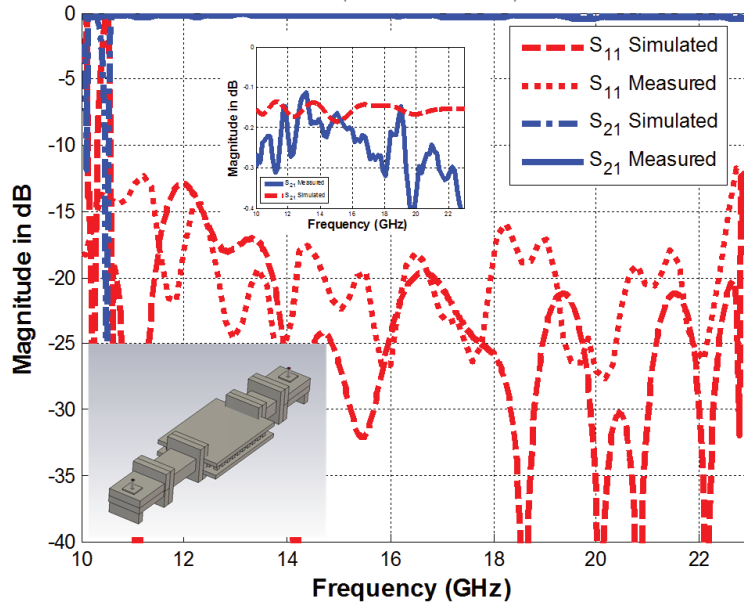


Figure 2.17: The S-parameters comparison for the whole structure.

2.3.1 The Transition Design

First of all, a low relative permittivity substrate is selected to build the microstrip line. As the microstrip line is a dielectric filled parallel plate-like structure, while the ridge gap waveguide is an air filled parallel plate-like structure, the matching will be easier as long as the dielectric constant of the substrate is closer to one. The microstrip line is fabricated on a Rogers RT5880LZ substrate with a relative permittivity of 1.96. The substrate thickness is 0.625 mm, which will be exactly equal to the gap height in the ridge gap waveguide. The periodic cells are extended on the microstrip line side to provide a sort of shielding. This extension eliminates the radiation as well as introducing a smoother transition, which will be now a transition from a ridge gap waveguide surrounded by periodic cells and a microstrip line packaged by identical cells. The packaged microstrip lines have been addressed many times before in the literature to get rid of the radiation losses [9, 17]. The matching between the microstrip line and the ridge gap waveguides can be performed by changing the ridge dimensions [28]. This work introduces another technique to achieve the matching by

inserting multi-sections of lower dielectric constants substrate between the ridge and the microstrip line. The lower relative permittivity substrates will be obtained by using the same substrate and apply some perforation to achieve the required relative permittivity. The dielectric constant value is controlled by the density of perforation, and this will be discussed in a later section.

Starting with the double cone back to back cell design proposed in [29], the cell is analyzed with a gap height of 0.625 mm to match exactly the selected substrate thickness. Figure 2.18 shows the dispersion relation of this unit cell as well as the cell structure, where the cell width $a = 5.6\text{ mm}$, the cap diameter $b = 3.2\text{ mm}$, the nail height $d = 5\text{ mm}$ and the gap height $h = 0.625\text{ mm}$. These are not the optimized dimensions as listed in [29] because of some constraints in the fabrication facilities resulted in shrinking the used cell size in this design to provide the whole structure size within the limits of the used 3D printing technique. The schematic of the proposed design is illustrated in Figure 2.19. This figure shows that the microstrip line is passing through the original substrate first for a very short distance to provide a suitable space for soldering the SMA connector. Then the same line is passing through a substrate covered by almost identical periodic cells. The nails in this first row of cells are shorter by 0.45 mm with the same cell size and cap diameter. It is important to mention that the characteristic impedance of the microstrip line is affected by the periodic cells loading of the first row, where the existence of these nails will increase the characteristic impedance for the same line width as discussed in the literature [17]. This means that the microstrip line width covered with these nails should be increased to maintain the $50\ \Omega$ characteristic impedance in the existence of the nails. This is followed by two matching sections formed by placing two perforated substrates below the ridge. Both sections can be considered as gap waveguide sections filled with a dielectric instead of air. The effective relative permittivities for both sections are taken to be 1.8 and 1.58 respectively. It is evident that taking lower

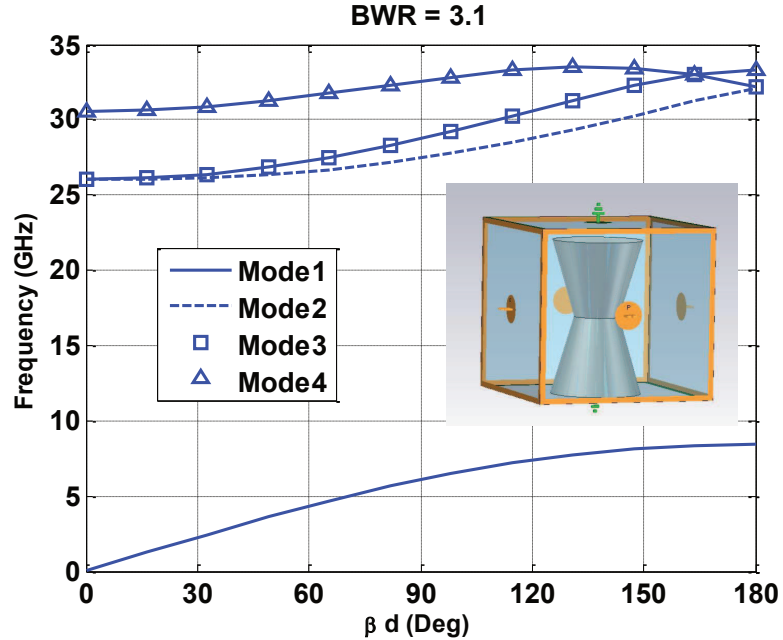


Figure 2.18: The dispersion relation of the double cone back to back unit cell.

values of relative permittivity will provide better matching, but the selected values of the relative permittivities must be feasible to be implemented via perforation as will be explained in the following section. The ridge width in the matching section 1 & 2 is designed in a way to satisfy the 50Ω characteristic impedance. Regarding both matching sections lengths, they are assumed to be one cell size as a starting point. It is very important that the values of these sections lengths should be equal to the quarter wavelength at a certain frequency within the operating bandwidth. Afterward, an optimization process is performed to achieve a good matching level. Figure 2.20 shows the scattering parameters in the ideal case. We mean by the ideal case that matching sections 1 and 2 are implemented with a substrate of exactly the required dielectric constants (1.8 and 1.58).

The losses in the transition sections are included as the simulations take into considerations the loss tangent of the substrate and the conductivity of the line and the ground. The shown figure illustrates that the achieved matching level is about -20 dB for the whole double transition.

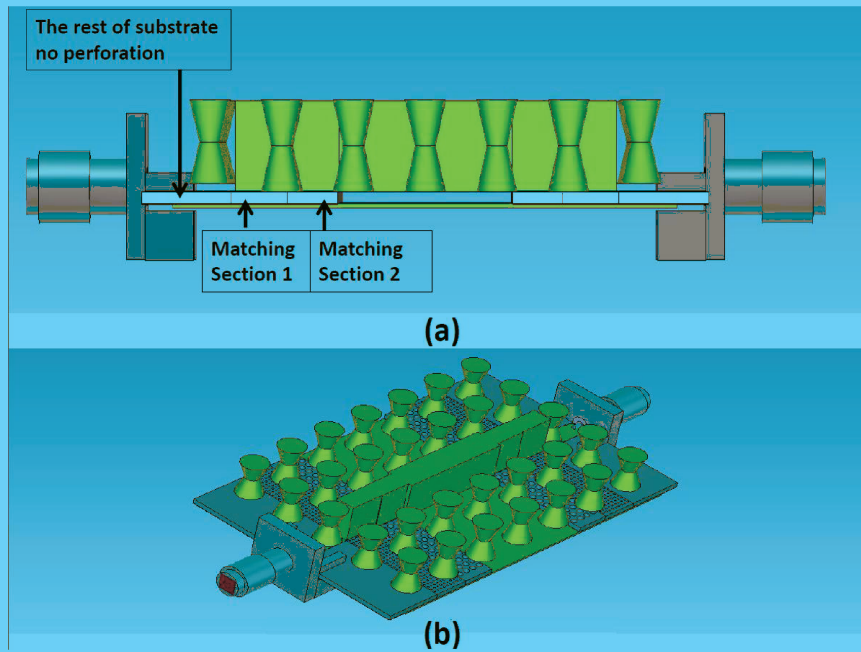


Figure 2.19: The transition between microstrip Line and ridge gap waveguide (a) Side view (b) 3D view.

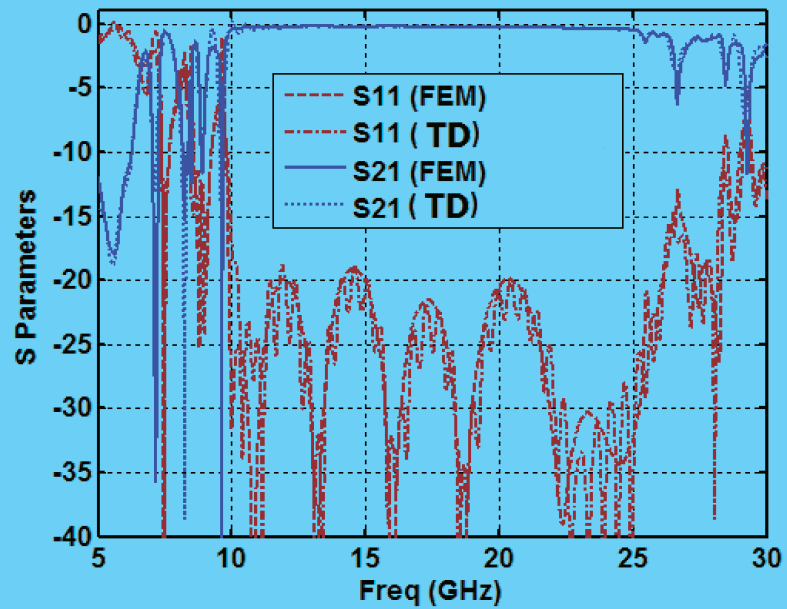


Figure 2.20: The scattering parameters of the transition in the ideal case.

2.3.2 The Perforated Substrates Design Procedure and Verification

The second step is to replace the ideally simulated matching sections by perforated Rogers RT5880LZ substrate that has very close relative permittivities to the assumed values. The implementation of particular values of the relative permittivities using a standard substrate of higher relative permittivity is discussed in many applications like the dielectric resonator antennas and the reflectarrays [30]. Many equations relate the perforation dimensions and the effective relative permittivity. Equation 2.10 is mentioned and utilized in a lot of work related to the reflectarrays [30] to provide this relation.

$$\varepsilon_{eff} = \varepsilon_r \left(1 - \frac{\pi}{2\sqrt{3}} \left(\frac{d_h}{d_h + p} \right)^2 \right) + \frac{\pi}{2\sqrt{3}} \left(\frac{d_h}{d_h + p} \right)^2 \quad (2.10)$$

where d_h and p are the hole diameter and the period between two adjacent holes, respectively. This equation is plotted in Figure 2.21 to illustrate the validity range of the effective relative permittivity via perforation, where the value of p is taken to be 0.25 mm , which is the minimum recommended value by the fabrication machine. The minimum possible hole diameter is 0.2 mm due to the used milling machine, while the maximum hole diameter considered is about 0.8 mm to ensure that the medium will act in a homogenous way and give the required behavior. The value of 0.8 mm is less than one tenth of the wavelength at the maximum frequency within the operating bandwidth. It can be seen easily from this figure that the valid implemented range using this perforation starts at 1.45 and ends at 1.9. The selected values of the relative permittivities should be, somehow, far from the edge of these boundaries to have a realizable design. This leads to the previously mentioned chosen values of the dielectric constants of both matching sections (1.8 and 1.58). The required initial value of the hole diameter is obtained from Figure 2.21. Equation 2.10 has been

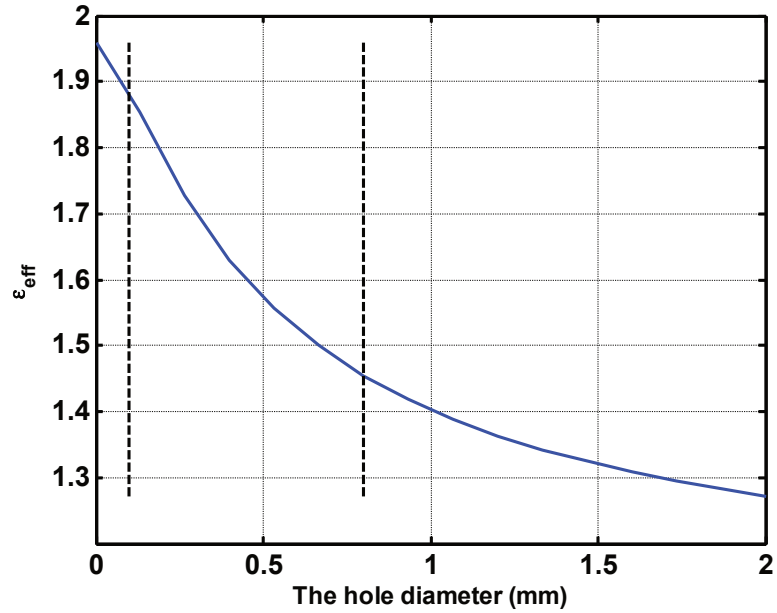


Figure 2.21: The relation between effective relative permittivity and the hole Diameter.

deployed in reflectarray problems, where the wave is incident normally on the top face of the perforated substrate. The selected values of the hole diameters should be verified and tuned to achieve the required dielectric constant. A numerical extraction for the relative permittivity is performed by simulating a parallel plate waveguide filled with the perforated substrate; then the relative permittivity is extracted from the phase of S_{21} as the mode propagating, in this case, is pure TEM mode. Figure 2.22 shows the extracted value of the relative permittivities with the frequency after tuning to obtain the requested dielectric constants in the design. Considering these values of the hole diameters in the perforated sections and building up the model, Figure 2.23 is obtained to show the scattering parameters of the final design of the transition printed on RT5880LZ substrate. The final dimensions of the matching sections are listed in Table 2.3.

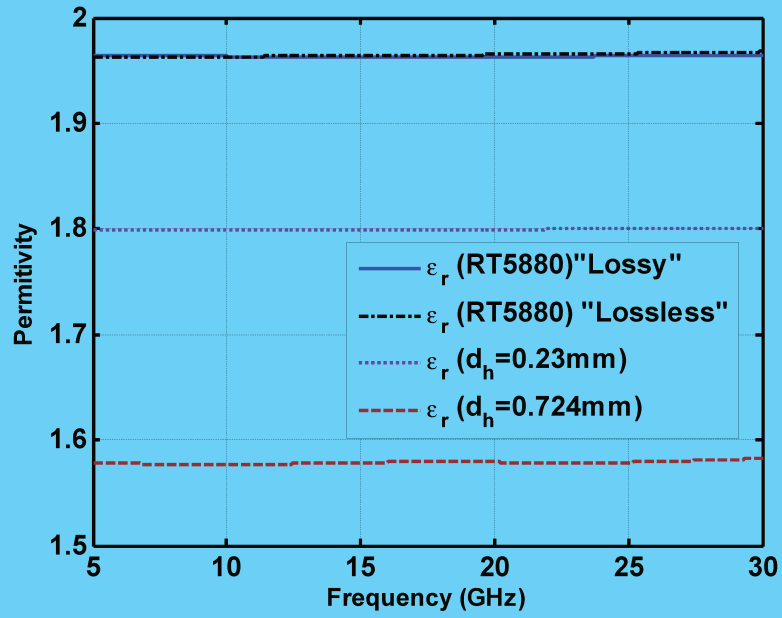


Figure 2.22: The extracted relative permittivity using the parallel plate model.

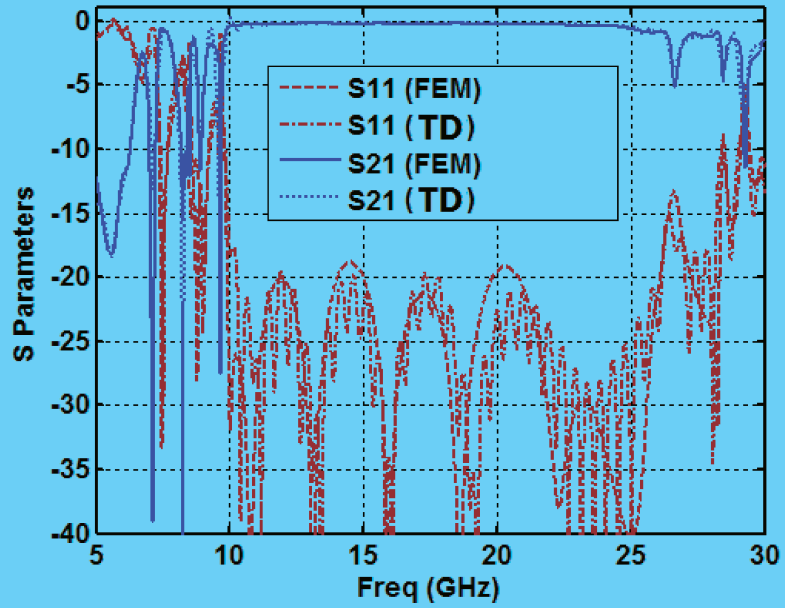


Figure 2.23: The scattering parameters of the final transition design with perforated substrate.

Table 2.3: The final dimensions of both matching sections

Matching Section 1		Matching Section 2	
The Section Length	4.31	The Section Length	3.91
The Ridge Width	2.32	The Ridge Width	2.43

2.4 RGW Measurement Setup

The transitions shown in this chapter provide excellent performance. These transitions can be used as basic elements in the measurement setup of various ridge gap waveguide components. Some matched loads have been made as well as through section to be used in calibration. After having these transitions, we should have an accurate evaluation of the ridge gap waveguide bandwidth. This point will be addressed in the following chapter in details.

Chapter 3

RGW cell analysis and BW enhancement

The traditional methodology of the RGW analysis starts with the cell analysis. This analysis is performed in the literature by solving the cells through the eigenmode solution. The stop band of the cell is always considered as the operating bandwidth of the ridge gap waveguide. In this procedure, there are two major drawbacks. The first one is the dependency on the Eigenmode solution without verifying the outcomes experimentally, especially that, this simulation methodology can easily give a wrong indication of a superior mode. The second drawback is that the ideal cell simulated through the Eigenmode simulator assumes the infinite periodicity and neglects the effect of the ridge presence and the finite number of cells. Both have non-negligible effects on the operating bandwidth. In this chapter, both problems are discussed and solved in detail. The first part of this chapter introduces a new methodology for experimental validation of the dispersion relation. This method can be used to validate the outcomes of the eigenmode solutions. The second part of this chapter criticizes the traditional methods for RGW bandwidth determination process and suggests some techniques for bandwidth calculation and enhancement.

3.1 RGW Cell Dispersion Relation in the Literature

The first step in the design procedure of such a configuration is the cell analysis and design. The cell analysis is performed by the Eigenmode solver, which is available in many simulation tools. In this simulation technique, the infinite periodic boundary conditions are assumed, and the final solution is the valid values for the propagation constant corresponding to different values of frequencies to specify the dispersion relation for various modes inside the required structure. Although this methodology is well established, no experimental setup can be configured to implement these boundary conditions. The RGW measurement as a whole was introduced before in many articles [10,12], but no measurement setup is presented to characterize the unit cell alone. In the literature, the primary concern about the RGW unit cell is always the stop band of the cell and the possible techniques to widen this band [29,31], which is directly related to the usable frequency band for the whole circuit. Not much attention is given to the cell analysis accuracy and validation. Theoretical approaches are presented, in the literature, to obtain expressions for the dispersion relations of the bed nail unit cells (BNUC)s. Despite neglecting some boundary conditions in these trials, some of these expressions results are pretty close to the Eigenmode solution results [32,33], where the fields are solved inside the real BNUC structure. In other presented papers, an equivalent surface impedance is assumed to have more simple mathematical manipulations [34].

Some trials are presented in many articles to obtain the mode dispersion relation given the fields inside the structure [35,36]. The methodology, presented in [36], utilized the FDTD solution to extract the dispersion relation of all modes. This technique can never be implemented practically as it depends on having full knowledge about the fields inside the Device Under Test (DUT), while, in practical cases, it is only valid to perform the measurement outside the DUT at the ports. Moreover, the dispersion relation can be obtained, regarding the periodic structures if each cell can

be resolved into N elements of a well-known behavior connected in a cascaded way. In this simple case, the $ABCD$ matrix representation of one cell is obtained mathematically, then the propagation constant as well as the Bloch impedance can be directly calculated for each cell [3, 37]. Another methodology for extracting the dispersion relation is through the unit cell modeling. Many models are presented to describe the unit cell, especially in metamaterials [38]. The unit cell can be represented as a 2D transmission line model, which leads to extracting the cell properties [39, 40].

The previous discussion can be summarized as follows: if the cell structure is simple or composed of simple elements, the dispersion relation can be obtained in a closed form expression. Another solution is to have a model that represents the cell behavior. Otherwise, the traditional solution is to get this relation numerically either with the Eigenmode solution or with some modified algorithms having the field solution everywhere inside the cell. The objective of our work is to have a simple mathematical algorithm to extract the dispersion relation of a specific structure from the measured scattering parameters. Using the Vector Network Analyzer (VNA), it is a straightforward procedure to obtain the S-parameters for the DUT. The electromagnetic signal is propagating through the DUT in a certain mode or modes then it is collected back by the ports to form the transmitted and the reflected signals. The scattering parameters depend on the propagating modes inside the DUT as well as the relation between the DUT characteristics and the port characteristics. In a two-port network case, there are two interfaces between the DUT and both ports, where the reflection at each port is a function of the difference between the DUT impedance and the port impedance. This simplified description puts emphasis on the fact that the scattering parameters contain the information about the propagating mode inside the DUT joined with the relating values of the DUT and the Ports impedance. The proposed algorithm depends only on the scattering parameters calculated or measured at the port. Although the slotted line measurement technique was well established

many years ago [41–43], it cannot be deployed here due to the difficulty of placing a non-radiating slot above the unit cell region.

In the following part, a detailed description of the proposed mathematical algorithm is presented. This algorithm is introduced to extract the dispersion relation of the DUT from the S-parameters regardless of the type of this DUT, which can be implemented based on measured data. This is followed by a procedure validation by applying the proposed algorithm to two examples of well-known dispersion relations. The selected examples are the ideal parallel plate waveguide and the rectangular waveguide with different filling materials. Then, the algorithm is applied to the target problem. Moreover, the model used to obtain the dispersion relation of the BNUC is presented and the final comparisons between the extracted dispersion relations and those obtained through the Eigenmode solution are shown.

3.1.1 Dispersion Relation Extraction Algorithm

3.1.1.1 DUT Under Single Mode Operation Conditions

The block diagram of the DUT in between the two ports is shown in Figure 3.1, where the wave impedance inside the DUT is assumed to be Z_1 , while the port impedance is Z_0 . The signal passes through the interface between the first port and the DUT then it undergoes an infinite number of reflections between both faces. The total reflected signal is the summation of the first reflection and the series of the back transmitted signals. The total transmitted signal is a summation of the forward transmitted signals. The first forward transmitted component can be described by the multiplication of the signal amplitude times both transmission factors T , T' and the propagation term along the DUT. This will result in $AT T' e^{-j\beta l}$, which can be reduced to $A(1 - \Gamma^2) e^{-j\beta l}$ as T and T' are equal to $(1 - \Gamma)$ and $(1 + \Gamma)$ respectively. For each successive component, the signal reflects twice and propagates a distance of $2l$. The previous term is multiplied by $\Gamma^2 e^{-j2\beta l}$ to consider every successive term.

Based on the previous discussion, the output signal of the second port can be written as follows:

$$S_{out2} = A(1 - \Gamma^2) e^{-j\beta l} [1 + \Gamma^2 e^{-j2\beta l} + \Gamma^4 e^{-j4\beta l} + \dots] \quad (3.1)$$

$$S_{out2} = \frac{A(1 - \Gamma^2) e^{-j\beta l}}{1 - \Gamma^2 e^{-j2\beta l}} \quad (3.2)$$

keeping in mind that the first reflection is $A\Gamma$ and the first component in the back reflected series passes through the first port interface in both directions and reflects on the second port interface once. It is also clear that the signal propagates a $2l$ distance inside the DUT. Thus, the total reflected term is written as follows,

$$S_{out1} = A\Gamma \{1 - (1 - \Gamma^2) e^{-j2\beta l} [1 + \Gamma^2 e^{-j2\beta l} + \Gamma^4 e^{-j4\beta l} + \dots]\} \quad (3.3)$$

$$S_{out1} = A\Gamma \left\{ 1 - \frac{(1 - \Gamma^2) e^{-j2\beta l}}{1 - \Gamma^2 e^{-j2\beta l}} \right\} \quad (3.4)$$

The final forms in Equations 3.2 and 3.4 can be used to obtain an expression for the scattering parameters for the DUT as follows:

$$S_{11} = \Gamma \left[\frac{1 - e^{-j2\beta l}}{1 - \Gamma^2 e^{-j2\beta l}} \right] \quad (3.5)$$

$$S_{21} = \frac{(1 - \Gamma^2) e^{-j\beta l}}{1 - \Gamma^2 e^{-j2\beta l}} \quad (3.6)$$

where the reflection coefficient is assumed to be in the general form of $\Gamma = |\Gamma|e^{j\theta_\Gamma}$.

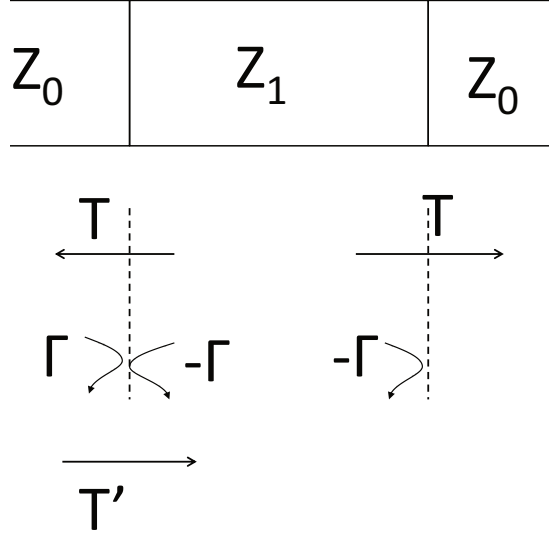


Figure 3.1: The DUT block diagram.

Single Propagating Mode inside the DUT

In this case, a single propagating mode is assumed inside the DUT with a real value of β . Using Equations 3.5 and 3.6, it is straightforward to obtain expressions for the scattering parameters magnitudes as follows:

$$|S_{11}| = |\Gamma| \frac{\sqrt{2 - 2 \cos(2\beta l)}}{\sqrt{1 + |\Gamma|^2 - 2|\Gamma| \cos(2\beta l + \theta_\Gamma)}} \quad (3.7)$$

$$|S_{21}| = \frac{\sqrt{1 + |\Gamma|^2 - 2|\Gamma| \cos(2\theta_\Gamma)}}{\sqrt{1 + |\Gamma|^2 - 2|\Gamma| \cos(2\beta l + \theta_\Gamma)}} \quad (3.8)$$

For any propagating mode inside the DUT, the wave impedance takes a real value with an angle of the reflection coefficient equals to multiple integers of π . Replacing θ_Γ with $n\pi$ will reduce Equation 3.8 to:

$$|S_{21}| = \frac{(1 - |\Gamma|)}{\sqrt{1 + |\Gamma|^2 - 2|\Gamma| \cos(2\beta l + \theta_\Gamma)}} \quad (3.9)$$

The previous equation shows that the transmission coefficient has a periodic behavior. This expression reaches its maximum value of 1 when the “cos” term is equal to 1 and reaches its min value when the “cos ” term is equal to -1 . The minimum value of the transmission coefficient can be expressed by the following equation

$$|S_{21}|_{min} = \frac{1 - |\Gamma|}{1 + |\Gamma|} \quad (3.10)$$

The extraction algorithm depends, mainly, on finding the minima and maxima of the transmission coefficients or the reflection curves over a certain frequency band and equating the “cos” term with ± 1 . Based on the expected value of the DUT impedance relative to the port impedance, whether it is greater or less than the port impedance, the angle θ_Γ will take a value of an odd multiple or an even multiple of π . The previous analysis leads to the following two cases

- Case 1: $\theta_\Gamma = 2n\pi$
 - $|S_{21}|_{max}$ at $2\beta l = 0, 2\pi, 4\pi, \dots$
 - $|S_{21}|_{min}$ at $2\beta l = \pi, 3\pi, 5\pi, \dots$
- Case 2: $\theta_\Gamma = (2n + 1)\pi$
 - $|S_{21}|_{max}$ at $2\beta l = \pi, 3\pi, 5\pi, \dots$
 - $|S_{21}|_{min}$ at $2\beta l = 0, 2\pi, 4\pi, \dots$

The proposed procedure can be described as follows: The DUT is placed in-between two standard single-mode port, and the scattering parameters are obtained “through simulations or measurements as will be done in the coming sections.” The minima and maxima locations in $|S_{11}|$ and $|S_{21}|$ exist when the phase constant equals

to multiple integers of π . The value of $2\beta l$ starts with 0 at the starting propagating frequency, then increases by π at every minimum or maximum, afterward. Finally, repeat the process after each stop band.

To illustrate the meaning of the stop band in this algorithm, the case of the evanescent modes should be addressed, which is the main concern of the following subsection.

Evanescent Mode inside the DUT

In regard to evanescent modes, only inside the DUT, the propagation inside the DUT takes the form of $e^{-\alpha l}$. Based on the assumption that the length of the DUT is sufficient for the signal to collapse, this term will approach zero. In this particular case, Equations 3.5 and 3.6 can be reduced as $S_{11} = \Gamma$ and $S_{21} = 0$, in the case of having enough length to for evanescent mode elimination. It is worth mentioning that the value of Γ is a unity magnitude and general phase as the wave impedance, in this case, has a pure imaginary value. The band of frequencies in which all modes are evanescent is the stop band of the structure. This band ends at the cutoff frequency of the following mode, where β starts at zero as mentioned in the previous case.

3.1.1.2 DUT under Multi-Mode Operation Conditions

This case is more complicated as the equations describing the signal coming out of each port will be a summation of all propagating modes contributions. This is based on the assumption of ignoring the mutual effect between modes and assuming that they are orthogonal. The problem in extracting the dispersion relation through the measured scattering parameters in the multi-mode case is that the measured S-parameters is performed through the network ports. The measured parameters represent the summation of all mode contributions. Thus, Equations 3.2 and 3.4

can be generalized to be

$$S_{out2} = \sum \frac{A_m (1 - \Gamma_m^2) e^{-j\beta_m l}}{1 - \Gamma_m^2 e^{-j2\beta_m l}} \quad (3.11)$$

$$S_{out1} = \sum A\Gamma_m \left\{ 1 - \frac{(1 - \Gamma_m^2) e^{-j2\beta_m l}}{1 - \Gamma_m^2 e^{-j2\beta_m l}} \right\} \quad (3.12)$$

where m stands for the mode number and the summation will be performed over all the propagating modes inside the structure. One major note, in this case, is that the amplitude of each mode is not only a function of the mode characteristics relative to the port characteristics, as described before in the single mode operation, but it is a function also of the ability of the used excitation technique to generate the mode. The methodology that can be used to distinguish between different modes depends on the fact that each mode has its phase constant and its velocity. Having an accurate time-domain experimental setup with sufficient resolution can utilize the time slot in which only one mode contributes to the output signal. Repeat the same algorithm in the second time slot in which two modes only contribute to the output signal and by subtracting the first mode contribution obtained from the first step and so on to include a certain number of modes. This process should be repeated until reaching the steady state value within a certain accepted error. It is clear that to reach the steady state value, all modes must be considered, however, in the case of structures that support an infinite number of modes, a finite number should be considered with an accepted percentage error.

The investigated RGW unit cell in this work is operating in the Ku and K bands. In order to differentiate between the modes exist within the same frequency band in this structure, a time domain setup with a resolution order of 10^{-15} second is needed, which is hard to achieve. Applying the proposed algorithm presented in the previous section, in the single mode case, results in having an effective dispersion relation for the existing modes. This leads to having a deeper physical insight for the propagation

inside the proposed setup.

In summary, if the DUT carries more than one mode, the measured parameters represent the summation of all modes. To distinguish between these modes, a high-resolution time domain measurement setup has to be deployed. The time domain setup will depend on the velocity difference between modes and determine the time slot in which only one mode exists. As this high-resolution time domain setup is not available, the extracted dispersion relation represents an average effect of the modes. A complete subsection is reserved to discuss the results obtained in the frequency band in which two modes can propagate. In this subsection the single mode equations are applied, even in the frequency band where multimode exist, to obtain an effective value for the phase constant in this frequency band.

3.1.2 Procedure Validation on Bench-Mark Examples

In this section, two different examples of well-known characteristics are given. These two examples are used as validity checks for the algorithm. The first example is an ideal parallel plate waveguide with a linear dispersion relation, while the second example is a rectangular waveguide.

3.1.2.1 Example1: Parallel Plate Waveguide

The proposed example contains three successive parallel plate waveguides of the same width and height but with different filling materials. The middle section, which is an air-filled section, is the DUT. The two terminal sections are filled with a dielectric of $\epsilon_r = 4$ as shown in Figure 3.2. The parallel plates in this example are assumed to be ideal. The fringing fields are eliminated by applying perfect magnetic conductor (PMC) boundary conditions on the side walls. Performing the simulation then applying the proposed algorithm on the exported scattering parameters, the dispersion relation can be extracted for the DUT. Figure 3.3 shows the scattering parameters

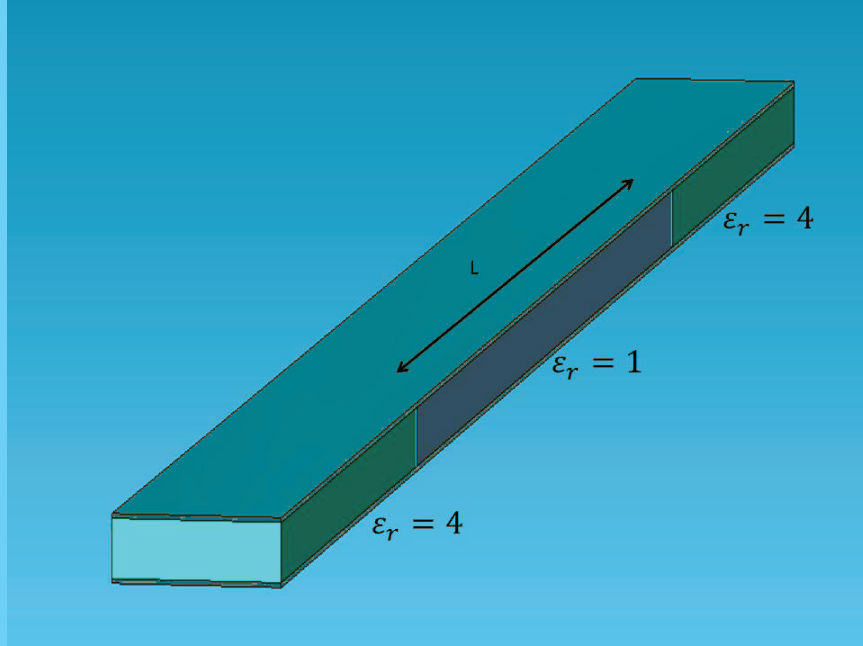


Figure 3.2: The parallel plate example block diagram.

of this example, while the comparison between the dispersion relation extracted from the proposed algorithm and the exact one is shown in Figure 3.4. The exact dispersion relation of the parallel plate waveguide can be written as follows:

$$\beta = \frac{\omega}{v_{ph}} \quad (3.13)$$

where $v_{ph} = c = 3 * 10^8$ m/sec as the DUT is an air-filled guide that supports a TEM mode.

3.1.2.2 Example2: Rectangular Waveguide

The previous example validates the algorithm in the case of linear dispersion relation. In this example, the structure has a stopband followed by a passband. The dispersion relation is a nonlinear curve within the passband. The same setup is investigated with three successive guiding structures of the same dimensions and different filling materials. The DUT is an air-filled rectangular waveguide, and the terminal lines are two identical rectangular waveguides filled with $\epsilon_r = 4$ as shown in Figure 3.5. It is

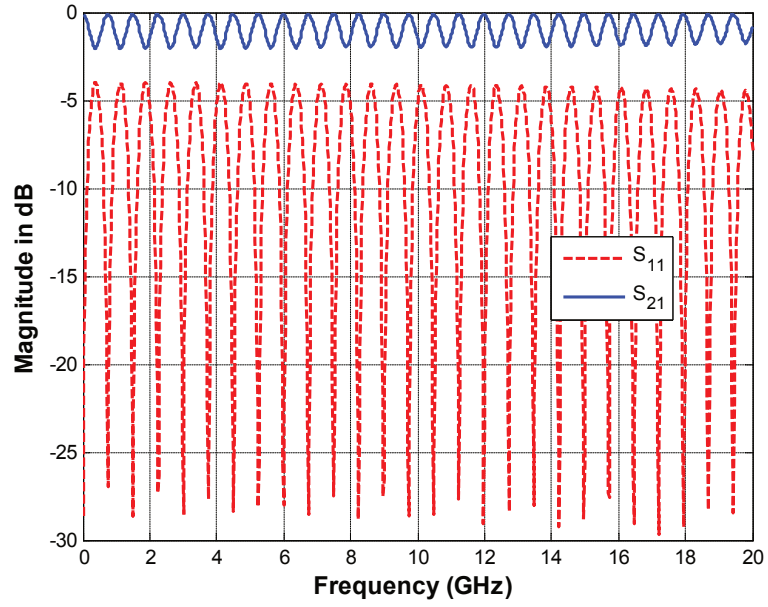


Figure 3.3: Scattering parameters of the parallel plate example.

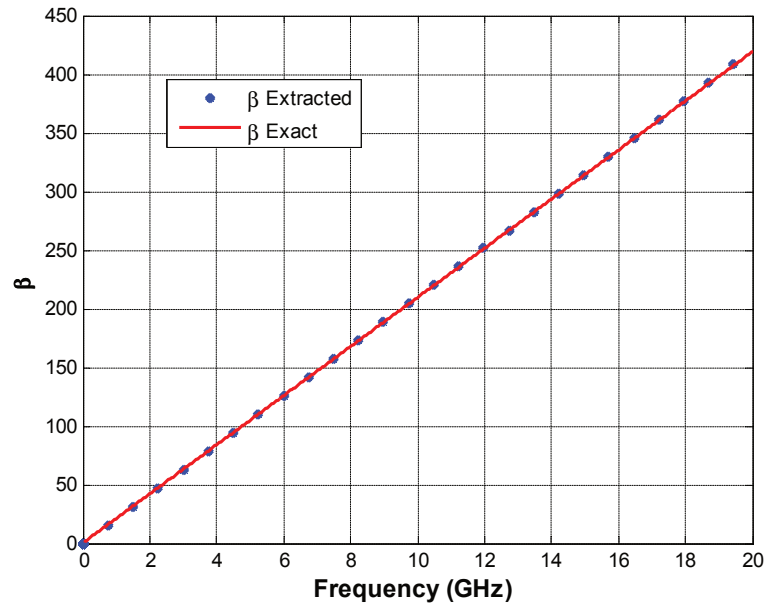


Figure 3.4: The parallel plate example: dispersion relation.

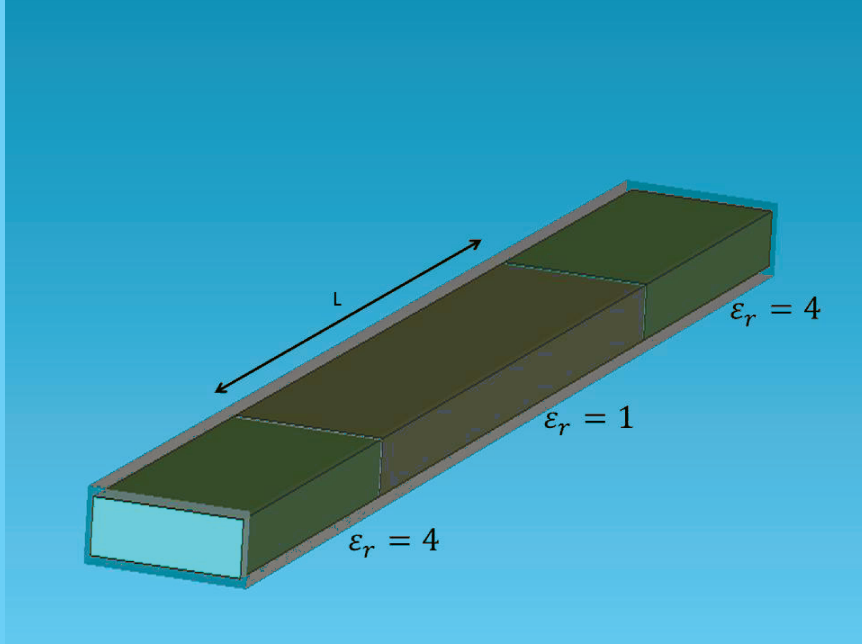


Figure 3.5: The rectangular waveguide example block diagram.

essential to mention that the port, itself, has its own cutoff frequency. This means that the solution is valid only beyond this frequency. The Scattering parameters of the prescribed setup are shown in Figure 3.6. Applying the proposed algorithm, the comparison between the dispersion relation extracted and the theoretically expected one is shown in Figure 3.7. The theoretically expected value of the phase constant can be written in the following equation

$$\beta = k_0 \sqrt{1 - (f_c/f)^2} \quad (3.14)$$

where k_0 is the free space wave number ($k_0 = \frac{\omega}{c}$) and f_c is the cutoff frequency of the rectangular waveguide dominant mode ($f_c = c/2a$)

It is indicated in this figure that there is a region before the cutoff frequency of the measurement setup in which the algorithm cannot be applied due to the setup limitations.

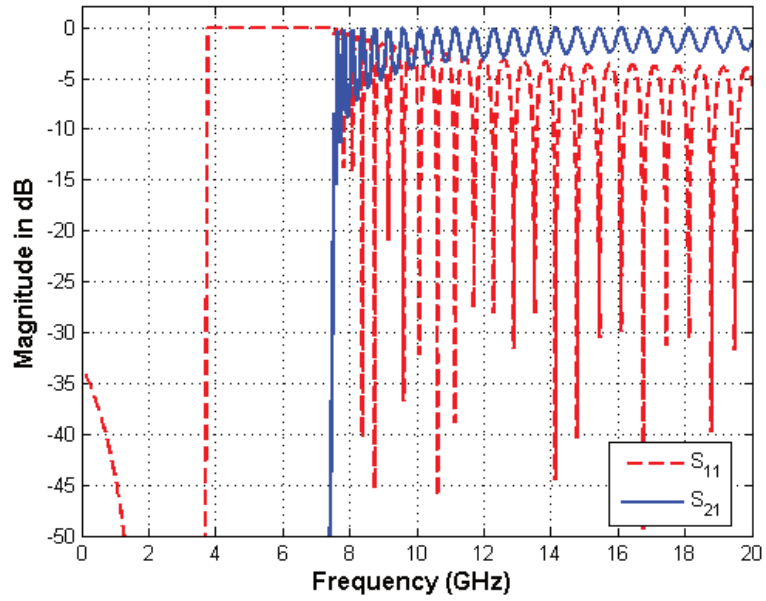


Figure 3.6: Scattering parameters the rectangular waveguide example.

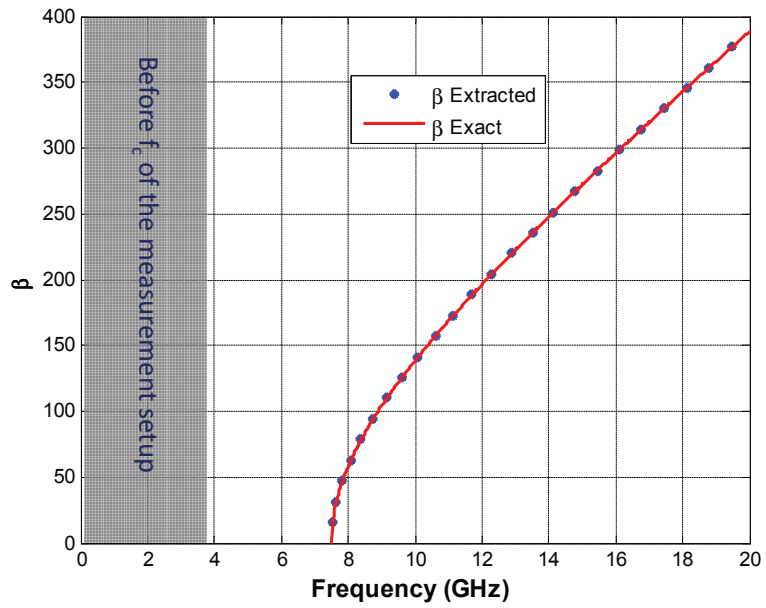


Figure 3.7: The rectangular waveguide example: dispersion relation.

3.1.3 Ridge Gap Waveguide Cells Dispersion Relation

Based on the procedure described and the validation process addressed in Sections 3.1.1 and 3.1.2, the proposed algorithm is applied to the target problem. The primary objective is to implement this algorithm to obtain the dispersion relation of the Bed Nail Unit Cells (BNUCs) used in the RGW configuration. The cell to be investigated in this work is the traditional BNUC shown in Figure 3.8, while the dimensions of this cell are given in Table 3.1, where a is the cell width, b is the pin width, d is the pin height and h is the gap height. Successive rows of the BNUCs are placed inside a Ku-band rectangular waveguide (WR-62). The standard waveguide utilized in this experiment is the WR-62, which has a height of 7.9 mm. On the other hand, the gap height of the unit cell is 0.5 mm. This created the need for a transition due to the difference in heights. A tapered transition is added to eliminate the sudden change in the height of the waveguide, while keeping the gap above the pins with the required value. However, it is possible to design a coaxial probe transition directly in the ridge gap. It should be taken into consideration that the bandwidth will be limited by how good this transition between the coaxial probe and the ridge gap is. It is believed that the bandwidth will be smaller than the waveguide bandwidth. The proposed configuration to test the BNUC is shown in Figure 3.9. The scattering parameters for the whole setup are shown in Figure 3.10. The proposed algorithm is applied to the actual problem to obtain the dispersion relation of the BNUCs through measurements. It can be depicted from Figure 3.11 that the results generated based on the proposed algorithm are very close to the results calculated with the Eigenmodes numerical technique. Many aspects that should be taken into consideration in the process of applying the presented extraction algorithm for the dispersion relation. The proposed technique is bounded by the measurement setup limitations. In the proposed case, for example, no curve can be extracted before the dominant mode cutoff frequency of the Ku-Band rectangular waveguide. It is evident, also, after the cutoff frequency

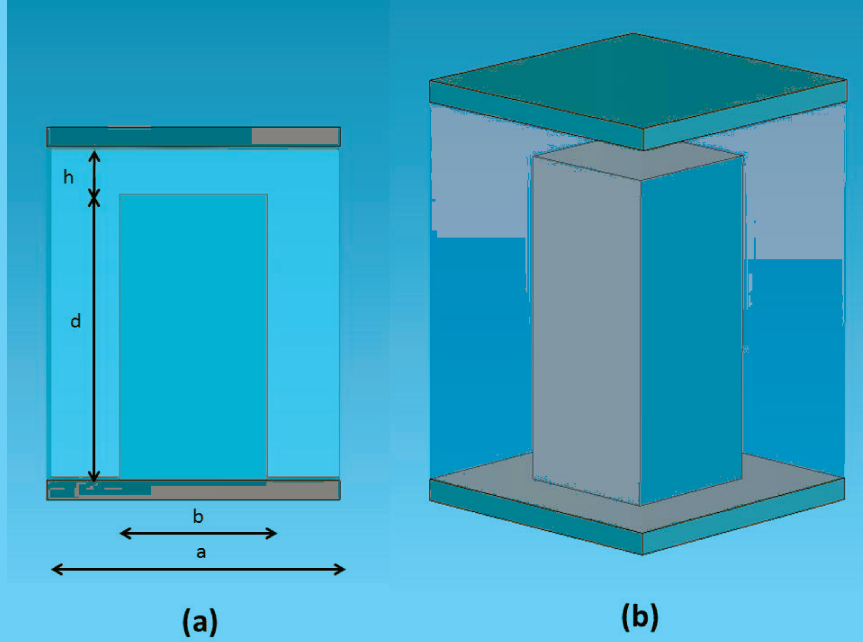


Figure 3.8: The cell configuration (a) Side view (b) 3D view.

of the second order mode, some higher order modes can be generated, and it may result in some deviations in the phase constant value. The straightforward solution to this problem is to repeat the measurement of the cells in different measurement setups and extract the curve in the stable band of the setup guide. In the frequency range where two modes exist, the wave propagates inside the cells region in the form of two different modes; then both modes will be superimposed on the port region. It is a must to have another diversity in order to distinguish between these two modes. As mentioned before, the difference in velocities between all modes enables the time domain measurement to differentiate between the modes. This can be done only if a time domain measurement setup exists with the required resolution. Although the algorithm is limited by the availability of the accurate time domain setup to differentiate between the two modes, applying the proposed technique in the case of two modes results in having an average behavior for the dispersion relation within this frequency band.

Table 3.1: The bed nail unit cell dimensions.

The Dimension	The Value (in mm)
a	3.17
b	1.6
d	3
h	0.5

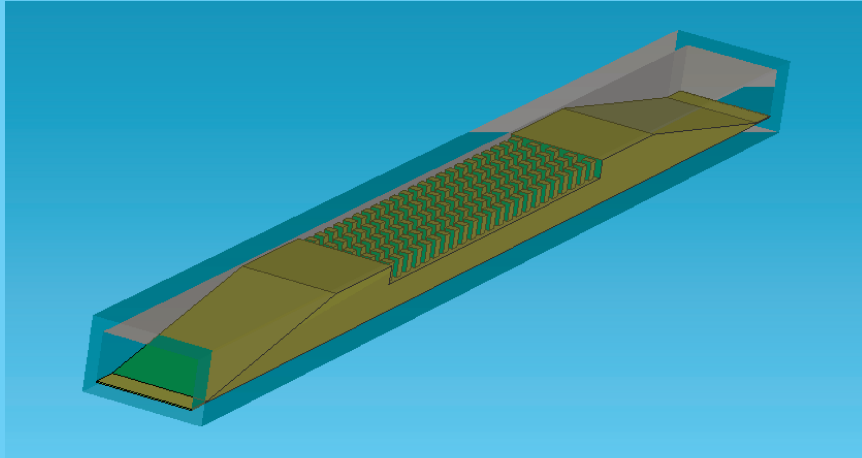


Figure 3.9: The measurement setup for BNUCs testing.

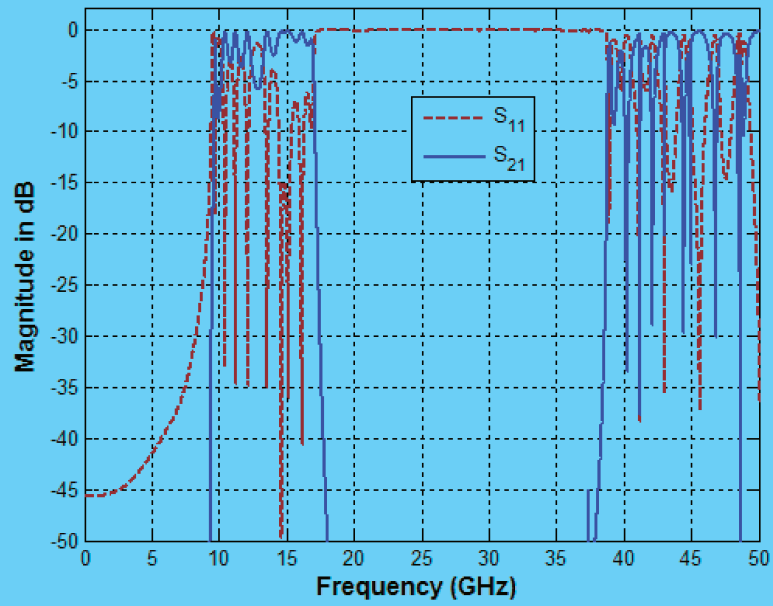


Figure 3.10: The scattering parameters of the BNUCs inside a rectangular waveguide.

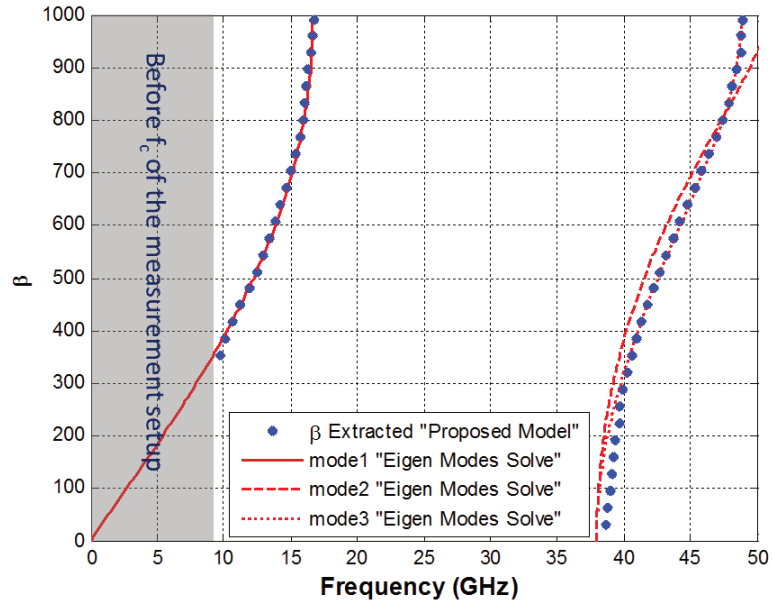


Figure 3.11: The comparison between the dispersion relations extracted by the proposed method and the eigenmode solution.

3.1.3.1 The Multi-Mode Band Results Interpretations

The results shown in Figure 3.11 lead to clear observations. The first observation is that the extracted stop band is slightly larger than the theoretical one obtained numerically through the Eigenmode solution. This band increase is expected as the proposed measurement setup deals with finite periodicity, while the simulated BNUC structure in the Eigenmode solver is assumed to have infinite periodicity. The second observation is that the extracted curve of the dispersion relation is closer to Mode 3 obtained from the Eigenmode solution. The conclusion of this observation is that this mode is the only excited mode, or at least it has a dominant effect. This gives more physical insight to the problem. To make sure that this observation is correct the fields of both modes are plotted using the Eigenmode solution in Figures 3.12 and 3.13. These figures represent the field distribution of the second and the third mode inside the unit cell through the Eigenmode solution. These figures indicate that the two polarizations are, almost, of the same magnitude in Mode 2 case, while in the

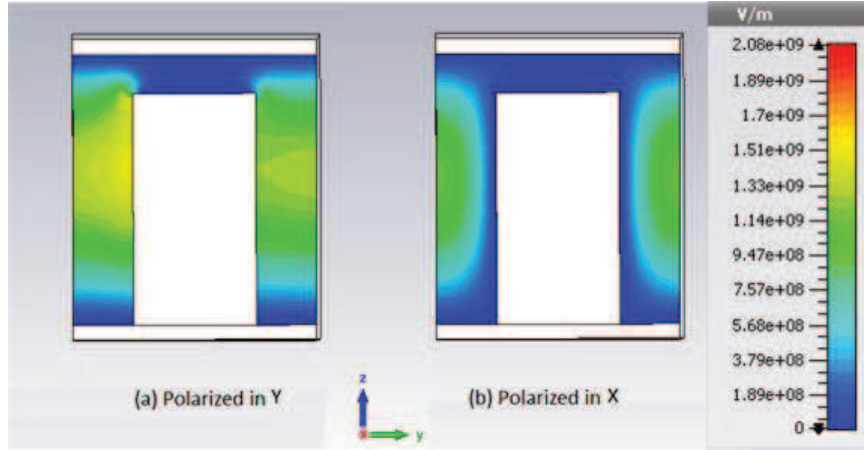


Figure 3.12: The field distribution of Mode 2.

case of Mode 3, the magnitude of one field component is five times the orthogonal one.

By simulating the proposed setup and sketch the field distribution inside this frequency band the previous conclusion is proved to be true. It can be depicted from Figure 3.14 that the two orthogonal components around the pins inside the proposed setup are of different order of magnitudes. This emphasizes that Mode 3 has a dominant effect in this setup. Finally, although high-resolution time domain setup is mandatory to distinguish between two very close modes, applying the proposed algorithm has remarkable benefits on the physical picture even in the absence of this equipment.

3.1.4 Measurement Results of the RGW Dispersion Relation

The setup shown in Figure 3.15 is used to obtain the dispersion relation of the RGW practically. The number of successive cells fabricated is 23 cells. This long structure ensures that all evanescent modes inside the cells region will die out. The large number of cells is selected to obtain a closer behavior to the periodic unit cells through performing the experiment with a finite number of cells. It is important to mention that the structure is slightly modified by adding a thin protrusion to ensure the gap

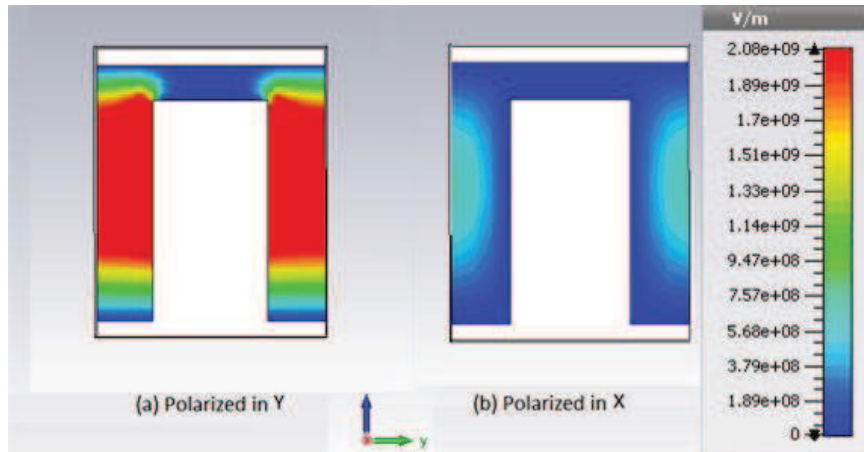


Figure 3.13: The field distribution of Mode 3.

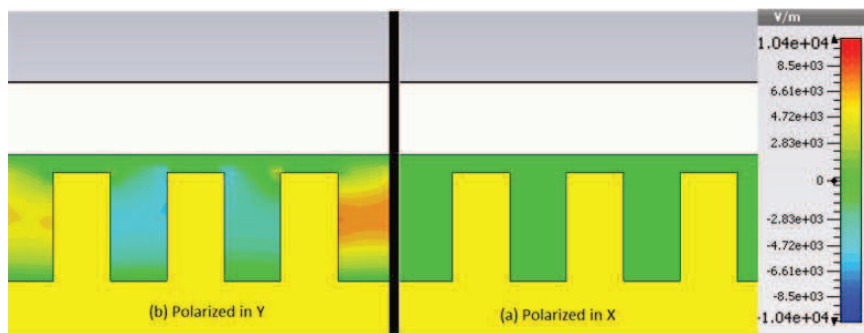


Figure 3.14: The field distribution inside the structure.

height with the required dimension. Two standard transitions are used to obtain the results through a vector network analyzer (VNA). These two transitions transfer the signal from the standard 2.92 mm connector to the WR-62 standard waveguide. These transitions operate in the standard WR-62 frequency band from 12.4 to 18 GHz. This puts some limitations on the extracted dispersion relation. The bandwidth limitation does not exist in simulating the structure as wave ports are deployed. The number of modes in each port can be controlled in the simulation tool to ensure only one mode propagation in the waveguide, even beyond the cutoff frequency of the second propagating mode. This leads to the dispersion relation of the RGW for extremely large bandwidth using a single simulation, as discussed in the previous section. On the other hand, in the real setup, the used excitation technique limits the extracted results to be valid only in the operating bandwidth. Performing the scattering parameters measurements and after the waveguide calibration, Figure 3.16 is obtained, where the measured reflection coefficient is compared with the simulated one. The fabricated parts are machined with a tolerance of 0.002 inches, which is over 5% of the gap height value "*The most critical parameter in the ridge gap unit cells*". This results in some discrepancies between the simulated and measured results. This curve is limited to the frequency band till 18 GHz as the available adapter in the lab works only in the standard Ku-band till 18 GHz. The matching level of this adapter is not acceptable beyond this band. The measured curve is utilized to extract the RGW cell dispersion relation through the proposed algorithm. In the previous discussion, it is mentioned that the proposed algorithm can utilize the minima and the maxima of $|S_{11}|$ or $|S_{21}|$. In this case, it is easier to detect the minima of $|S_{11}|$. Figure 3.17 illustrates the comparison between the extracted dispersion relation via the measurement setup and the Eigenmode solver results. It is clear that the extracted results are shown only in the operating bandwidth. The bandwidth limitation is due to the deployed measurement setup as the rectangular waveguide used is the standard

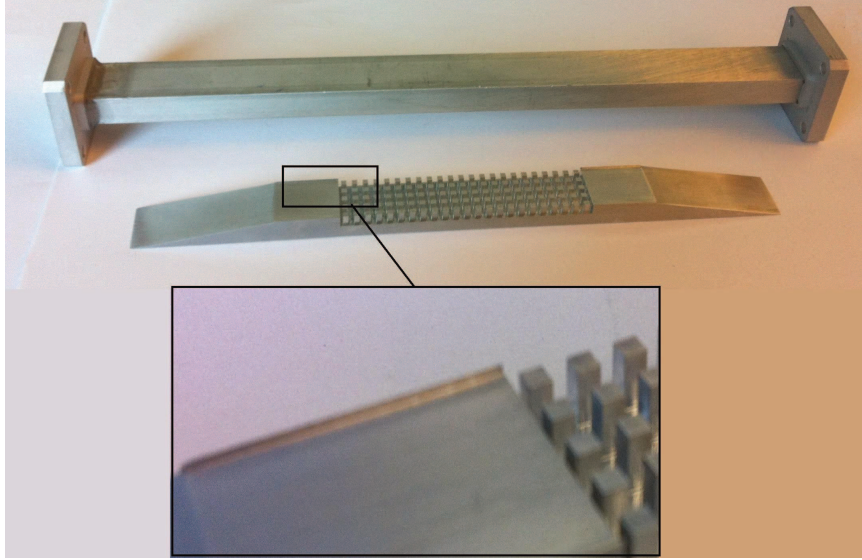


Figure 3.15: The measurement setup to extract the RGW dispersion relation.

WR62 waveguide.

3.1.5 Utilizing the Dispersion Relation in the RGW Design

In this section, the previous relation is used in the design process of the RGW to provide an application and emphasize the importance of the accurate dispersion relation. The Ridge Gap Waveguide is constructed of the parallel plate-like structure with the ridge acts as the lower plate and a large ground on top of the whole structure. The gap height of the cells is identical to the separation between the ridge and the upper ground plate. The ridge height is equal to the pin height of each cell. The ridge width is designed to have a 50Ω line. A starting value can be calculated from the parallel plate characteristic impedance equation $Z_0 = \eta \frac{h}{W}$ or with better accuracy through the expression of the strip line, where $Z_{0, RGW} = 2Z_{stripline} = 2\frac{\eta}{4} \left[\frac{W}{2h} + 0.441 \right]^{-1}$ [3]. In fact, the characteristic impedance of the RGW is studied many times before [10, 44–46], where the extracted value of the characteristics impedance is utilized in many applications [15, 47]. In addition, the value of the characteristic impedance for the RGW has been a little bit less than the values calculated through the stripline method.

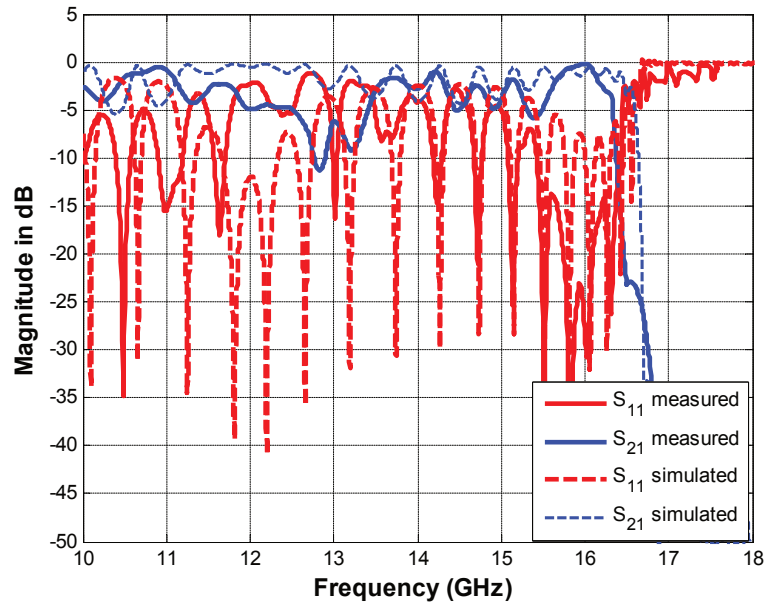


Figure 3.16: Comparison between the measured and the simulated scattering parameters.

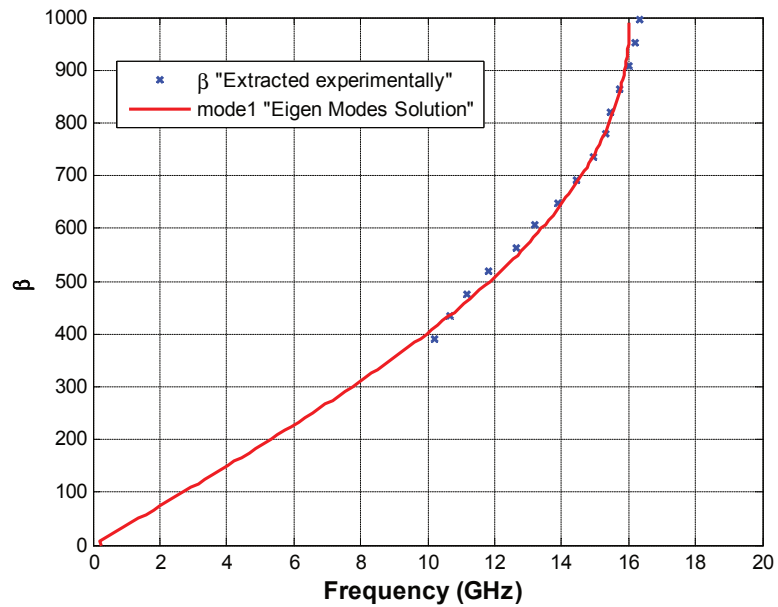


Figure 3.17: Comparison between the extracted experimentally and the simulated dispersion relation.

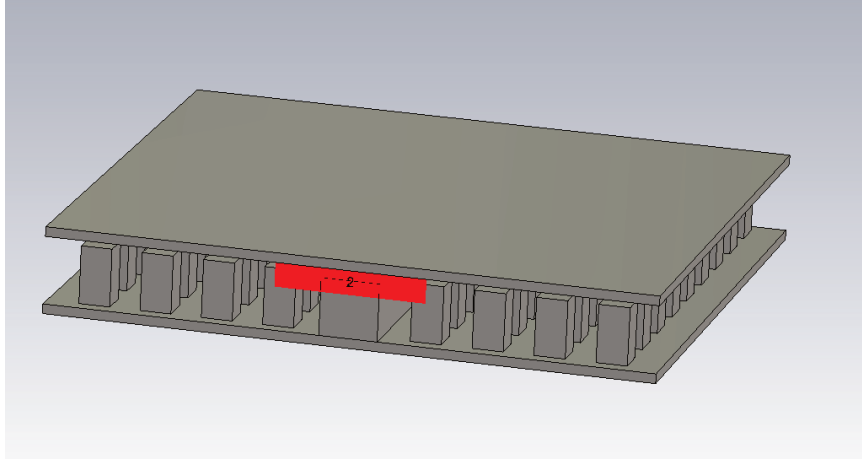


Figure 3.18: Straight ridge gap waveguide.

This can be compensated by decreasing the width of the ridge. Figure 3.18 shows a 50Ω ridge gap straight waveguide surrounded by the investigated cell in the previous section excited by a wave port. The scattering parameters of the previous line are shown in Figure 3.19. This figure illustrates the performance of the RGW as it provides the guidance of the signal within the stop band of the BNUCs. On the other hand, this guidance is lost out of this band, where specific modes can penetrate the BNUCs. The propagation constant of these modes is described through the dispersion relations discussed in the previous sections. The bandwidth of the structure can be depicted from the insertion loss curve: starting around 17 GHz and ending before 39 GHz, which matches the results obtained from the dispersion relation of the cells. It is worth mentioning that the bandwidth in this structure is not measured only by a specific matching level as it may occur that the reflection is below a certain level, while the wave is subjected to leak out of the guide. Another step to verify the signal confinement within the usable frequency band is to plot the normalized field over a cross section of the structure at different frequencies. This normalized field is plotted in Figure 3.20, and this confirms the wave guidance at different frequencies inside the operating bandwidth.

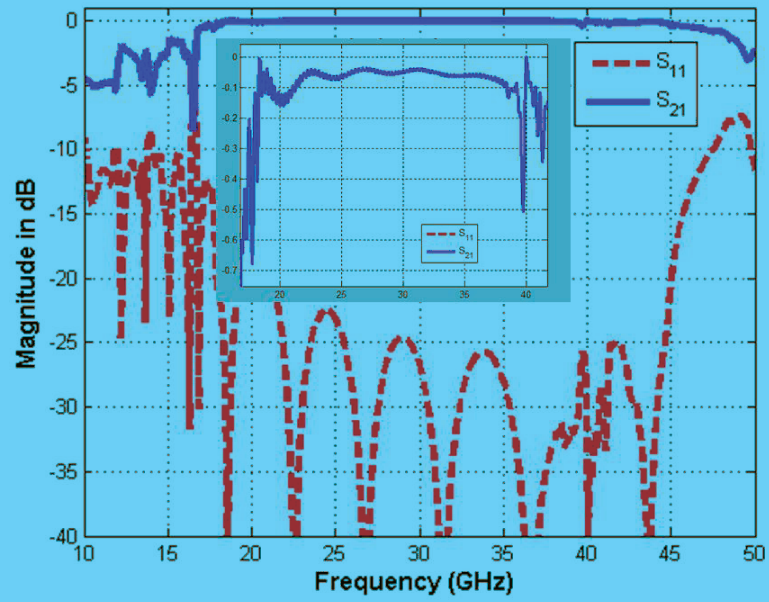


Figure 3.19: The scattering parameters of a straight RGW.

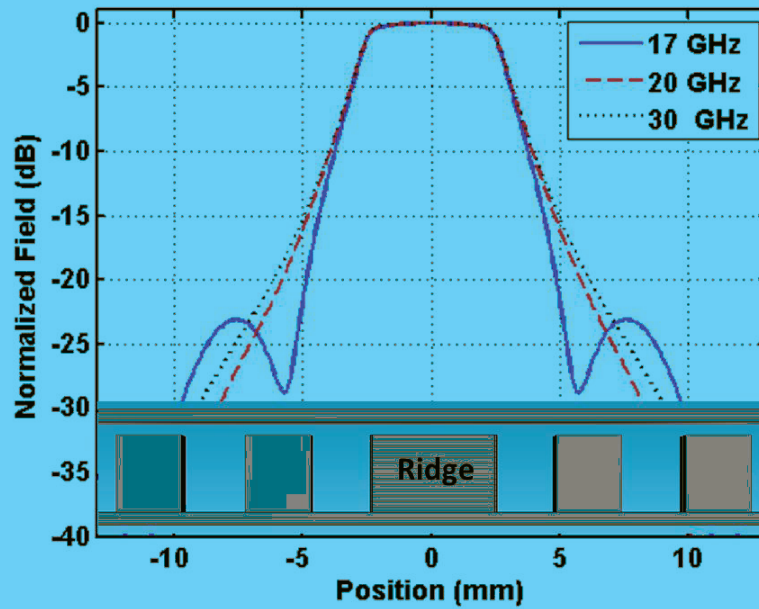


Figure 3.20: The field distribution over a cross section of the straight ridge gap waveguide.

3.2 Ridge Gap Waveguide Bandwidth

Previous research has proposed the utilization of the RGW in many applications such as antennas and antenna arrays [23, 24]. In addition, other microwave devices have been developed based on this technology as filters, couplers, and power dividers [14, 45, 48]. One key element in any application is its operating bandwidth, which is supposed to be the stop band of the unit cells surrounding the ridge. This created a strong motivation to introduce novel cells with wider bandwidth to support the development of wideband applications. The possible bandwidth of the traditional cells is about 2.5:1 and a lot of work have been done to present wider band cells approaching 3:1 in some cases [17]. In the previously studied shapes, the pyramidal and cone shapes have shown a promising behavior for wide bandwidth [29, 31], but it is extremely difficult to fabricate such a structure. Another important point is that the unit cell bandwidth is very sensitive to the gap height, where tiny gap height provides very broadband unit cells. However, this is limited by the fabrication mechanism. Another drawback of minimizing the gap height is its effect on the matching of the structure as a result of changing the ridge characteristic impedance.

In this part, a detailed study is presented to illustrate the realized bandwidth in the ridge gap waveguides and how it is related to the possible bandwidth provided by the unit cells. This study includes the traditional square cross-sectional unit cells as well as the cone-shaped unit cells due to its remarkable wide bandwidth. A novel unit cell is also presented to introduce a printed cone shaped unit cell in order to overcome the barrier in fabricating the cone shape cell. Then, a comparison between four different types of unit cells is made. This is followed by a study of the gap height effect on the bandwidth and illustration of simple solutions for keeping the characteristic impedance at the same value in the case of small gap heights. A separate subsection is dedicated for RGW of zero gap height, where the operating bandwidth is studied as well as a closed form expression is derived to calculate the cutoff frequency of

the proposed structure. The testing section introduces the configuration used to test the bandwidth for the proposed cells and the comparison between the measured and simulated results.

3.2.1 The Realized Bandwidth Vs the Possible Bandwidth

As mentioned in the previous section, current research in RGW is focused on increasing the bandwidth of the individual cell. However, the utilized bandwidth is affected by the ridge existence in the final structure. In this section, four different cell structures are studied. In each case, the individual cell dispersion relation is studied along with the dispersion relation in the existence of the ridge. The first step is to examine the two previously published cell structures, the traditional bed of nails unit cells with a square cross section, and the cone shaped unit cell, where Figure 3.21 shows the structure and the dimensions of both cells. For a fair comparison, the cell size, the nail height and the gap height are kept at the same value for both cells, which are listed in Table 3.2. The top cone diameter and the pin width equal to 3 mm, while the cone base diameter is half this value. The dispersion relation of the square cross section unit cell and the cone shape unit cell is shown in Figure 3.22 (a) and (b), respectively, where the bandwidth ratios in these two cases are 2.39 and 2.63. The existence of the ridge introduces some modes in the cell band gap; this results in shrinking the operating bandwidth. The dispersion relation in the presence of the ridge for both cases is shown in Figure 3.22 (c) and (d), where the bandwidth ratios are reduced to be 1.82 and 2.04 respectively. It is important to notice that the bandwidth ratios in the previous two cases are reduced to 76.2% and 77.6% of their initial values due to the existence of the ridge. The reduction percent is the same. However, the realizable bandwidth with the cone is about the same as those for a nail type without the ridge.

The previous observation encourages trying the cone cell with zero radius at the

base. Although it is not practical to have such a cell structure, it is important to investigate the extreme cases to check the validity of the previous phenomenon. Figure 3.23 displays the dispersion relation of the zero base cone cell alone and the same cell dispersion relation in the existence of the ridge. The bandwidth of both cases can be depicted from this figure to be 2.75 and 2.68, which means that the bandwidth after inserting the ridge is about 97.5% of its original value. Not only does the zero base cone shape give the highest possible bandwidth among other shapes, but also it suffers from the lowest possible reduction in the bandwidth in the existence of the ridge. The major problem of this cell is the fabrication barrier, where it is almost impossible to produce such a configuration. This leads to a simple idea of implementing a similar configuration through printing it to a substrate. The proposed configuration, as well as the dispersion relation for both the cell alone and the cell in the presence of the ridge, are shown in Figure 3.24. The used substrate is RT 5880 with a relative permittivity of 2.2, a substrate thickness of 1.575 mm and a metal layer thickness of 35 μm . This substrate is selected for its relatively small dielectric constant to have a close performance of the air-filled cell. The printed cone base dimension is 5.75 mm, while all other dimensions are kept with the same values, as Table 3.2, for a fair comparison. The dispersion relation of the proposed cell, entitled to printed cone cell, shows a bandwidth ratio of 2.12 for the cell alone and 2.04 with the ridge. It is important to mention that although the cell is not symmetrical in geometry, the dispersion relations in both directions are very close to each other. One final problem in the proposed cell is the difficulty in ensuring the electrical contact at the end point of the cone shape, which is assumed in the simulations. The proposed cell is modified to be a grounded printed cone cell, which is shown in Figure 3.25. It can be understood from the same figure that the presented cell has a bandwidth ratio of 2.2, and this is reduced to be 2.02 in the ridge presence. The height of the ground strip is 1 mm, which reduces the nail height and affects the operating bandwidth by

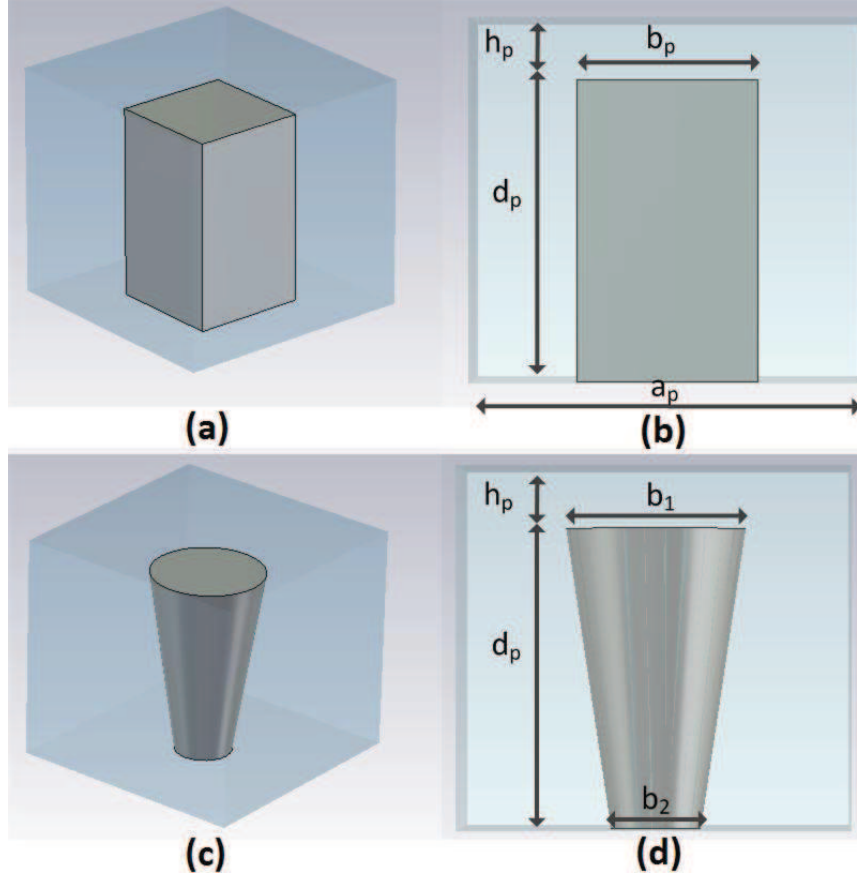


Figure 3.21: The squared cross section bed nail unit cell (a) 3D structure (b) Front view. The cone shaped unit cell (c) 3D structure (d) Front view.

shifting it up as displayed in Figure 3.25.

3.2.2 Gap Height Effect on RGW Bandwidth

The gap height is one of the most effective parameters to control the possible bandwidth of the unit cell. The bandwidth higher limit can be calculated by $f_h = c/2(d+h)$, while the pin acts ideally as PMC surface at $f = c/4d$. It can be concluded,

Table 3.2: The unit cell dimensions of the ridge gap waveguide.

The dimension	The value (mm)
a_p (The cell size)	6.5 mm
d_p (The pin height)	5 mm
h_p (The gap height above the pin)	1 mm

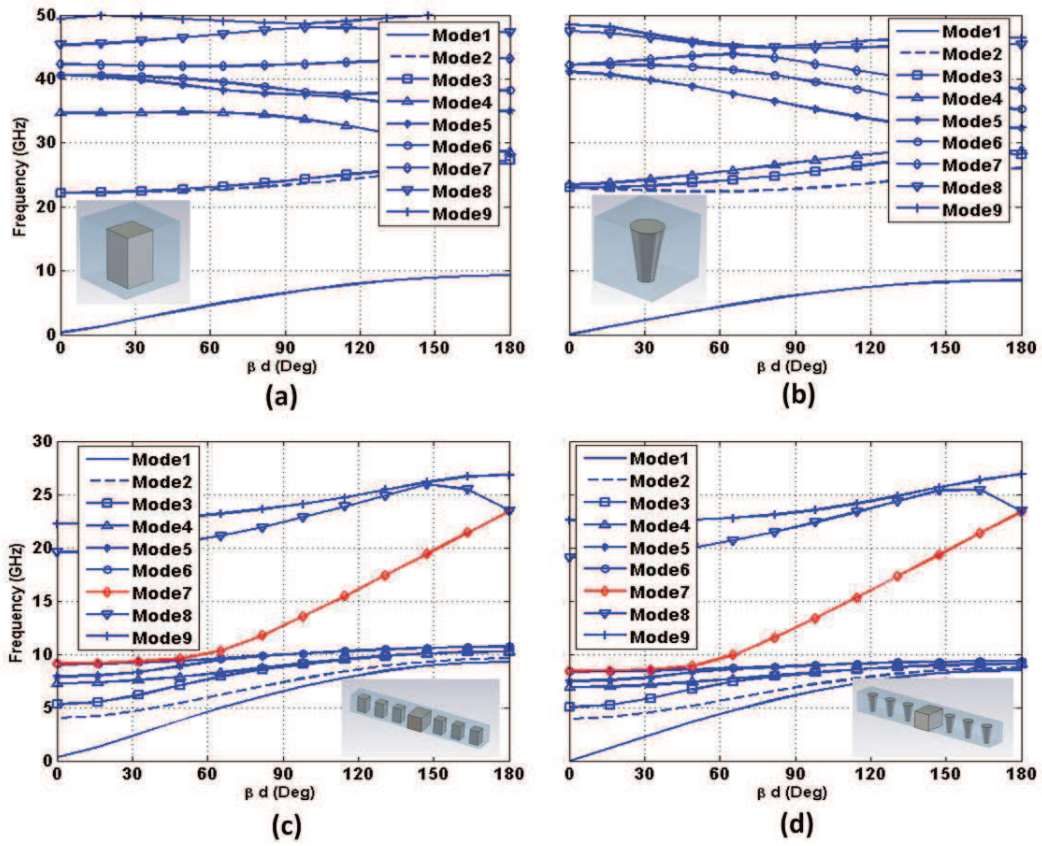


Figure 3.22: The dispersion relation of (a) Square cross-sectional unit cell. (b) Cone shaped unit cell. (c) Square cross-sectional unit cell with the ridge. (d) Cone shaped unit cell with the ridge.

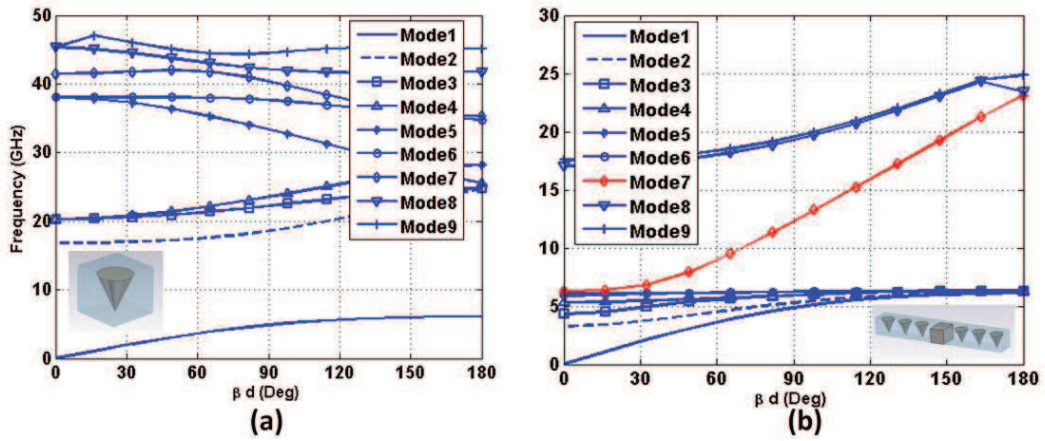


Figure 3.23: The dispersion relation of (a) Zero base cone shape unit cell. (b) Zero base cone shape unit cell with the ridge.

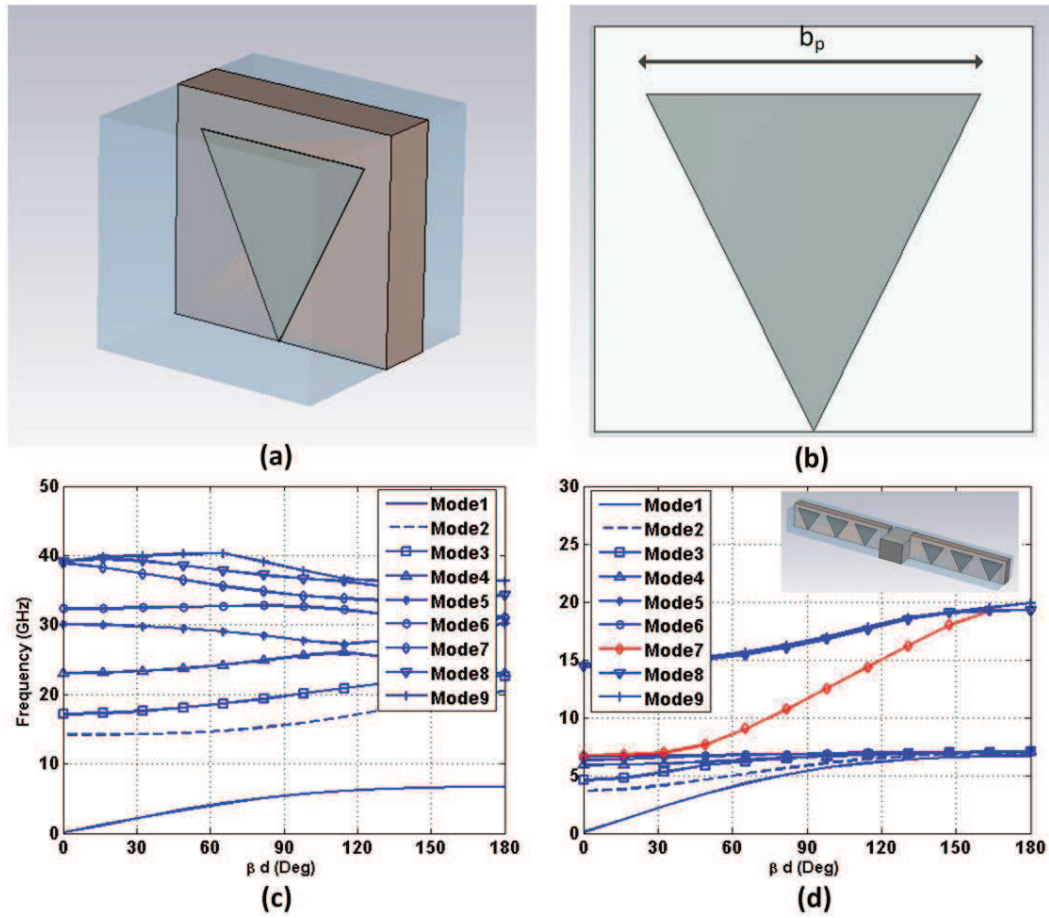


Figure 3.24: The printed cone cell (a) 3D structure. (b) Front view. (c) Unit cell dispersion relation. (d) The dispersion relation in the presence of the ridge.

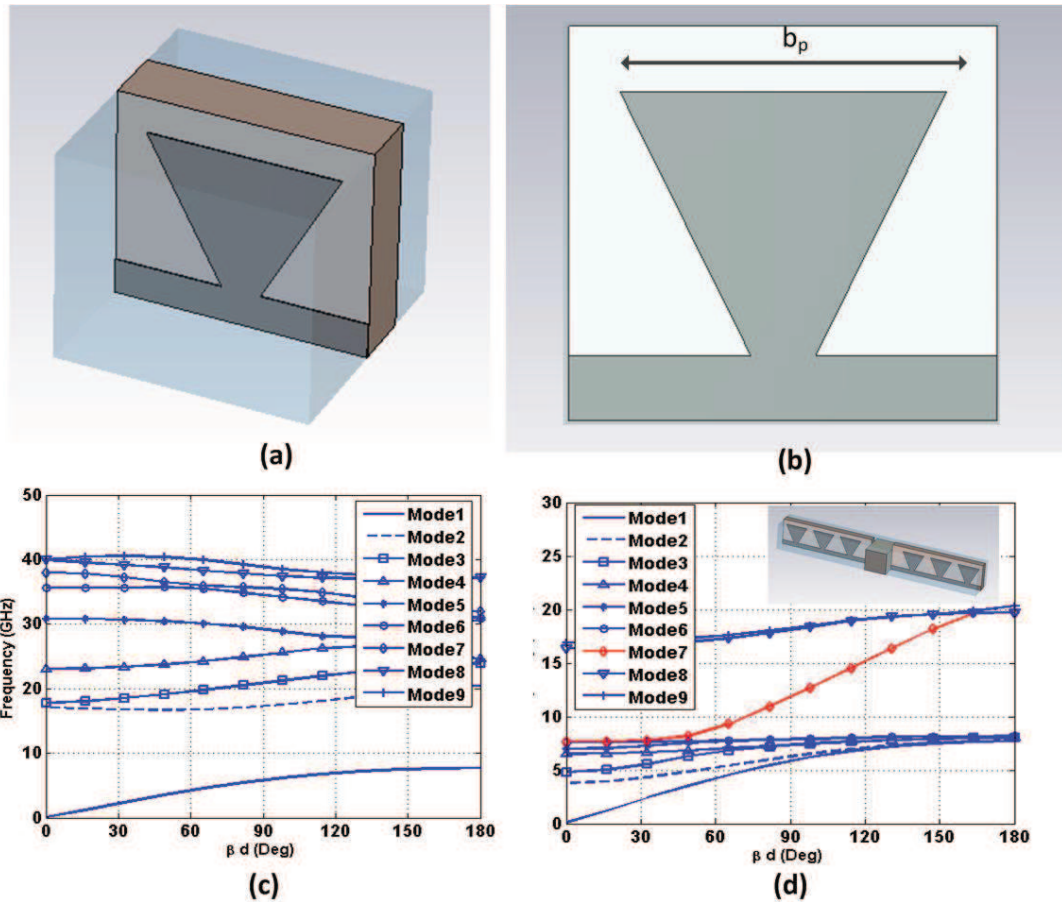


Figure 3.25: The grounded printed cone cell (a) 3D structure. (b) Front view. (c) Unit cell dispersion relation. (d) The dispersion relation in the presence of the ridge.

based on these expressions that the bandwidth increases as the gap height decreases. This was addressed before to have unit cells with extremely large bandwidth in the case of tiny gap heights [29]. To illustrate the gap height effect on the four unit cells discussed in the previous section, the bandwidth ratios of these cells are obtained for different values of the gap height in between 0.5 mm and 1.5 mm. Figure 3.26 gives an indication of the bandwidth ratio behavior with the gap height, where it implies the inverse proportionality between them as expected. This figure introduces a study of the gap height effect on the bandwidth ratio in the case of individual unit cells. As described before the existence of the ridge limits the bandwidth of the individual cell and affects the relation between the gap height and the bandwidth ratio. The gap height effect in the presence of the ridge is shown in Figure 3.27. By visual comparison of these two figures, it is obvious that the zero base cone unit cell has the best performance either alone or with the ridge existence. However, it can be totally excluded due to the fabrication infeasibility. Although the traditional cells show better performance than the printed cone in the individual cell response, the existence of the ridge deteriorates the performance for both traditional cells and has less effect on the proposed unit cell. The grounded printed cone unit cell, in the presence of the ridge, introduces larger bandwidth than the square cross-sectional nail for gap heights more than 0.8 mm and very close bandwidth to that obtained through the cone-shaped cell for gap height 1 mm and more. It should be taken into consideration that the ridge width has to be modified based on shrinking the gap height to maintain the ridge characteristic impedance of $50\ \Omega$. This motivates the discussion of the following two points.

- How to maintain the ridge characteristic impedance at the required level without having a tiny ridge.
- What is the theoretical limit of having zero gap height RGW.

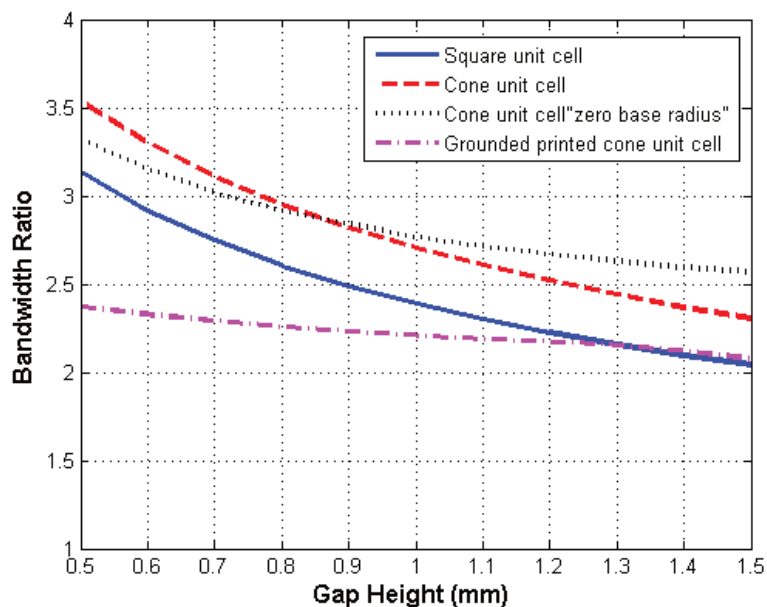


Figure 3.26: The relation between the bandwidth ratio and the gap height for four different cells.

These two points will be illustrated in the coming subsections in more detail.

3.2.2.1 The Dual Gap Height RGW

Through the mentioned relation between the gap height and the possible bandwidth of the unit cell, it is better to decrease the gap height. However, the characteristic impedance of the ridge is proportional to the ratio h_r/W_r , where the parameter " h_r " represents the gap height above the ridge and " W_r " represents the ridge width. This proportionality can be expected in the case of the RGW as one of the parallel plate-like structures. This means that the ridge width should be reduced by almost the same ratio to maintain the required value of the characteristic impedance. In fact, this results in tiny ridge width in the case of tiny gap heights, where it is very hard to be coupled to the signal. The solution to such a problem is, basically, to separate the gap height above the ridge and the gap height above the cells. This leads to having a dual gap height RGW, where the cell gap height h_c takes a different value from that is assigned to the ridge gap height h_r . Figure 3.28 shows the comparison between the

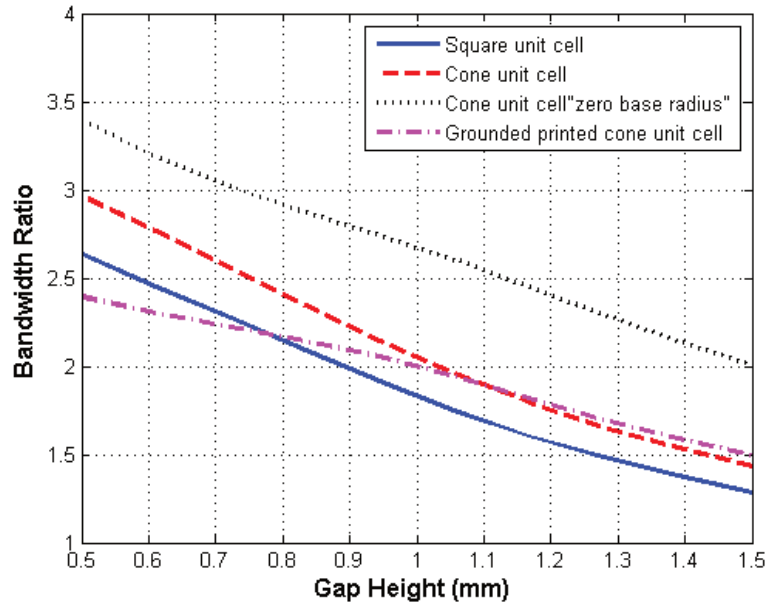


Figure 3.27: The relation between the bandwidth ratio and the gap height for four different cells in the presence of the ridge.

structure of the traditional RGW, where the gap height is the same above the ridge and the cells, and the dual gap height RGW, keeping a $50\ \Omega$ characteristic impedance of both structures. This figure illustrates that the ridge has to be of a smaller width than the nails of the cells for the gap heights around 0.5 mm or below. In this case the excitation of the ridge is difficult, and it is getting more difficult as the ridge width decreases. Another major advantage of the dual gap height RGW is its power handling capability relative to the traditional one in the case of small gap heights. The breakdown field of the air gap is 3 MV/m [49,50] and the more gap height above the ridge, the more field strength it can support. The relation between the gap height and the bandwidth ratio in the case of the dual gap height RGW is shown in Figure 3.29. It can be depicted from this figure that the grounded printed cone unit cell has a better performance than the traditional square cross-sectional unit cell for all values investigated for the gap height.

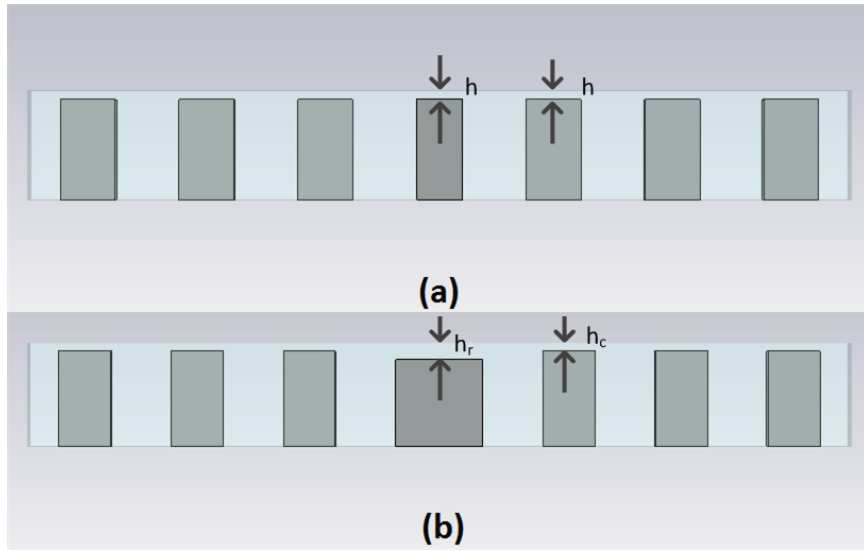


Figure 3.28: (a) Front view of the traditional RGW. (b) Front view of the dual gap height RGW.

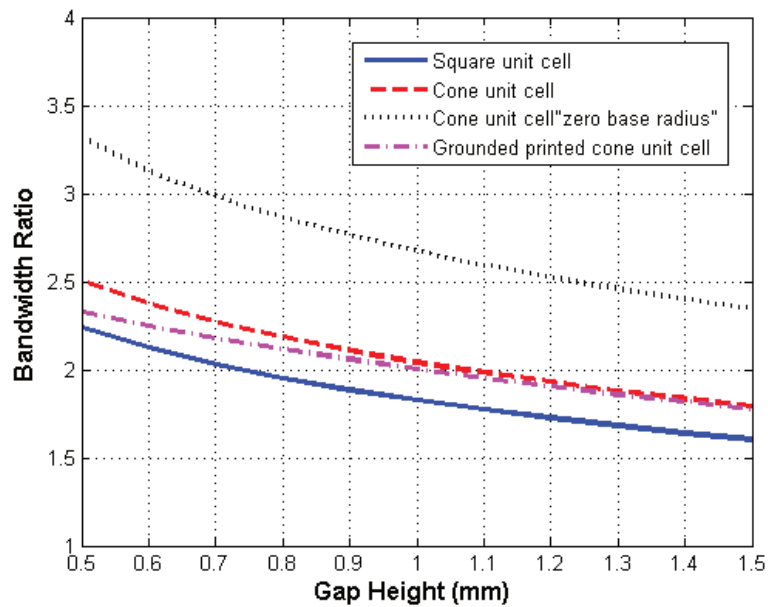


Figure 3.29: The relation between the bandwidth ratio and the gap height for four different cells in the dual gap height RGW.

3.2.2.2 Nail Connected RGW Configuration "Ridge Waveguide with Periodic Walls"

The traditional RGW has a single value for the gap height either above the ridge or the cells. Hence, this prevents the idea of the zero gap height RGW. However, the proposed idea of the dual " h " RGW makes it possible to investigate the zero gap height RGW above the nails. The gap cell height can be zero, while the ridge gap height can take another value as both values are independent. From another perspective, the proposed structure can be considered as a single ridge waveguide replacing the solid side walls by nails. The 3D structure of the proposed cell, the dispersion relation for the cell alone and the dispersion relation in the existence of the ridge are shown in Figure 3.30. It can be depicted from the dispersion relation of the cell that connecting the nails to the upper ground eliminates all modes before the band gap. In this case, the bandwidth ratio is infinite, but this is reduced in the presence of the ridge to be around 4:1. Here, the bandwidth limits are identified by the region in which there is only one linear mode that propagates. This is limited by the single ridge structure, which was studied before [21, 22]. The same methodology utilized in calculating the cutoff frequency of the single ridge waveguide can be applied with minor modifications. At the cutoff frequency, the signal will bounce in the transverse direction with no propagation in the longitudinal one. The transverse resonance conditions will be satisfied at infinite and zero impedance values at the middle point of the structure. The first resonance frequency, which corresponds to the cutoff frequency of the first mode, occurs when the middle point impedance tends to infinity. The structure in the transverse direction can be divided into three admittances in parallel. These three admittances are two transmission line sections and the discontinuity in between these two sections.

Mathematical formulation for the cutoff frequency

As illustrated in Figure 3.30 (a), the ridge width is denoted as W_r , while the gap height above the ridge is entitled h_r . Regarding the total width of the guiding structure between the two side walls W_t , an average value is considered, which is the distance between the middle of the adjacent pins on each side. Based on the shown cross section, the following phases will be defined

$$\theta_1 = 2\pi \frac{(W_t - W_r)/2}{\lambda'_c} \quad \theta_2 = 2\pi \frac{W_r/2}{\lambda'_c} \quad (3.15)$$

λ'_c is the cutoff wavelength in the presence of the ridge, which can be related to λ_c , the cutoff wavelength of the guide in the absences of the ridge, with the following equation

$$\lambda'_c = \left(\frac{\pi/2}{\theta_1 + \theta_2} \right) \lambda_c \quad (3.16)$$

This cutoff frequency is obtained through modeling the ridge as three parallel admittances. These admittances are an open circuited line, a short-circuited line, and the discontinuity. This discontinuity is denoted by B_0 and it is modeled in [22]. At the first resonance, the summation of the three admittances equals to zero

$$-Y_{01} \cot(\theta_1) + Y_{02} \tan(\theta_2) + B_0 = 0 \quad (3.17)$$

By simple manipulations, taking into consideration that the ratio between the two characteristic admittances of the two transmission line sections equals to the height ratio

$$\frac{(h_r + d_r)}{h_r} = \frac{\cot(\theta_1) - B_0/Y_{01}}{\tan(\theta_2)} \quad (3.18)$$

The discontinuity is modeled by a capacitor that takes the following expression [51, 52]

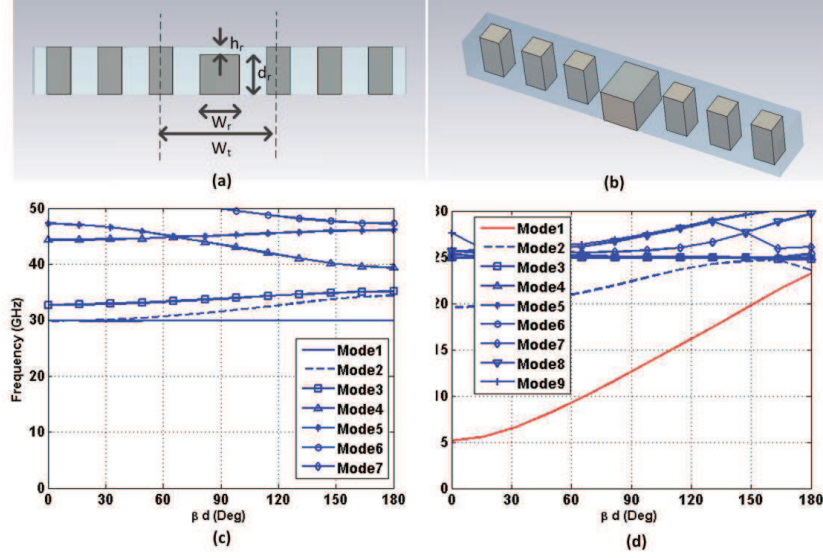


Figure 3.30: The zero gap height RGW (a) Front view. (b) 3D structure. (c) Unit cell dispersion relation. (d) The dispersion relation in the presence of the ridge.

$$C_d = \frac{2\varepsilon}{\pi} \ln \left(\sin \left(\frac{\pi}{2} \frac{d_r}{d_r + h_r} \right)^{-1} \right) \quad (3.19)$$

Substituting in Equation 3.18, the final transcendental equation is obtained as follows:

$$\begin{aligned}
& -\cot(\theta_1) + \frac{h_r + d_r}{h_r} \tan(\theta_2) \\
& + \frac{\theta_2}{\pi/4} \frac{h_r + d_r}{W_r} \ln \left(\left(\sin \left(\frac{\pi}{2} \frac{d_r}{d_r + h_r} \right) \right)^{-1} \right) = 0 \quad (3.20)
\end{aligned}$$

Solving the previous equation, the cutoff frequency of the proposed structure can be obtained. The proposed methodology is applied in the simulated example and the cutoff frequency of the nail connected RGW for the dimensions listed in Table 3.3 is calculated to be 5.27 GHz, while the simulation indicates a cutoff frequency of 5.2 GHz.

Table 3.3: The dimensions of the nail connected ridge gap waveguide.

The dimension	The value (mm)
W_r (The ridge width)	5 mm
d_r (The ridge height)	5 mm
h_r (The gap height above the ridge)	1 mm

3.2.3 Measurements Results

To test the performance of the proposed cells, a comparison is held between a straight line of a ridge surrounded by the square-cross sectional traditional cells and another ridge surrounded by these proposed printed cells. The interface of both lines is identical, and the same frequency range is used as well. This enables the utilization of the same excitation technique for both lines. A special coaxial to RGW transition is designed based on a five-section Chebyshev matching transformer to cover the band from 9 GHz to 25 GHz, which is wider than the bandwidth of both cells. Figure 3.31 shows the transition, which is tested to provide the transformation between 2.92 mm coaxial connector and the RGW interface for this wideband. This transition was described in detail in Chapter 2. It is quite important to mention that the proposed cells are printed on a substrate, and each row of cells is placed on a single piece to be installed in a groove adjacent to the ridge. Due to the assembly mechanism, grooves of 2 mm depth are made, and this results in increasing the pin length, which leads to a shift in the operating frequency band. As mentioned, the same operating frequency has to be utilized in order to make use of the available transition. To adjust the operating bandwidth by modifying the pin size, the pin height is reduced by increasing the printed ground height. The gap height above the cell, the cone width and the ground height are 0.5 mm, 4.95 mm and 1.5 mm respectively. These dimensions are selected to have the realized bandwidth within the frequency band through the available transition. Figure 3.32 illustrates the dispersion relation of the proposed cells with the modified dimensions. It can be seen from this figure that the proposed cells provide

a bandwidth ratio of 2.01 that ends at 18.7 GHz and starts at 9.3 GHz, while the traditional cell with a square cross-sectional pin provides a bandwidth ratio of 1.82, from 10.7 GHz to 19.5 GHz, as mentioned in Section 3.2.1. Performing a waveguide calibration to remove the transition effect in both measurements, the reference plane is shifted to be at the starting point of the RGW port. The fabricated two RGW straight lines are shown in Figure 3.33. The comparison between the measured and the simulated scattering parameters are shown in Figure 3.34 (a) in the case of the traditional square cross-sectional pin, while the same comparison in the case of the grounded printed cone unit cells is shown in Figure 3.34 (b). By visual comparison between the previous two figures, it is clear that the printed cone unit cell can provide a larger bandwidth than the traditional square cross-sectional pin cell. Another important note in these two figures is that the band in both cases extends beyond the expected end frequency. The bandwidth is expected to end at 19.5 GHz in the case of the traditional cell, and it is anticipated to end at 18.7 GHz in the case of the grounded printed cone cell. However, the bandwidth seems to cover beyond 20 GHz in both cases. In fact, the bandwidth is limited at the higher end by exciting higher order modes above the cells that carry part of the signal outside the ridge and introduce leakage. This may not occur in the case of a straight line of RGW, but it shows up when bending or discontinuities exist in the tested line.

3.3 Bandwidth evaluation of RGW components

In this chapter, the unit cell dispersion relation is validated experimentally. The bandwidths of different cell shapes are accurately evaluated. In addition, novel cell structures and novel types of the ridge gap waveguide are introduced. Based on the best performing transitions and the accurate estimation of the structure bandwidth, it is possible to start the design procedure of different ridge gap waveguide components.

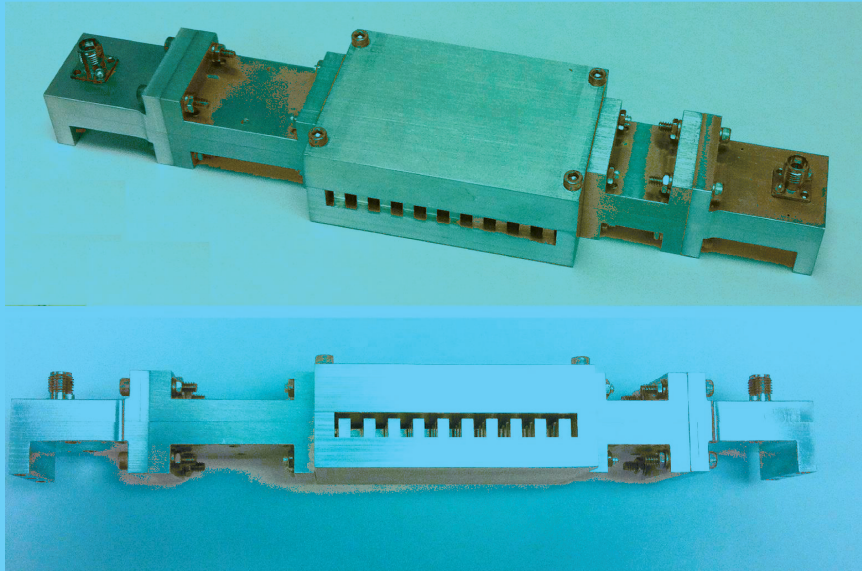


Figure 3.31: The fabricated transition between coaxial connector and RGW.

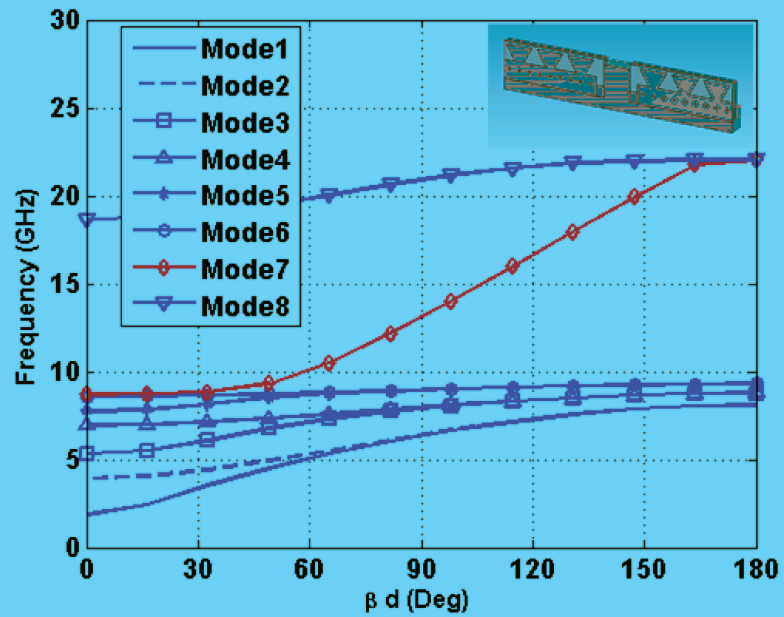


Figure 3.32: The dispersion relation of the grounded printed cone unit cell in the presence of the ridge.

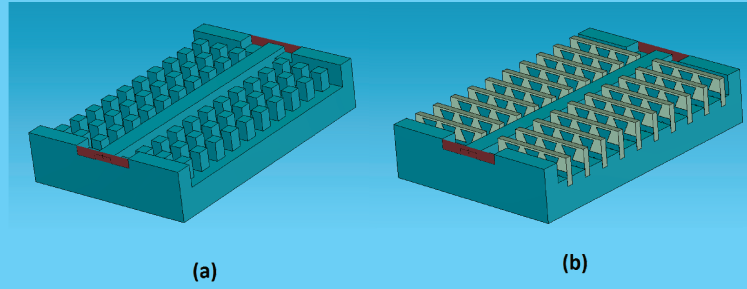
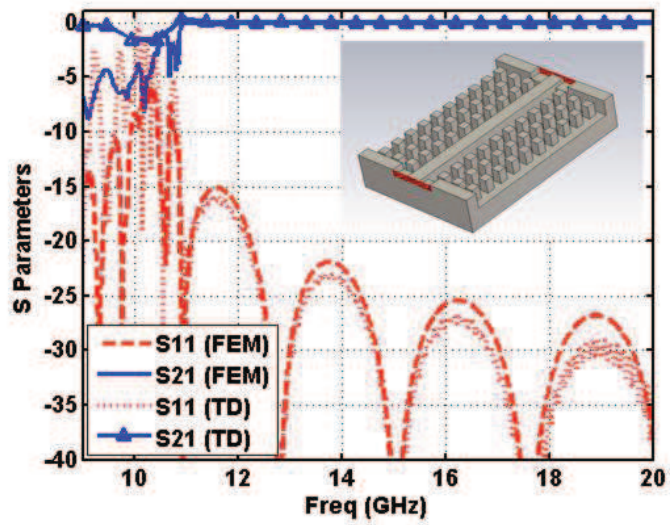
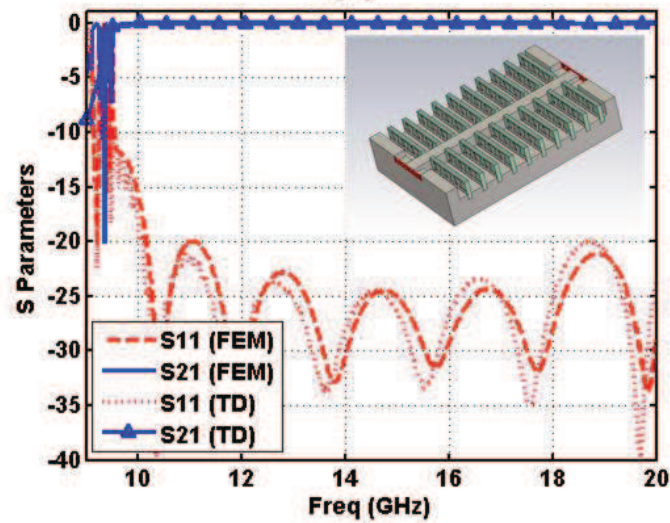


Figure 3.33: The fabricated straight RGW lines (a) The traditional square cross sectional unit cell. (b) The grounded printed cone unit cell.

In the following chapter, various reciprocal components will be introduced and in chapter 5, some nonreciprocal devices will be presented.



(a)



(b)

Figure 3.34: The scattering parameters of a straight line of a ridge gap waveguide (a) Surrounded by the square cross-sectional traditional cells. (b) Surrounded by grounded printed cone unit cells.

Chapter 4

Reciprocal Devices Based on RGW Technology

The previously proposed designs for RGW transitions removed the limitations of the excitation in RGW technology, which facilitates the development of wideband devices based on RGW technology. In this chapter, two reciprocal devices are to be proposed. The first device is a wideband power divider and the second one is a hybrid coupler based on an RGW. In both cases, the design procedures, as well as the results, are discussed in detail.

4.1 WideBand Power Divider Based on RGW

Ridge gap waveguides were deployed in many applications either in passive nonradiating devices such as filters [48] or antenna applications [23]. One of the commonly used types of passive devices is power dividers. They are used in antenna feeding structures to provide suitable excitations in the array antenna systems. Some trials were presented in the literature for power dividers based on RGW technology [45, 53]. However, these power dividers supported only less than 50 % of the possible bandwidth of the structure. The subsequent section presents the unit cell that surrounds

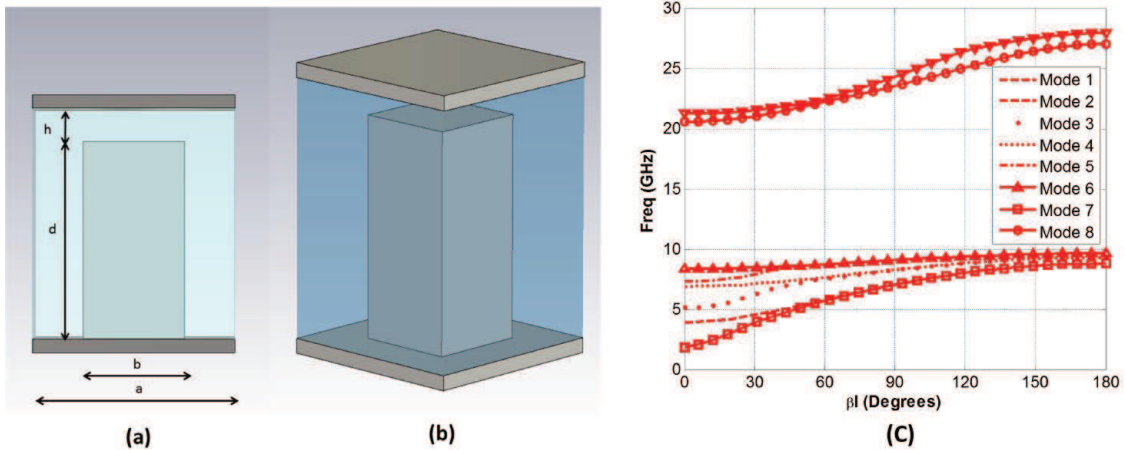


Figure 4.1: The AMC unit cell (a) Cross section view, (b) 3D view, and (c) Dispersion relation.

the RWG and the stopband of the periodic cells. The top surface of the periodic structure acts as a perfect magnetic conductor surface (PMC) that suppress wave propagation between the upper conductor surface and the PMC surface within the stopband. It should be clear that the device operating frequency band exists within the periodic cells stopband. Section 4.1.2 provides a description of the proposed power divider.

4.1.1 RWG Unit Cell Analysis

The unit cell is the traditional square cross-sectional nail. The structure in two views, as well as the dispersion relation, is shown in Figure 4.1 (a), (b) and (c), respectively. The existence of the ridge is considered in obtaining this dispersion relation. Figure 4.1 (c) shows that the stop band of the cell is from 10 GHz to 20.5 GHz, which is the conceivable bandwidth of the structure using this cell. The cell dimensions are given in Table 4.1.

Table 4.1: RGW unit cell dimension.

The Dimension	The value in (millimeter)
Cell size (a)	5
Nail width (b)	2.5
Nail height (d)	6
Gap height (h)	0.625

4.1.2 Power Divider Design

The power divider is designed based on a two matching level transformer. The input impedance of the parallel connection is half of the characteristic impedance of each single line. The starting value of the characteristic impedance can be obtained through the strip line equation, which give a good approximation [10].

$$Z_{0,RGW} = \frac{\eta}{2} \left[\frac{W}{2h} + 0.441 \right]^{-1} \quad (4.1)$$

This equation can be utilized to have a starting dimensions of the calculated matching transformers based on a Chebyshev polynomial. A triangular cut is placed on the connection between the two branches to provide better matching. Figure 4.2 (a) shows the top view. Figure 4.2 (b) for the 3D view and Figure 4.2 (c) for the divider with the microstrip transition and the coaxial terminator connectors, respectively. In all views, the upper ground is hidden to show the detailed structure. An optimization process is performed to obtain a better matching level for the required band, as the initial dimensions are calculated based on the rule of thumb assumption. The widths of both matching sections are 6.31 mm and 4.75 mm while the lengths are 6.61 mm and 4.71 mm. The triangular cut has a base dimension of 10.57 mm and a height of 3.59 mm. The ridge width is 3.58 mm. The response of the proposed power divider fed by the microstrip line to RGW transition is shown in Figure 4.3. The matching level of this design is better than -17 dB for 95 % of the possible band of the periodic cells. The possible bandwidth of the cells is obtained based on the assumption of infinite

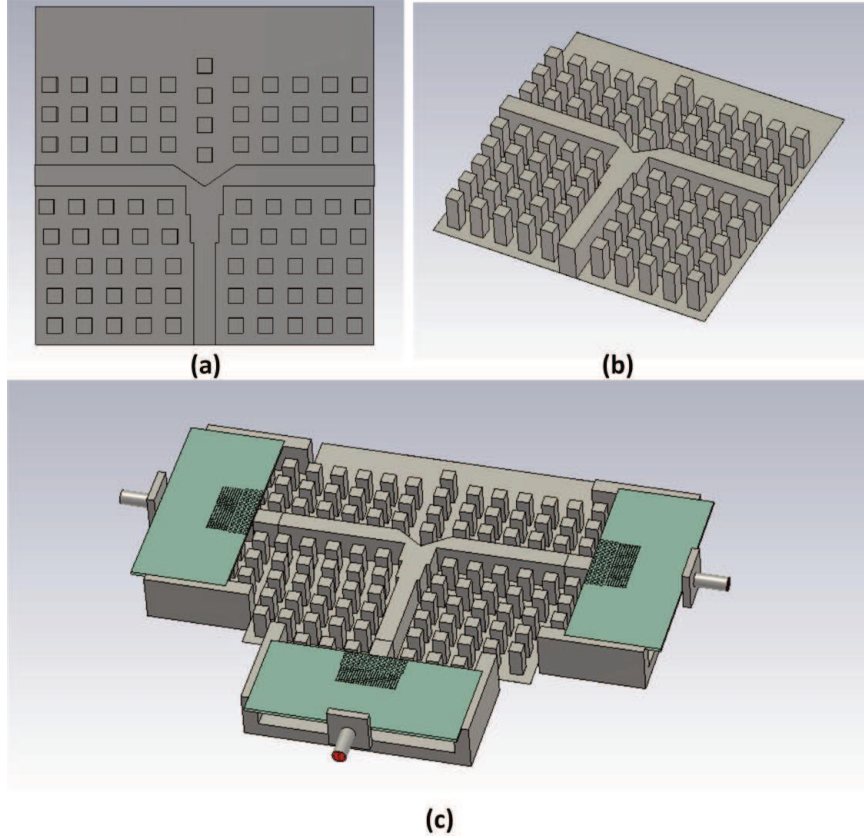


Figure 4.2: Power Divider configuration (a) Top view. (b) 3D structure (c) The configuration with the feeding structure.

periodicity. The finite periodicity of the cells results in shrinking the band a little bit to start at 10.3 GHz and ends at 20.3 GHz.

4.2 RGW 3-dB Hybrid Coupler

Hybrid microwave circuits were presented in the 1940s as a development of hybrid coils. The term hybrid was used to indicate the ensuring of the preferential isolation, which is the function of the hybrid coils in the old telephone systems [54]. This type of network is also called a bi-conjugate network, and it can be classified into hybrid rings, couplers, and hybrid junctions [55]. This terminology refers to the functionality of the device, where the input signal from a particular port is coupled to some ports and isolated from others. Through the previous seven decades, the microwave

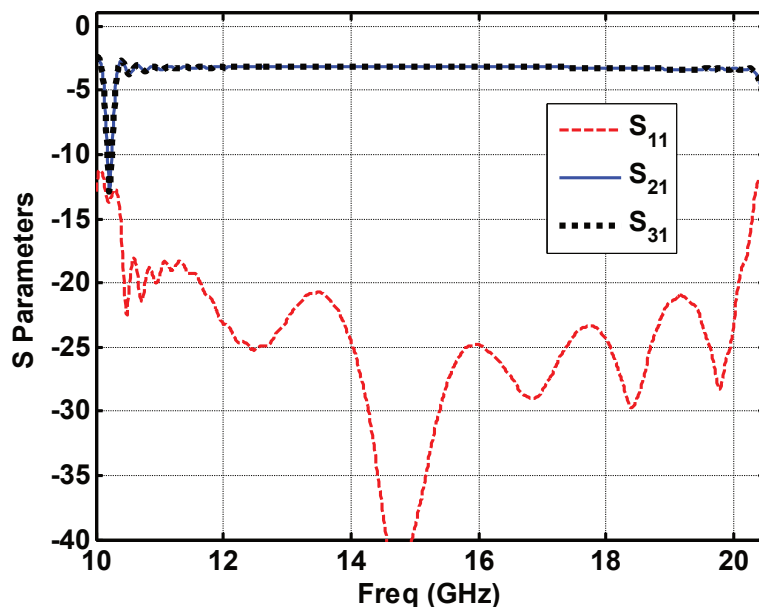


Figure 4.3: The scattering parameters of the power divider fed by the MSL to RGW transition.

industry paid considerable attention to couplers. The basic concepts, as well as the analysis of the couplers, were addressed in many publications for both the balanced and unbalanced couplers [56, 57]. The hybrid coupler was introduced with many configurations such as the coupled line and branch lines [58]. In addition, they were implemented by different guiding structures such as rectangular waveguides, stripline and microstrip lines [59]. The continuous development of the guiding structures to match the rapid changes in communication systems creates the need for similar developments in microwave components. Communication systems are moving toward the utilization of bands to provide high data rates suitable for high definition and virtual reality applications. The above 6 GHz bands, especially around 15 GHz, and the millimeter wave bands around 30 GHz and 60 GHz are the most recommended bands for the upcoming 5G mobile communication standard [60, 61].

The following part presents RGW hybrid coupler design centered at the 15 GHz for 5G communication systems and airborne radar applications. We start with an ideal

model assuming PMC surround the ridge. The PMC is realized by the periodic unit cells. The following section gives a mathematical formulation to obtain the coupling part dimensions. This is followed by the RGW hybrid coupler design procedure. Then a section explains the experimental validation of the final design.

4.2.1 Hybrid Coupler Mathematical Formulation & Empirical Design Equations

Starting with a similar analysis of the short slot rectangular hybrid coupler shown in Figure 4.4, the even-odd mode analysis is deployed. The relation between the scattering parameters of the structure and even-odd modes coefficients can be stated as follows [3]:

$$S_{11} = \frac{1}{2}(\Gamma_e + \Gamma_o) \quad (4.2)$$

$$S_{21} = \frac{1}{2}(T_e + T_o) \quad (4.3)$$

$$S_{31} = \frac{1}{2}(T_e - T_o) \quad (4.4)$$

$$S_{41} = \frac{1}{2}(\Gamma_e - \Gamma_o) \quad (4.5)$$

where Γ_e and Γ_o represent the reflection coefficients for the even and odd modes, respectively, while T_e and T_o are the transmission coefficients for the even and odd modes, respectively. The odd mode is not affected almost by the existence of the short slot. The first condition is to satisfy the isolation between the input and the isolated ports. For a complete isolation, the reflection coefficient of both modes should be equal to zero. This puts a limitation on the width reduction inside the coupling part. In the even mode, ϕ_r represents a phase shift at the end of the coupling sections. The solution of Maxwell equations for the even mode is studied in detail by Carlson and

Heins [62]. The second condition is satisfied if the total coupling section length gives a phase shift of $\pi/2$. This can be mathematically described by the following formula:

$$(\beta^e - \beta^o) L + \phi_r = \pi/2 \quad (4.6)$$

Through this condition, the coupling area length can be obtained. Moreover, the reflection and transmission coefficients can be evaluated [56]. Applying the previous procedure on different waveguide standards, The length of the coupling section (in inches) can be obtained approximately by the following empirical expression

$$L = a_1 \lambda_g^{b_1} \quad (4.7)$$

where $a_1 = 1.701$, $b_1 = 1.072$ and the guided wavelength is in inches. This is quite simple and a good approximation, which can be considered as a starting point of the coupling section length. The initial diameter of the capacitive domes is $\phi_d = 0.4L$ with a height of $h_d = 0.05\phi_d$, while the coupling section width is 5% less than the total width of the opening. The previous approximation initially can satisfy a good matching and isolation levels. However, to ensure a balanced output, the middle section width, and capacitive domes are used as tuning elements. To increase the power directed to port 3 the middle section width should be decreased, or the dome diameter should be increased and vice versa. The previous approximations are tested on variety range of rectangular waveguides from S-band to Ka-band. Many examples can be shown to validate the previous empirical equation. However, the major goal of this work is the RGW hybrid coupler design. The dimensions obtained through these expressions are considered as initial values for the ideal RGW coupler.

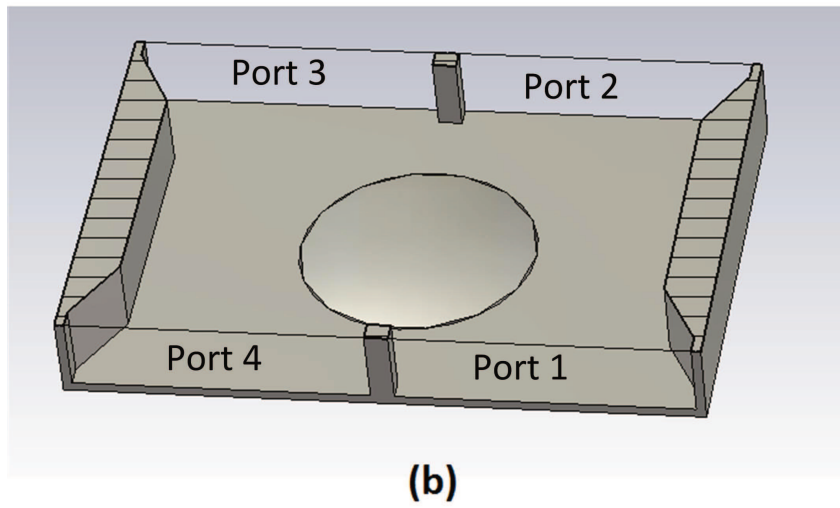
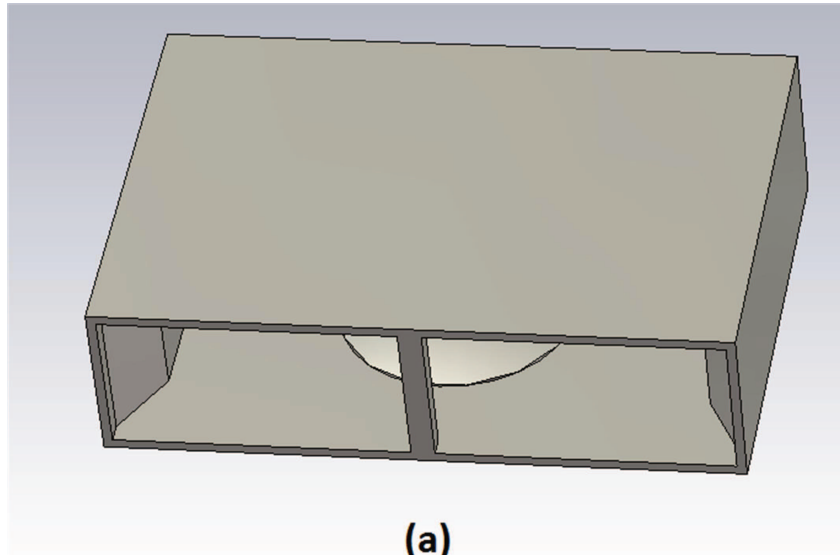


Figure 4.4: The short slot rectangular waveguide hybrid coupler (a) 3D view (b) 3D sectional view.

4.2.2 RGW Hybrid Coupler Design Procedure

4.2.2.1 The Ideal Model with PMC Surface

The previously mentioned empirical expressions are used to obtain the initial dimensions of the coupling section at the design frequency for the rectangular waveguide. The electric field vanishes at both sides in the case of the rectangular waveguide, while in the case of the RGW, the electric field is maximum at both ridge sides. This can be compensated in the previous equations by multiplying by half. The previous empirical equation is modified for the RGW to be:

$$L = \frac{1}{2}a_1 \lambda_g^{b_1} \quad (4.8)$$

where $\lambda_g = \lambda_0 = c/f_d$, the guided wavelength is equal to the free space wavelength because the propagating mode is a Quasi-TEM mode, while c represents the speed of light and f_d represents the design frequency. The same constants in this empirical equation are used $a_1 = 1.701$ and $b_1 = 1.072$. The diameter of the dome and its height can be expressed as:

$$\phi_d = 0.4L \quad (4.9)$$

$$h_d = 0.05\phi_d \quad (4.10)$$

In the rectangular waveguide, the coupling area width is selected based on the standard width of the guide, while in the RGW case, the coupling section is selected initially as a square shape, then the width is varied to achieve the power balance between Ports 2 and 3. The previous expressions are used to get initial design values of the coupler configuration in Figure 4.5 (a). In this figure, the upper ground is removed to show the structure details. The simulation is performed while a PMC

Table 4.2: The dimensions of the RGW hybrid coupler with ideal PMC boundaries.

Dimension	Value in (mm)
Coupling area length L	13.21
Coupling area width W	13.97
Dome diameter ϕ_d	7.9
Dome height h_d	0.2
Ridge width W_r	5
Gap height h_g	1

ideal boundary condition is surrounding the ridge. Hence, an optimization process is carried out to reach the values listed in Table 4.2. The ridge width is $W_r = 5$ mm and the gap height $h_g = 1$ mm. These values are selected to match the available transition in the lab for RGW. It can be designed with some suitable values for the required frequency band. The simulated scattering parameters are shown in Figure 4.5 (b), where the response is considered only in 20% bandwidth centered at the design frequency. The four arms are separated in order to place the pins required for isolation in between the four ports.

4.2.2.2 The Realized Structures with Periodic Cells

The final step in the design is to replace the PMC ideal boundary with periodic cells. The cell design was addressed in many papers before to achieve a particular bandwidth. The traditional bed of nail unit cell configuration can achieve a bandwidth ratio of 2:1 and many articles addressed different techniques to achieve a wider bandwidth. In this case specifically, there is no need to have a complicated cell design as the objective operating bandwidth ratio is less than 2:1. The gap height is $h_g = 1$ mm, as mentioned before, to match the available transition. Using the Eigenmode solver, the proposed cell in Figure 4.6 (a) and (b) can be simulated to obtain the response in Figure 4.6 (c), where the dimensions are listed in Table 4.3. It can be depicted from this figure that the stop band of the periodic cells starts after 11 GHz and ends at 25 GHz, which covers the required bandwidth of the RGW hybrid coupler. The periodic

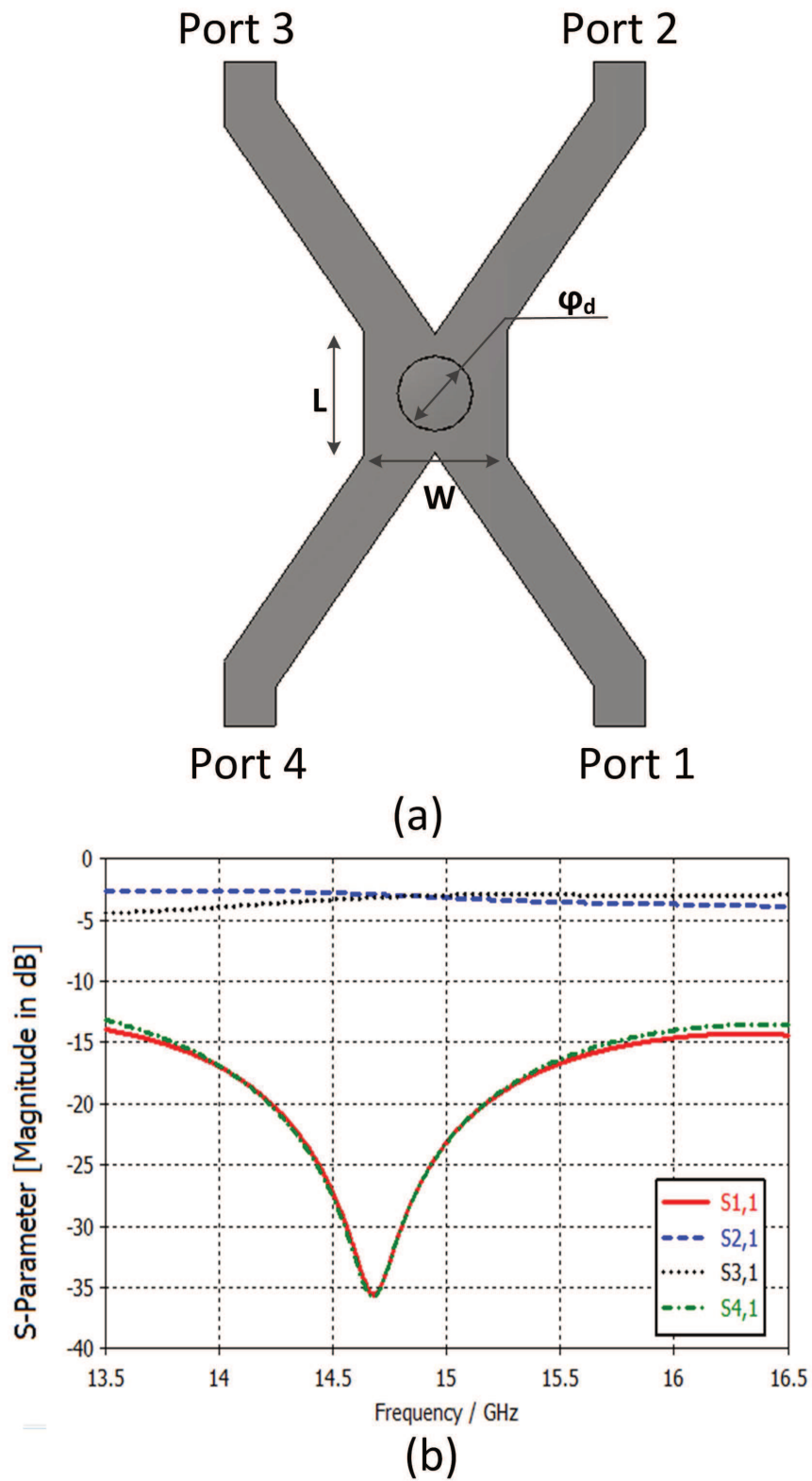


Figure 4.5: The RGW hybrid coupler with ideal boundary conditions (a) Structure top view. (b) Simulated scattering parameters.

Table 4.3: The dimensions of the unit cell.

Variable	Value in (mm)
Cell size a	4.4
Nail width b	2
Nail height d	4.7
Gap height h	1

cells are placed around the ridge, where at least two rows should be covering the ridge in all directions. The final simulated configuration is shown in Figure 4.7 (a), while the simulated response is shown in Figure 4.7 (b). The ports are converted to a single ridge structure with a particular dimension to match the available transition. It can be depicted from the simulated results that the realized coupler covers approximately the band from 14 GHz to 16.5 GHz. This can be considered as 16.6% bandwidth with a matching level of -14 dB.

4.2.3 The Experimental Validation

To test the RGW hybrid coupler, a complete measurement setup is designed. The testing setup contains the following items: Two coaxial to custom single ridge transitions with matching level below -18 dB for the double transition, two matched loads, and a custom through for the calibration process.

The components used in the measurement setup are shown in Figure 4.8. The first part of the measurement setup is coaxial to a single ridge transition. The coaxial interface used is the 2.92 mm standard connector. The design of this adapter is performed based on two parts. The first part is a five-section Chebyshev matching transformer from coaxial to the single ridge with a particular size. The second part is a fitting section from a single ridge to a single ridge with different dimensions. The details of the design and the testing of this transition are presented in previous chapters, where the final design can cover the whole band 10-25 GHz. The matching level of the double transition is -18 dB. Figure 4.9(a) shows the adapter used in the

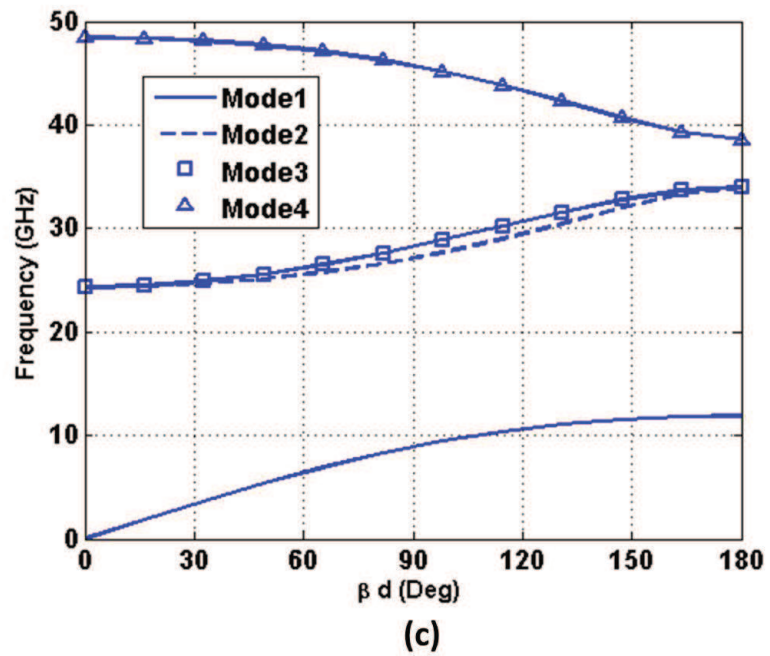
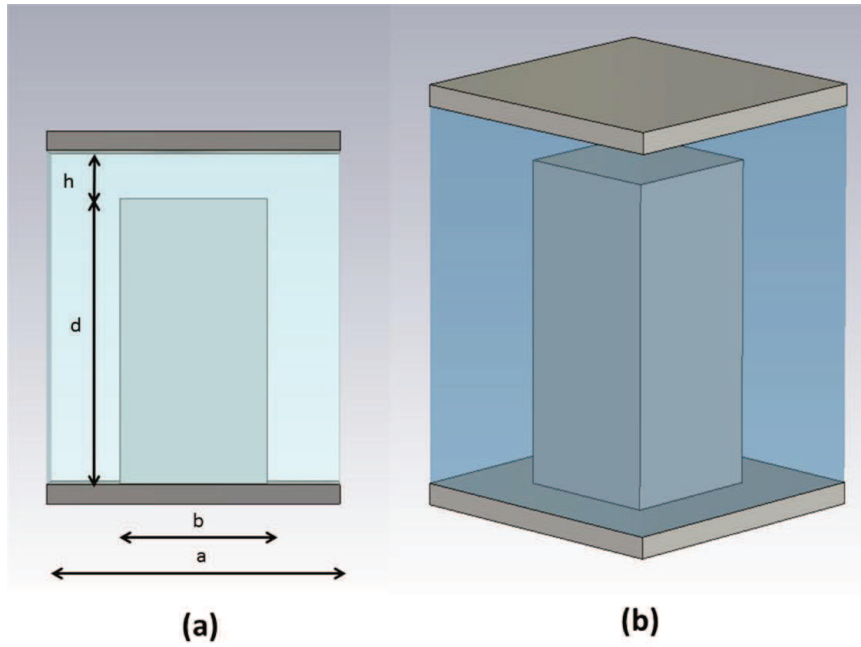
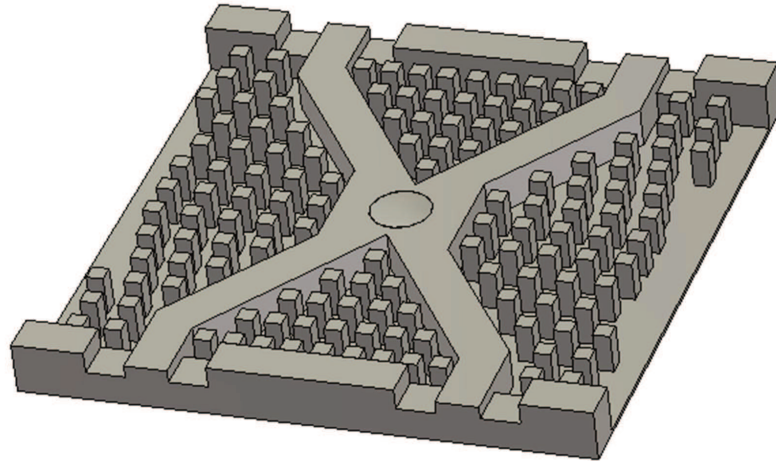
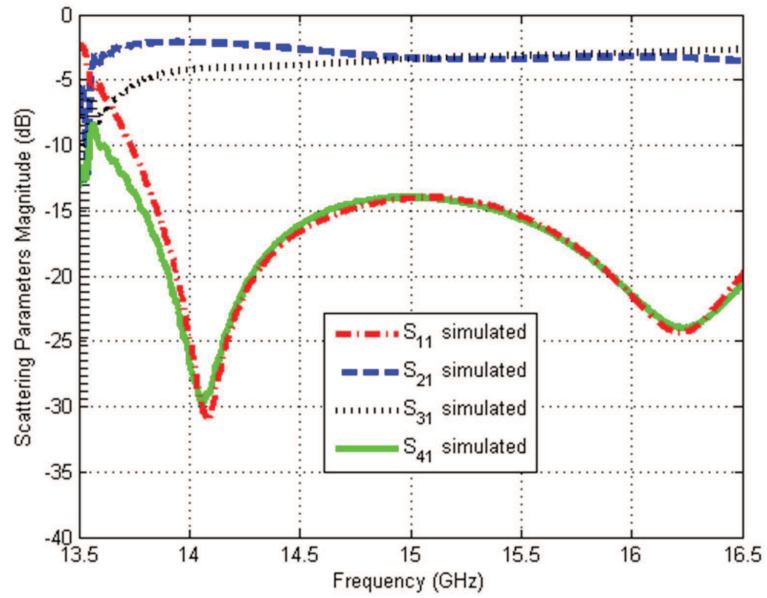


Figure 4.6: The unit cell (a) Front view. (b) 3D structure (c) Dispersion relation.



(a)



(b)

Figure 4.7: The simulated RGW hybrid coupler (a)3D model upper ground is removed (b) Scattering parameters.

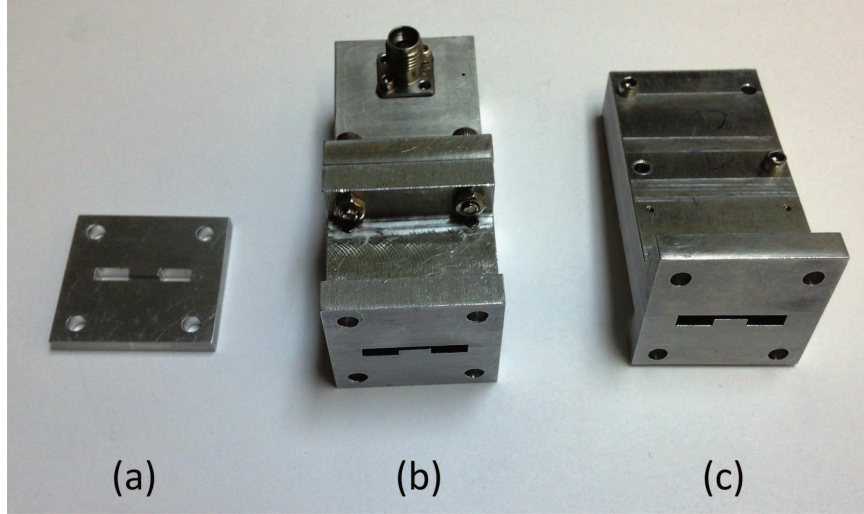
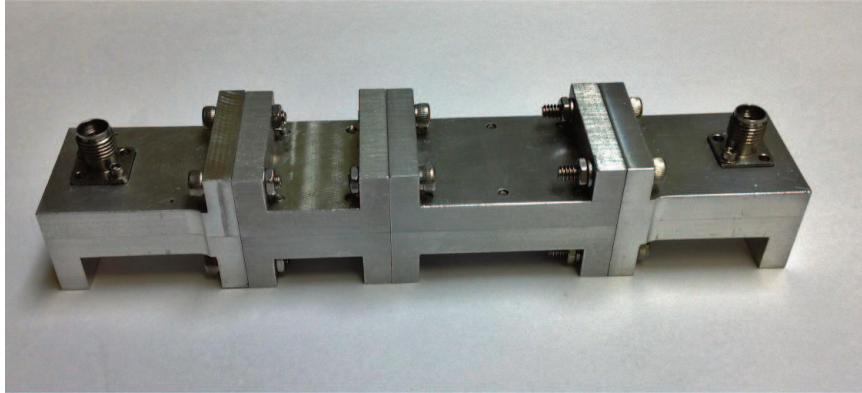


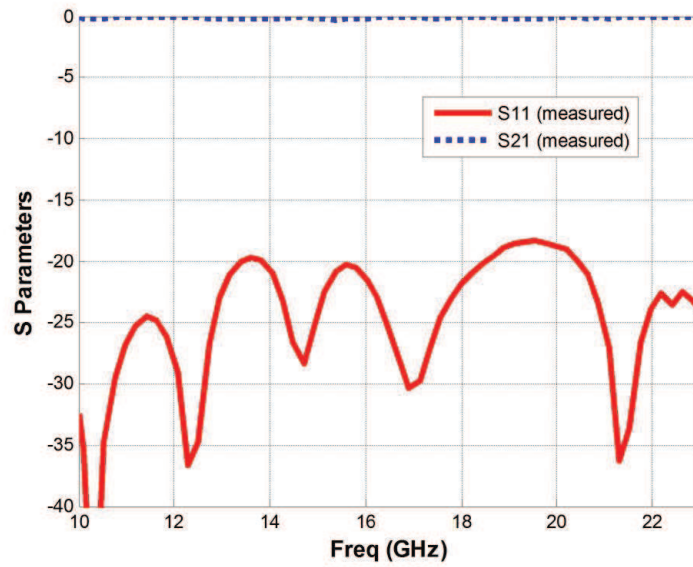
Figure 4.8: The measurement setup components (a) The custom through. (b) Coax to single ridge transition. (c) Single ridge matched load.

testing, while Figure 4.9 (b) show the response of the double transition. Regarding the matched loads, they are designed based on placing a wedge shaped lossy material inside a tapered single ridge section. The lossy material used in this structure is Raisen material with a dielectric constant of $\epsilon_r = 12.6$ and a loss tangent $\tan \delta = 0.76$.

The ANRITSU MS46322A VNA is used in the measurement. The first measurement was performed through a coaxial calibration, where the two transitions back to back is evaluated as discussed before. Hence, the two matched loads were measured with the same coaxial calibration. The measurement configuration is shown in Figure 4.10 (a), and the response is provided in Figure 4.10 (b). It is important to note that the previous curve represents the combined response of the transition and the load. Finally, the fabricated RGW hybrid coupler was tested as shown in Figure 4.11 (a). The calibration methodology utilized is the 2-port double offset short calibration technique. This transfers the reference plane at the waveguide port of both adapters. The final response is shown in Figure 4.11 (b), where the comparison between the measurement and the simulation is presented. It can be depicted from this figure that both curves are in very good agreement.

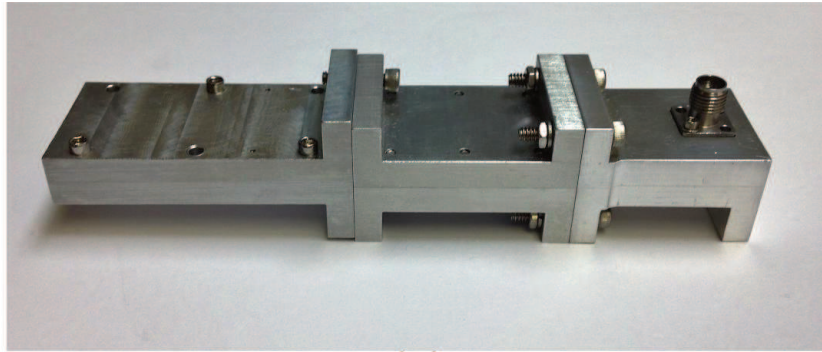


(a)

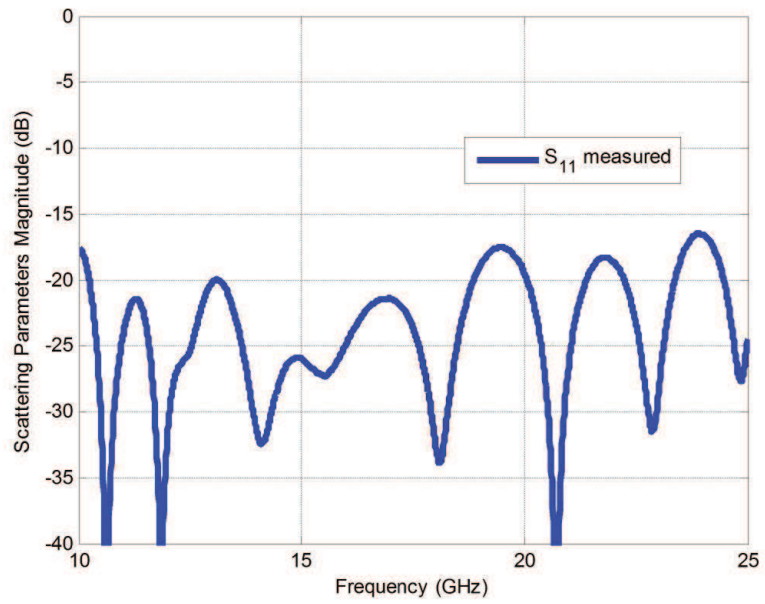


(b)

Figure 4.9: The Coaxial to RGW transition (a) Connected back to back (b) Back to back measured scattering parameters.

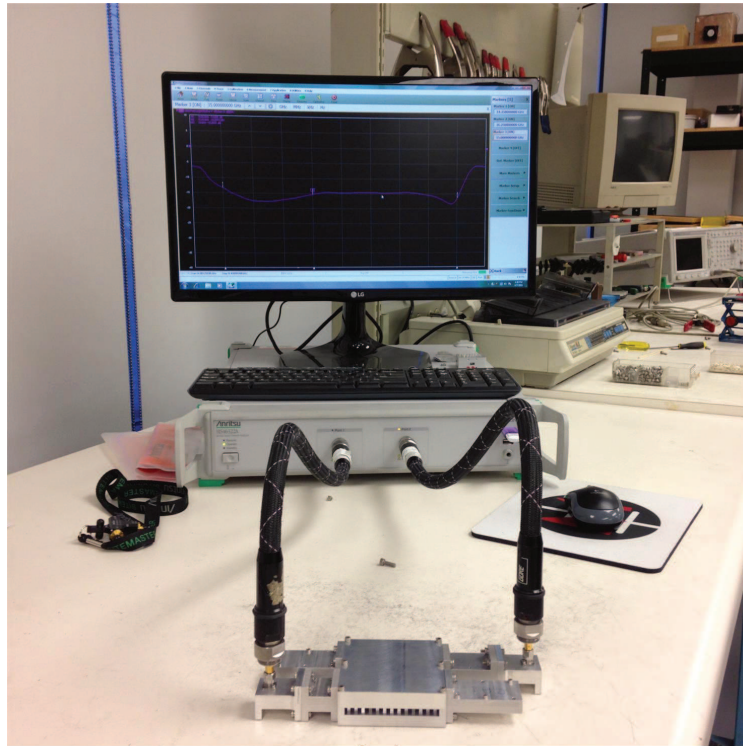


(a)

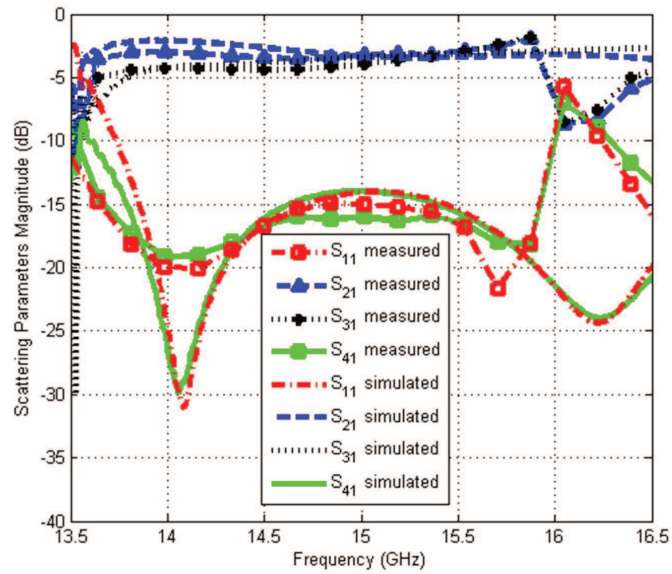


(b)

Figure 4.10: The matched load evaluation (a) Measurement setup. (b) Scattering parameters.



(a)



(b)

Figure 4.11: The final RGW hybrid coupler (a) measurement setup (b) comparison of the simulated response.

4.3 RGW Passive Components Summary

In this chapter, two different devices are presented. Both devices are reciprocal components. All elements deployed in the design are linear elements. In the following chapter, the RGW circulators design methodology will be explained. The core element in the design is the ferrite disc. This disc has an anisotropic behavior for the permeability tensor, where the reciprocity condition is violated.

Chapter 5

Non-Reciprocal Devices Based on RGW Technology

5.1 Introduction

Microwave circulators have been considered essential components in radar systems for more than six decades [63,64]. The first type of circulator was based on Faraday rotation. Other types of circulators were introduced for better power handling such as resonance circulators and differential phase shift circulators [65–67]. The basic concepts of ferrite materials physics were revisited many times to provide a solid background for circulators analysis and design [68]. Among these types of circulators, the junction circulators are paramount configurations. They are called turnstile circulators [69,70], Y circulators [71,72] and junction circulators [73]. The configuration of this type consists of three identical guiding structures connected in a Y-shape while a ferrite disc is placed in the middle of the structure to provide the nonreciprocal behavior. The three identical arms can be a rectangular waveguide, stripline, microstrip-line or any guiding structure [74–76]. Some other designs were introduced to utilize lumped elements for matching the junction circulators [77,78].

Over the past few decades, circulators were developed to achieve better electrical specifications with a compact size and low cost [79,80]. Also, many publications addressed the junction analysis either by constructing a model [81–83] or by the development of a suitable numerical technique [84–86]. Modern guiding structures are deployed for circulators implementations such as the SIW and the coupled line circulators [87–89]. Moreover, modern technologies were utilized to introduce semiconductors and MMICs circulators [90,91].

The objective of the present work is providing a systematic approach to design circulators with closed form expressions that reveal the hidden information regarding the circulator design. The provided expressions are valid for a wide range of parameters. It is also shown that the current expressions can be used for any frequency band with proper scaling. In addition, this work presents the first design for a circulator based on the RGW technology. The targeted circulators are centered at 15 GHz and 30 GHz, for 5G mobile applications. The frequency direction for the 5G technology is above 6 GHz and mainly deploys the millimeter wave frequency range [60,61]. The 15 GHz band can be used for the airborne radar applications, as well. The present work is a part of a project to design microwave components based on RGW technology. The following section explains, in detail, the mathematical formulations used for the junction circulator analysis. This is followed by a description of the design procedure. The design method is divided into two major steps. The first step is to consider the surface of the pins as an ideal perfect magnetic conductor (PMC) boundary. In the second step, the PMC is replaced by the actual structure.

5.2 Junction Circulator Mathematical Formulations

5.2.1 The Ferrite Disc Field Distribution

Starting from Maxwell equations that can be listed as:

$$\nabla \times \bar{E} = -j\omega\bar{B} \quad (5.1)$$

$$\nabla \times \bar{H} = j\omega\bar{D} \quad (5.2)$$

where, a tensor represents the permeability of the ferrite material

$$\bar{B} = [\mu] \bar{H} \quad (5.3)$$

for a ferrite disc saturated in the \hat{z} direction, this tensor is expressed, in the cylindrical coordinates, by [3]

$$[\mu] = \begin{bmatrix} \mu & j\kappa & 0 \\ -j\kappa & \mu & 0 \\ 0 & 0 & \mu_0 \end{bmatrix} \quad (5.4)$$

The expressions for μ and κ are summarized in Table 5.1. Then the previous equations can be rewritten as

$$\nabla \times \bar{E} = -j\omega [\mu] \bar{H} \quad (5.5)$$

$$\nabla \times \bar{H} = j\omega\epsilon\bar{E} \quad (5.6)$$

Based on the assumption of no axial variation, the solution of Maxwell equations in the cylindrical coordinates, taking into consideration this permeability tensor is listed below:

$$\frac{1}{\rho} \frac{\partial E_z}{\partial \phi} = -j\omega (\mu H_\rho + j\kappa H_\phi) \quad (5.7)$$

$$-\frac{\partial E_z}{\partial \rho} = -j\omega (-j\kappa H_\rho + \mu H_\phi) \quad (5.8)$$

Solving both together:

$$H_\rho = \frac{jY_{0eff}}{k_{eff}\mu} \left(j\kappa \frac{\partial E_z}{\partial \rho} + \frac{\mu}{\rho} \frac{\partial E_z}{\partial \phi} \right) \quad (5.9)$$

$$H_\phi = \frac{-jY_{0eff}}{k_{eff}\mu} \left(\mu \frac{\partial E_z}{\partial \rho} + \frac{-j\kappa}{\rho} \frac{\partial E_z}{\partial \phi} \right) \quad (5.10)$$

where the effective wavenumber, the effective intrinsic admittance, and the effective permeability are listed in Table 5.1. Solving Equation 5.6, one more relation can be obtained as follows:

$$\frac{1}{\rho} \left[\frac{\partial (\rho H_\phi)}{\partial \rho} - \frac{\partial H_\rho}{\partial \phi} \right] = j\omega \varepsilon E_z \quad (5.11)$$

By direct manipulation a second order differential equation for the axial electric field can be expressed as:

$$\rho^2 \frac{\partial^2 E_z}{\partial \rho^2} + \rho \frac{\partial E_z}{\partial \rho} + \rho^2 k_{eff}^2 E_z + \frac{\partial^2 E_z}{\partial \phi^2} = 0 \quad (5.12)$$

The solution of the previous equation is commonly addressed in cylindrical waveguide problems, and it takes the form of:

$$E_z = \sum_{n=-\infty}^{\infty} A_n J_n(k_{eff}\rho) e^{jn\phi} + C_n N_n(k_{eff}\rho) e^{jn\phi} \quad (5.13)$$

Where $J_n(k_{eff}\rho)$ and $N_n(k_{eff}\rho)$ are the Bessel and Neumann functions of order n , respectively. $N_n(k_{eff}\rho)$ goes to ∞ at the axis of the cylinder, which leads to having $C_n = 0$. Substituting in Equation 5.10, the magnetic field H_ϕ takes the following form:

$$H_\phi = -jY_{eff} \sum_{n=-\infty}^{\infty} A_n \left[J'_n(k_{eff}\rho) + \frac{n g_\kappa}{k_{eff}\rho} J_n(k_{eff}\rho) \right] \quad (5.14)$$

The electric field can be expressed as:

$$E_z = \sum_{n=-\infty}^{\infty} A_n J_n(k_{eff}\rho) e^{jn\phi} \quad (5.15)$$

Figure 5.1 illustrates a schematic of the circulator, with the coordinates indicated. The port width W is related to the coupling area at each port. This area is controlled by the coupling angle ψ , where

$$\sin(\psi) = \frac{W}{2a} \quad (5.16)$$

In any 3-port circulator, it is required to couple all the input power from port 1 to port 2, while port 3 is isolated. The isolation condition of the circulator means that no power is coupled to Port 3, which is only possible if the field distribution vanishes at $\phi = \phi_{P3} = 240^\circ$. The required field distribution to satisfy the circulator conditions can be stated mathematically by:

$$H_{\phi, required}(a, \phi) = \begin{cases} H_0 & -\psi < \phi < \psi \\ H_0 & 2\pi/3 - \psi < \phi < 2\pi/3 + \psi \\ 0 & 4\pi/3 - \psi < \phi < 4\pi/3 + \psi \\ 0 & O.w. \end{cases} \quad (5.17)$$

The above boundary conditions are required to ensure the existence of the magnetic field at Port 1 and Port 2. On the other hand, there is no magnetic field at Port 3

and no magnetic field in between ports. The last assumption is based on assuming a PMC boundary on the disc surface due to the high permittivity of the ferrite disc with respect to the surrounding permittivity. To apply the circulatory boundary condition of the magnetic field, Equation 5.17 has to be written in the Fourier series form as

$$H_{\phi, required}(a, \phi) = \frac{\psi \sin(n\psi)}{\pi n\psi} \sum_n [(1 + e^{-j2\pi n/3}) e^{jn\phi}] \quad (5.18)$$

This ideal field boundary condition can be satisfied through equating the magnetic field inside the ferrite disc with the required tangential magnetic field outside. This amplitude A_n can be expressed as:

$$A_n = j \frac{1}{Y_{0eff}} \frac{\sin(n\psi)}{n} \left[\frac{1 + e^{j2\pi n/3}}{J'_n(x) + \frac{ng_\kappa}{x} J_n(x)} \right] \quad (5.19)$$

The electric field at the port is the average field over the interval ψ , with the following expression:

$$E_{zp} = \frac{1}{2\psi} \int_{\phi_p - \psi}^{\phi_p + \psi} E_z d\phi \Big|_{\rho=a} \quad (5.20)$$

where $\phi_p = 0, 120^\circ$ or 240° for ports 1, 2 and 3, respectively. Performing the integral, the average electric field at the port is

$$E_{zp} = \sum j \eta_{effr} \cdot \eta_0 \left(\frac{\sin(n\psi)}{n\psi} \right)^2 \left[\frac{(1 + e^{-j\frac{2\pi n}{3}}) e^{jn\phi_p}}{J'_n(x)/J_n(x) + \frac{ng_\kappa}{x}} \right] \quad (5.21)$$

5.2.2 The Junction Network Representations

Although the junction circulator is an n-port network, the 3-port network is the commonly used configuration. At Port 1, the magnetic field can be expressed as:

$$H_{\phi p1} = 1 \quad (5.22)$$

Table 5.1: Permeability tensor important expressions

The Physical Quantity	Symbol	Expression
Gyropy (g_κ)	κ/μ	$\frac{\omega\omega_m}{\omega_0^2-\omega^2+\omega_0\omega_m}$
Diagonal elements	μ	$\mu_0(1+\psi_{xx}) = \mu_0(1+\psi_{yy})$
Off diag. elements	κ	$-j\mu_0\psi_{xy} = j\mu_0\psi_{yx}$
Diagonal susceptibility	ψ_{xx}	$\frac{\omega_0\omega_m}{\omega_0^2-\omega^2}$
Off diag. susceptibility	ψ_{xy}	$\frac{j\omega\omega_m}{\omega_0^2-\omega^2}$
Larmor angular freq.	ω_0	$\mu_0\gamma$ " H_0 (A/m) "
Magnetic angular freq.	ω_m	$\mu_0\gamma$ " M_s (A/m) "
Normalized Larmor freq.	σ_0	$\frac{\omega_0}{\omega} = \frac{2.8*10^6}{f}$ " $H_0(Oe)$ "
Normalized magnetic freq.	p_m	$\frac{\omega_m}{\omega} = \frac{2.8*10^6}{f}$ " $(4\pi M_s)(G)$ "

The magnetic field expression, in the previous equation, is manipulated via the integration

$$H_{\phi p} = \frac{1}{2\psi} \int_{\phi_p-\psi}^{\phi_p+\psi} H_\phi d\phi \Big|_{\rho=a} \quad (5.23)$$

Both fields can be related to each other by the following matrix

$$\begin{bmatrix} E_{zp1} \\ E_{zp2} \\ E_{zp3} \end{bmatrix} = \begin{bmatrix} \eta_{11} & \eta_{12} & \eta_{13} \\ \eta_{21} & \eta_{22} & \eta_{23} \\ \eta_{31} & \eta_{32} & \eta_{33} \end{bmatrix} \begin{bmatrix} H_{\phi p1} \\ H_{\phi p2} \\ H_{\phi p3} \end{bmatrix} \quad (5.24)$$

Taking the symmetry and the circulator operation into account, the following equations can be stated

$$\eta_{11} = \eta_{22} = \eta_{33} \quad (5.25)$$

$$\eta_{12} = \eta_{31} = \eta_{23} \quad (5.26)$$

$$\eta_{13} = \eta_{21} = \eta_{32} \quad (5.27)$$

The number of unknowns is reduced to:

$$\begin{bmatrix} E_{zp1} \\ E_{zp2} \\ E_{zp3} \end{bmatrix} = \begin{bmatrix} \eta_{11} & \eta_{12} & \eta_{13} \\ \eta_{13} & \eta_{11} & \eta_{12} \\ \eta_{12} & \eta_{13} & \eta_{11} \end{bmatrix} \begin{bmatrix} H_{\phi p1} \\ H_{\phi p2} \\ H_{\phi p3} \end{bmatrix} \quad (5.28)$$

where

$$\eta_{11} = \sum \left[j \frac{\psi}{\pi} \left(\frac{\sin(n\psi)}{n\psi} \right)^2 \frac{\eta_{eff} \cdot \eta_0}{J'_n(x)/J_n(x) + \frac{n g_\kappa}{x}} \right] \quad (5.29)$$

$$\eta_{12} = \sum \left[j \frac{\psi}{\pi} \left(\frac{\sin(n\psi)}{n\psi} \right)^2 \frac{\eta_{eff} \cdot \eta_0 e^{j2n\pi/3}}{J'_n(x)/J_n(x) + \frac{n g_\kappa}{x}} \right] \quad (5.30)$$

$$\eta_{13} = \sum \left[j \frac{\psi}{\pi} \left(\frac{\sin(n\psi)}{n\psi} \right)^2 \frac{\eta_{eff} \cdot \eta_0 e^{j4n\pi/3}}{J'_n(x)/J_n(x) + \frac{n g_\kappa}{x}} \right] \quad (5.31)$$

In the case of total isolation, $E_{zp3} = 0$ and $H_{\phi p3} = 0$, simultaneously. The input impedance of the junction can be written as:

$$Z_{in} = \frac{Z_0}{\eta_0} (\eta_{11} - \eta_{12}^2/\eta_{13}) \quad (5.32)$$

where Z_0 and η_0 are the characteristic impedance of the input transmission line and the intrinsic impedance, respectively. This equation can be reduced at the resonance by forcing $\eta_{12} = -\eta_{13}$. The final input impedance can be expressed as:

$$Z_{in} = \frac{Z_0}{\eta_0} (\eta_{11} + \eta_{12}) \quad (5.33)$$

For the maximum coupling between the input and the output ports, the resonance condition should be satisfied. To achieve that the input reactance of the junction must be equal to zero. This condition can be mathematically described as follows:

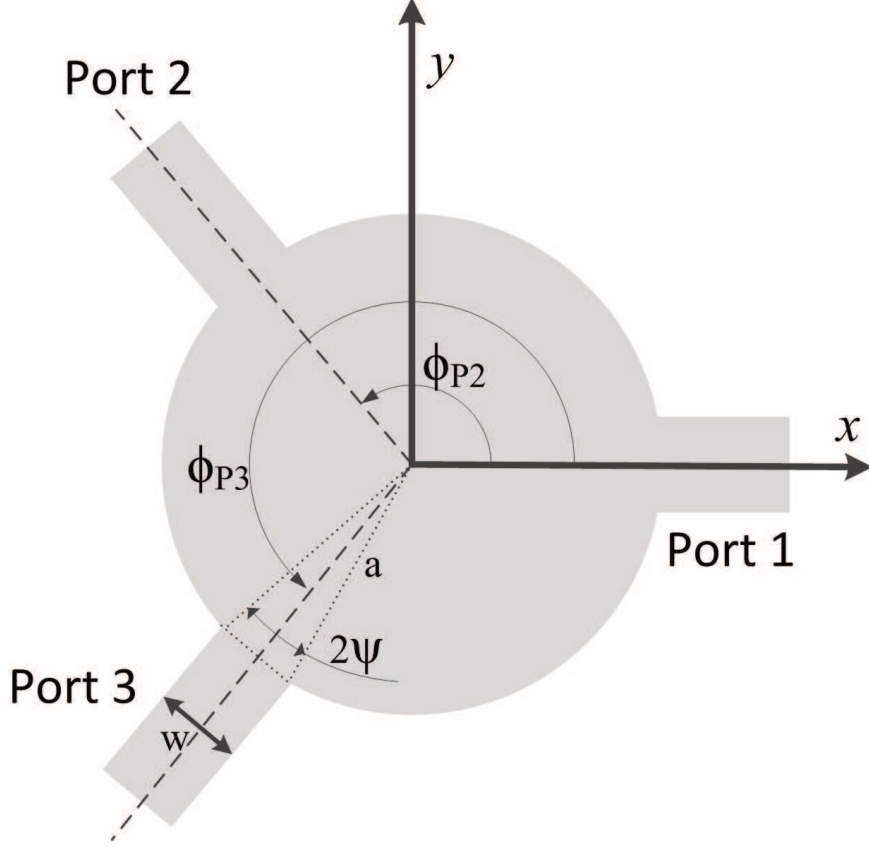


Figure 5.1: A schematic for the junction circulator.

$$X_{in} = \text{Im} \left\{ \frac{Z_0}{\eta_0} (\eta_{11} + \eta_{12}) \right\} = 0 \quad (5.34)$$

After assuming a particular value for g_κ , the coupling angle ψ and the value of x can be obtained to satisfy the previous condition. As such, the material and the physical dimensions are determined. Hence, the scattering parameters are calculated from the impedance matrix by:

$$[S] = \left(\frac{Z_r}{\eta_0} [\eta] + [I] \right)^{-1} \left(\frac{Z_r}{\eta_0} [\eta] + -[I] \right) \quad (5.35)$$

5.3 The RGW Circulator Design

In this section, a detailed procedure is presented for the circulator design. The previous analysis is directed to obtain the ferrite disc specification to satisfy the circulatory conditions. Based on the required operating frequency the procedure can be classified in the following steps:

1. RGW circulator with ideal boundary conditions: In this part, the RGW is implemented with a PMC boundary, where the following approach is proposed.
 - (a) Assuming the Gyropy value in the range between -1 to 0 for below resonance mode of operation. It is recommended to be limited in between -0.2 and -0.8 to avoid resonance losses and below saturation losses. These facts are addressed in many articles and textbooks [92,93]. It is possible also to select positive values of the Gyropy for above resonance mode of operation, but this usually gives a smaller operating bandwidth [93]. Then the saturation magnetization of the ferrite disc can be calculated through

$$4\pi M_s = \frac{g_\kappa f_d}{2.8 \times 10^6} \quad (5.36)$$

- (a) The input reactance is equated to zero to find the ferrite radius and the coupling angle.
- (b) The ferrite height is assumed, where $h_f < a$ (assume $h_f = 0.4a$). This condition to ensure the neglected axial variations as assumed in the analysis. This is a design parameter, which means that this height can take many other values as long as the axial variation is neglected.
- (c) The input resistance is calculated at the design frequency.
- (d) Design the matching network to connect the junction to the feeding line.
It must be taken into consideration that the permittivity of the RGW

should be smaller than the ferrite permittivity. As such, a PMC boundary assumption at the perimeter of the ferrite disc between the ports is a valid approximation. A roughly estimated limit is that $\varepsilon_{d,max} = 0.8\varepsilon_f$, where the dielectric filling of the RGW has a relative permittivity of ε_d , while the ferrite relative permittivity is ε_f . There are no definite limits for the maximum value of the dielectric permittivity deployed for matching. However, the PMC boundary assumption is more violated when both values are getting closer. After calculating the required value of the relative permittivity for the matching, a lower value should be considered. The objective is the RGW circulator design, which has more fringing fields around the ridge compared to the model with PMC surface. This results in having a larger effective electrical width than the physical width. The characteristic impedance of RGW will be smaller than the ideal model. To compensate for this phenomenon, in advance, the utilized dielectric constant is lower than the required one by 30%.

- (e) Finally, the analytically predicted response of the scattering parameters has to be compared to the simulated response based on ideal boundary conditions.

2. RGW circulator realization: The objective of this step is to replace the PMC boundary around the ridge with the periodic cells. To achieve that, the following procedure should be performed:

- (a) Design the periodic cell with the same gap height with a bandgap that contains the circulator operating bandwidth.
- (b) Replace the ideal PMC surface with the designed cells. Hence, further optimization should be performed to obtain the required response, if needed.

5.3.1 RGW Circulator with Ideal Boundary Conditions

As mentioned before the design frequencies are $f_{d1} = 15$ GHz and $f_{d2} = 30$ GHz. The assumed Gyropy is chosen to be -0.6 . This value is a design parameter, i.e. it can be selected with any value in the specified range. The saturation magnetization of the ferrite is calculated to be $4\pi M_s = 3214.3, 6428.6$ G, respectively. The dielectric constant of the ferrite materials should be obtained from the ferrite provider. The nominal value of this parameter is in between 12 and 15. An example of the ferrites is the TT1-3000, listed in [3] with $\varepsilon_f = 12.9$. The ferrite materials can be custom made with a specific $4\pi M_s$ or can be ordered with standard values. If the required material is not available, the designer can use a material with slightly less $4\pi M_s$ and obtain the same Gyropy by some extra magnetization. It is assumed here that the required value is available. The material deployed in the design has $4\pi M_s = 3214.3$ and 6428.6 G and $\varepsilon_f = 12.9$.

The input impedance imaginary part is equated to zero. This results in a coupling angle $\psi = 0.5344$ radian for both designs and ferrite disc radii are $a_1 = 0.0686''$ and $a_2 = 0.0343''$. Hence, the ferrite heights can be assumed to be $h_{f1} = 0.0274''$ and $h_{f2} = 0.0137''$. It is important to notice that, both, the coupling angle and the disc radius, determine the ridge width. This width W_r can be calculated through Equation 5.16, where $W_{r1} = 0.0699''$ and $W_{r2} = 0.0349''$. The input resistance of the ferrite disc is equal to 16.82Ω in both cases, but the characteristic impedance of the air filled RGW is 54.98Ω . The RGW characteristic impedance is calculated approximately through the stripline equation [3]

$$Z_0 = \frac{30\pi}{W_e/b + 0.441} \quad (5.37)$$

The required dielectric constant to ensure the matching is above 10. As mentioned before, the selected filling material of $\varepsilon_d = 7.75$, which is around 30% below the

required value of the matching. Figure 5.2 illustrates the simulated model of the ideal RGW, where Figure 5.2 (c) focuses on the top PEC boundary condition in green and Figure 5.2 (d) shows the PMC boundary in a blue color. The PMC boundary is considered only to obtain the ideal RGW response. Figure 5.2 also illustrates the curved shaped lines in Ports 2 and 3. The main reason behind this curvature is to show the ability to align all ports at the principal planes, which is a standard mechanical requirement in these devices. The comparison between the analytical and the simulated response is shown in Figure 5.3 (a) and (b), for both designs. The circulator response is considered in a 40% bandwidth centered at the design frequency. It can be depicted from these figures that the designs are shifted down in frequency, intentionally. This shift is due to the deployed matching section. The dielectric constant used in matching is less than the required value in order to compensate for the expected change in the characteristic impedance of the ridge. Both designs cover more than 25% bandwidth with a matching and isolation levels of -15 dB, while the proposed bandwidths for 5G mobile applications do not exceed 10%. In addition, the realization of this design by RGW will compensate for the frequency shift, which will increase the circulator bandwidth. This will be explained in the following subsection.

5.3.2 RGW Circulator Realization with Periodic Cells

The periodic cells deployed in this design are the traditional bed of nails unit cell (BNUC). These types of cells can achieve a bandwidth better than 2:1. In some applications, when the operating bandwidth exceeds 2.5:1, other types of unit cells have to be used. The design of the BNUC is visited in many publications. The designed unit cell is shown in Figure 5.4 (a) and (b), while the Eigenmode solution is provided in Figure 5.4 (c). The cell dimensions are the cell width W_c , the pin width W_p , the gap height h_g and the pin height h_p . The values of these parameters are listed in Table 5.2 for both designs, where the gap height of the cell is precisely equal

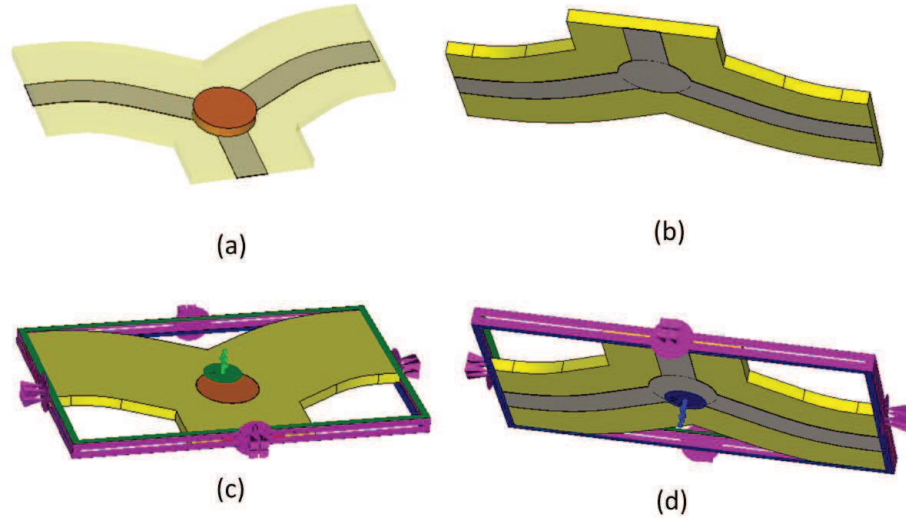


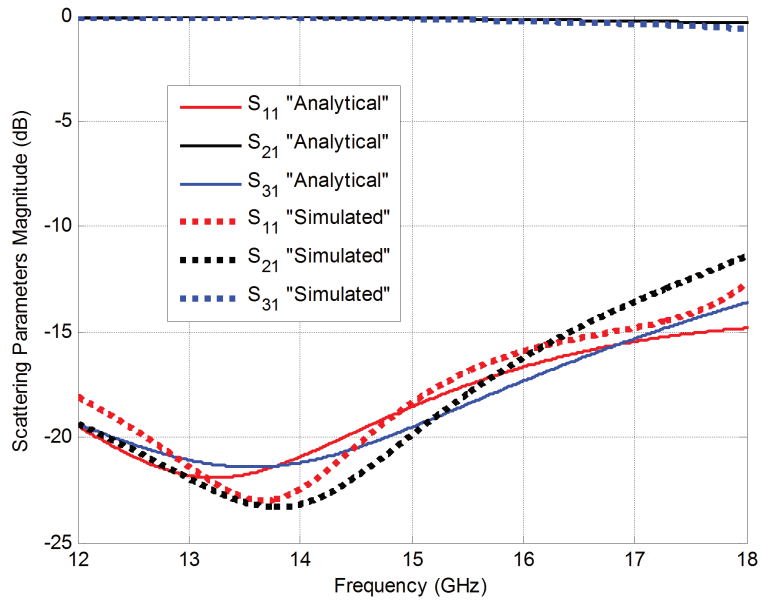
Figure 5.2: The simulated model of the RGW circulator.

Table 5.2: The bed of nail unit cell dimensions.

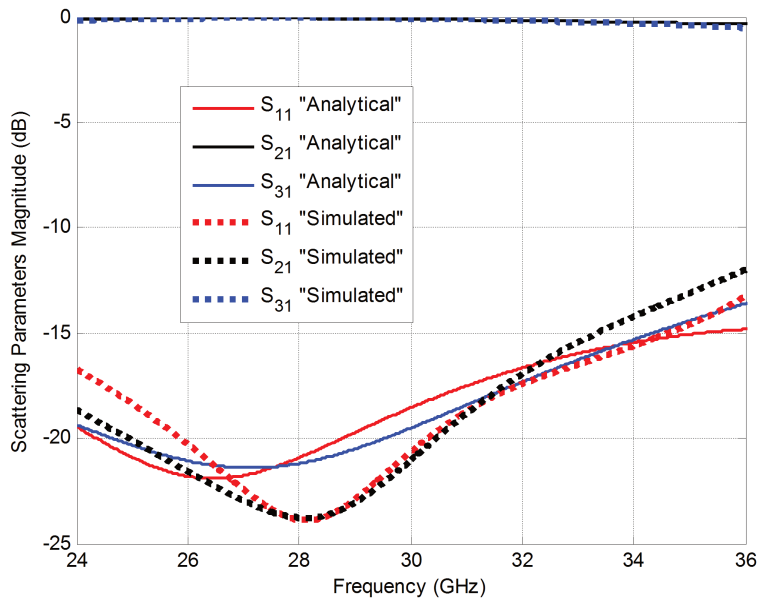
The Dimension	Design 1 Value (inch)	Design 1 Value (inch)
W_c	0.1813	0.0515
W_p	0.0976	0.0343
h_g	0.0279	0.0137
h_p	0.1813	0.0984

to the ferrite disc height. It can be depicted from Figure 5.4 (c) and (d), that the stopband of the designed cells covers wider bands in both cases.

The cells are placed surrounding the ridge to keep the PMC boundary conditions assumed in the ideal design. The circulator configuration is shown in Figure 5.5 (a), where the upper ground is removed to show the structure details. The responses of the final designs are presented in Figure 5.5 (b) and (c). It is evident from these figures that the curves are shifted up again. The practical ridge implementation has more field fringing around the ridge compared to the ideal PMC boundaries, which increases the effective width of the ridge. The wider ridge reduces the characteristic impedance of the feeding line, which compensates the characteristic impedance of the matching network. The final design covers, almost, a 40% bandwidth with a matching level of -15 dB.



(a)



(b)

Figure 5.3: The comparison between the analytical and the simulated response of the RGW circulator with ideal PMC around the ridge. (a) Design example 1. (b) Design example 2.

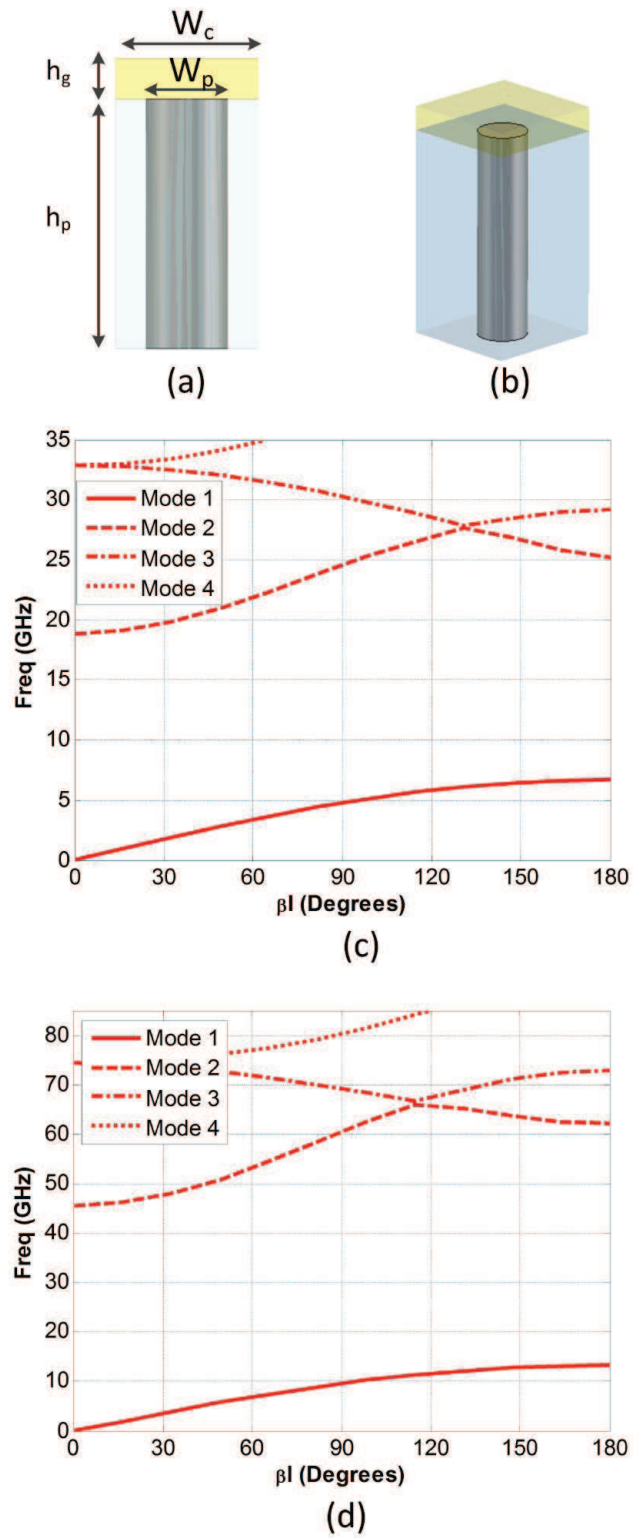
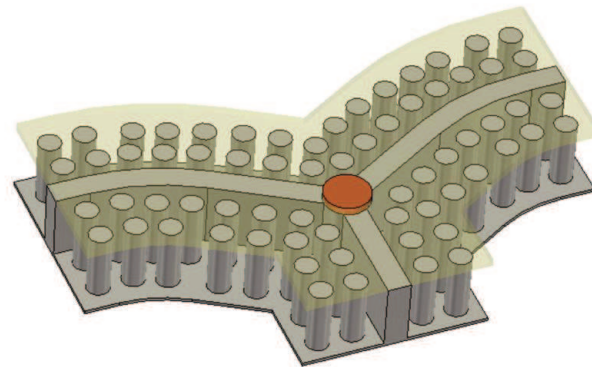
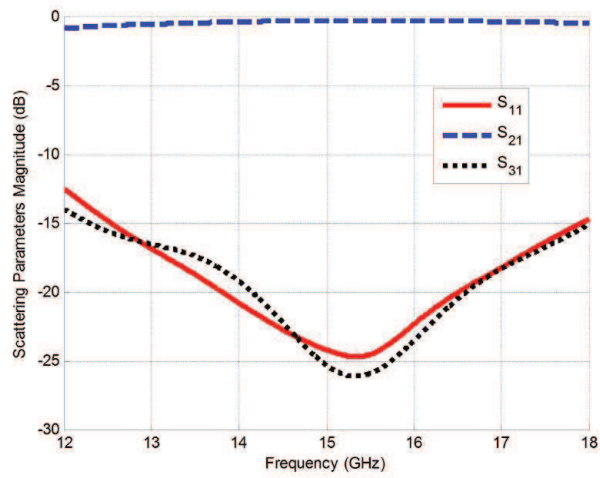


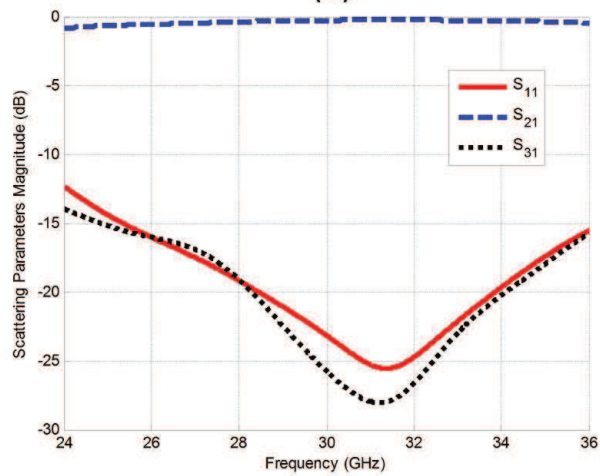
Figure 5.4: The unit cell (a)Front view. (b) 3D view. (c) Cell 1 dispersion relation. (d) Cell 1 dispersion relation.



(a)



(b)



(c)

Figure 5.5: The realized RGW circulator (a) 3D structure. (b) Design 1 scattering parameters. (c) Design 2 scattering parameters.

5.4 Summary of the Introduced Components

In the previous four chapters, the measurement setup, as well as the accurate estimation of the RGW bandwidth have been introduced. Moreover, samples of reciprocal and non-reciprocal devices have been put in place. The design methodology of these components has been illustrated in details. In the following chapter, some application will be introduced to utilize these transitions and components in textile material measurements and antenna applications.

Chapter 6

Applications of Ridge Gap Waveguide Devices

This work introduced a step toward the standardization of the RGW technology. Different transitions have been presented. In addition, better analysis techniques have been proposed, especially, for the bandwidth evaluation. Moreover, samples of reciprocal and non-reciprocal devices have been introduced. These previous contributions can be deployed in many applications. In this chapter, two examples will be given to utilizing the RGW technology in different applications. The first application is textile material characterization through using a straight RGW. The second application is a grating lobe free slot antenna array fed by anti-phase two ridge gap waveguides.

6.1 Textile Material Characterization using RGW Technology

Wearable antennas and microwave medical applications create a high potential to utilize and characterize the textile materials in microwave applications. Although these materials have well known mechanical characteristics, but it is not enough for

deploying in antenna applications. The electrical characteristics, especially the relative permittivity, are key elements in the antenna design process. Many traditional methods to identify the relative permittivity of unknown materials are presented in the literature. Resonance techniques and cavity perturbations were introduced, 50 years ago, to determine the dielectric permittivity [3, 94–96]. Another well-known method is to identify the dielectric constant by performing measurements inside waveguides [97–99]. The coaxial probe method and the free space method are some of the presented techniques as solutions to the same problem. It is evident that the previously mentioned methods are general techniques used with any type of materials. These methods are applied to ceramics and substrates, for microstrip line and coplanar waveguide applications, for example [100, 101]. Some of these methods are applied even to semiconductors and liquids [96, 102]. The measurement techniques of the relative permittivity are developed rapidly to be extended for higher frequency bands [103] or to be applied to new materials such as textile materials. In the case of textile materials, the standard thicknesses are relatively small. This adds limitations of the used measurement technique. This work introduces a novel methodology for relative permittivity measurements that can be listed in the category of guided structure measurements. The goal of this partial is to propose a suitable measurement technique for wideband operation and a small thickness of the sample under test through using the Ridge Gap Waveguide (RGW). The proposed methodology has an advantage of utilizing only the scattering parameters steady-state magnitude. Some dielectric constant measurement techniques are based on time domain measurements [12] other needs the complex value of the scattering [13]. In both cases, the measurement devices imperfection affects the algorithm accuracy severely. This imperfection has more effects on high frequency measurements. As the signal propagates inside an RGW in the form of quasi-TEM, it is subjected to minimal dispersion. The signal is also subjected to small attenuation as there are no dielectric losses inside the

structure.

The configuration also requires no electrical contacts between its lower and upper parts, which is a major problem in other structures like rectangular waveguides. The ridge gap waveguide is similar to the traditional ridge waveguide in terms of the widebandwidth while carrying the TEM mode is giving this new structure a better performance compared to the traditional ridge waveguide. Two major characteristics of this configuration are the main reason behind the idea of using RGWs in the relative permittivity extraction procedure. The quasi-TEM mode of propagation and the small gap thickness encourage the employment of RGW in the measurement setup. The wideband is another important feature of this technology. RGWs have a bandwidth of 2.5:1 and this band can be increased by modifying the shape of the unit cells that surround the ridge.

RGWs measurements have been presented in many papers before, but most of them are performed only for small bandwidth relative to the possible band of this guiding structure or with relatively lossy transition [10, 12, 28]. The idea presented, here, to identify the relative permittivity depends on extracting the dispersion relation of the propagating signal inside the RGW filled with the sample under test. Extracting the dispersion relation of a specific mode is quite simple if the numerical solution of the whole structure exists. This case is addressed before in some publications, where the FDTD solution is developed to generate the dispersion relation of each mode [35, 36]. Other methods are presented to extract the RGW dispersion relation in a closed form solution by solving the wave equation inside the periodic cells [32, 33] or having a surface equivalent impedance of the cells top surface [34]. The proposed algorithm, in this work, is able to extract the dispersion relation of the RGW with no prior knowledge of the infill material relative permittivity.

In the following section, a detailed description is given for the used measurement setup and the excitation technique for the whole experiment. This is followed by

a section for the mathematical formulation to extract the relative permittivity out of the measured data. The relation between the effective and relative permittivity and the effect of the relative permittivity value on the measurement bandwidth are discussed in two successive sections. In section 6.1.6, some benchmark examples are illustrated to validate the proposed algorithm. The algorithm application on many samples of textile materials is discussed in a separate subsection.

6.1.1 The Measurement Setup Description

The proposed setup consists of an RGW structure with a total length of 10 cells. This line is excited through 2.92 mm coaxial connector to RGW transition. This transition covers the whole possible bandwidth with a matching level below 15 dB for the double transitions, as described in a previous chapter. Figure 6.1a shows the cross section of the structure and Figure 6.1b shows the 3D model of the complete setup. The model takes into consideration the coaxial ports and the 2.92 mm connectors. It also considers the transitions from the coaxial ports to RGW and vice versa. The middle section of this model is the straight RGW. The sample under test has to be placed in this middle section as will be explained later. The first step is to measure the setup response in the case of air filling RGW. The calibrated measured transmission coefficient phase contains the air filled RGW dispersion relation. In the case of an air filled guide, it is very important to obtain the dispersion relation for the relative permittivity calculations. The second step is to place the sample under test (SUT) inside the gap of the RGW. Performing the calibration via the TRL method shifts the reference plane to be exactly at the starting point of the sample under test. The scattering parameters are obtained while the textile material is filling the gap. The overall insertion loss and return loss curves are of a sinusoidal behavior. The mathematical formulations are discussed in detail in the next section. It is worth

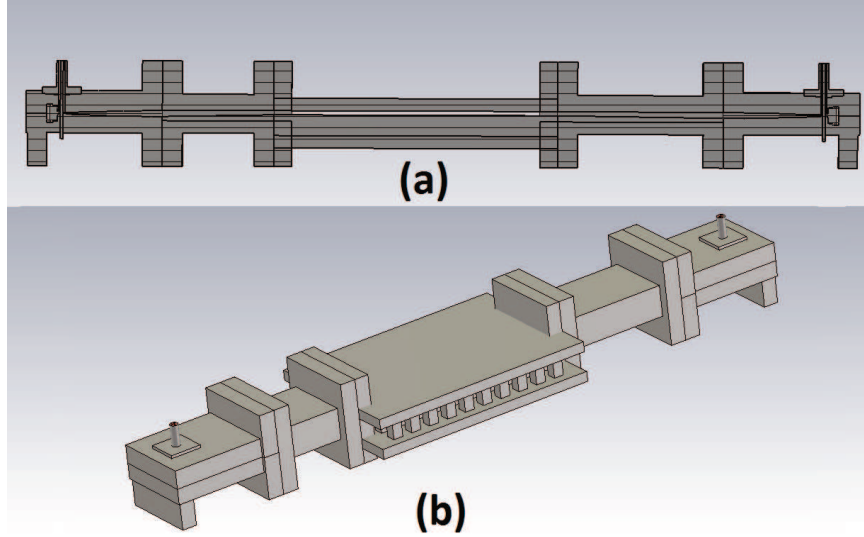


Figure 6.1: The simulated model of the complete setup (a) Cross section. (b) 3D model.

mentioning that although the reflection coefficient is a function of the relative permittivity, the proposed methodology is based on extracting the required information through the dispersion relation.

6.1.2 The Proposed Algorithm Mathematical Formulations

This relies on having only one propagating mode within the operating bandwidth of the RGW. The block diagram of the SUT in between the two ports is shown in Figure 6.2, where the wave impedance of the sample under test and the port impedance are Z_1 and Z_0 , respectively. The signal passes through the interface between the first port and the sample under test; then it suffers from an infinite number of reflections between both faces. This is a simple block diagram to model the loaded RGW with the material under test in between two air-filled gap waveguides. The total reflected signal is the summation of the first reflection and the series of the backward transmitted signal components. The total transmitted signal can be expressed as a summation of the forward transmitted signal components. The first forward transmitted component is the multiplication of the signal amplitude and both transmission factors T , T' and

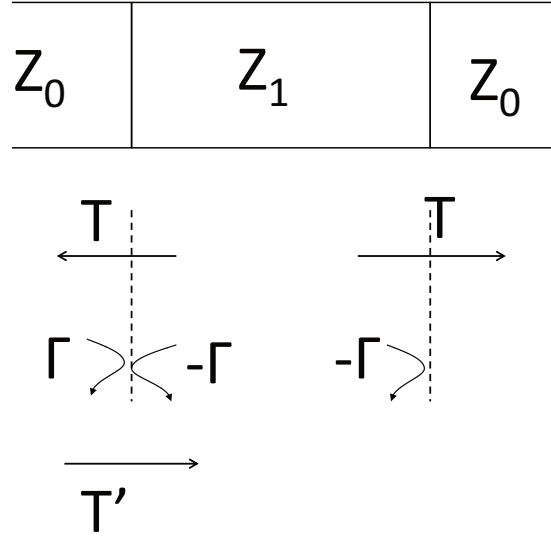


Figure 6.2: The SUT block diagram.

the propagation term along the sample under test. This results in $AT T' e^{-j\beta l}$, which can be simplified into the following form $A(1 - \Gamma^2) e^{-j\beta l}$ as T and T' are equal to $(1 - \Gamma)$ and $(1 + \Gamma)$ respectively. The signal reflects two times and propagates for a distance of $2l$ between each two reflections. The previous term is multiplied by $\Gamma^2 e^{-j2\beta l}$ to get next terms.

Based on what is mentioned above, the output signal at port 2 can be written as follows:

$$S_{out2} = A(1 - \Gamma^2) e^{-j\beta l} [1 + \Gamma^2 e^{-j2\beta l} + \Gamma^4 e^{-j4\beta l} + \dots] \quad (6.1)$$

$$S_{out2} = \frac{A(1 - \Gamma^2) e^{-j\beta l}}{1 - \Gamma^2 e^{-j2\beta l}} \quad (6.2)$$

Similarly for the return loss curve, $A\Gamma$ is the first reflection, while the first component in the back reflected series passes through the first port interface in both

directions and reflects on the far port only once. It is also evident that the signal propagates for $2l$ distance. The total reflected term can be written as follows,

$$S_{out1} = A\Gamma\{1 - (1 - \Gamma^2)e^{-j2\beta l} [1 + \Gamma^2e^{-j2\beta l} + \Gamma^4e^{-j4\beta l} + \dots]\} \quad (6.3)$$

$$S_{out1} = A\Gamma\left\{1 - \frac{(1 - \Gamma^2)e^{-j2\beta l}}{1 - \Gamma^2e^{-j2\beta l}}\right\} \quad (6.4)$$

Equations (6.2) and (6.4) are used to get an expression for the scattering parameters for the sample under test to be

$$S_{11} = \Gamma \left[\frac{1 - e^{-j2\beta l}}{1 - \Gamma^2 e^{-j2\beta l}} \right] \quad (6.5)$$

$$S_{21} = \frac{(1 - \Gamma^2)e^{-j\beta l}}{1 - \Gamma^2 e^{-j2\beta l}} \quad (6.6)$$

The general complex value of the reflection coefficient is $\Gamma = |\Gamma|e^{j\theta_\Gamma}$ at each interface. Starting from equations (6.5) and (6.6), expressions for the S-parameters magnitude can be obtained as follows

$$|S_{11}| = |\Gamma| \frac{\sqrt{2 - 2\cos(2\beta l)}}{\sqrt{1 + |\Gamma|^4 - 2|\Gamma|^2 \cos(2\beta l + \theta_\Gamma)}} \quad (6.7)$$

$$|S_{21}| = \frac{\sqrt{1 + |\Gamma|^4 - 2|\Gamma|^2 \cos(2\theta_\Gamma)}}{\sqrt{1 + |\Gamma|^4 - 2|\Gamma|^2 \cos(2\beta l + \theta_\Gamma)}} \quad (6.8)$$

For the propagating mode inside the sample under test, the wave impedance is a pure real value. The angle of the reflection coefficient equals to $n\pi$. Replacing θ_Γ with $n\pi$ in Equation (6.8) results in

$$|S_{21}| = \frac{(1 - |\Gamma|^2)}{\sqrt{1 + |\Gamma|^4 - 2|\Gamma|^2 \cos(2\beta l + \theta_\Gamma)}} \quad (6.9)$$

The previous equation shows that the transmission coefficient has a sinusoidal behavior. The cos term is oscillating between 1 and -1. The minimum value of the transmission coefficient can be expressed by the following equation

$$|S_{21}|_{min} = \frac{1 - |\Gamma|^2}{1 + |\Gamma|^2} \quad (6.10)$$

The idea of the extraction algorithm is to find the minima and maxima of the transmission coefficient curve over a particular frequency band and equating the “cos” term with ± 1 , which corresponds to the maximum and minimum of the reflection coefficient. It is very clear in equations (6.7) and (6.8) when the “cos” term is equal to 1 the value of the reflection reaches its minimum value at 0, while the transmission coefficient will be equal to its maximum value. It is important to keep in mind that in some cases, where $|\Gamma|$ is very small, recognizing the minimum and the maximum in the transmission coefficient is difficult and the values of $|S_{21}|_{max}$ and $|S_{21}|_{min}$ are very close to each other. In these cases, finding the minima of the return loss curve is more suitable and accurate. The previous analysis leads to having the following two cases.

- Case 1: $\theta_\Gamma = 2n\pi$
 - $|S_{21}|_{max}$ at $2\beta l = 0, 2\pi, 4\pi, \dots$
 - $|S_{21}|_{min}$ at $2\beta l = \pi, 3\pi, 5\pi, \dots$
- Case 2: $\theta_\Gamma = (2n + 1)\pi$
 - $|S_{21}|_{max}$ at $2\beta l = \pi, 3\pi, 5\pi, \dots$
 - $|S_{21}|_{min}$ at $2\beta l = 0, 2\pi, 4\pi, \dots$

The proposed extraction algorithm contains two major steps:

1. Indicate the frequency points correspond to the minima and maxima locations in the magnitude of S_{21} , or the corresponding values of the maxima and minima of S_{11} magnitude .
2. Equate $2\beta l$ with $2n\pi$ starting with 0 at the starting propagating frequency.

Applying the previously discussed algorithm, the dispersion relation curve for the RGW filled with the dielectric material can be extracted. The phase constant of the RGW filled with dielectric can be related to the same quantity of the air-filled through

$$\beta_{filled} = \beta_{air\ gap} \sqrt{\epsilon_{eff}} \quad (6.11)$$

By plotting the curve $\beta_{filled}/\beta_{air\ gap}$ the required quantity is equal to the curve slope squared. It is very important to note that the algorithm finds the effective permittivity, while the final target is to obtain the relative permittivity. This creates the need of having a general relation between the effective permittivity and the relative permittivity or at least a curve that describes this relation for the guided structure used in the measured setup.

6.1.3 The Tolerance Analysis of the Proposed Algorithm

The previous algorithm is based on two major assumptions, which are having a lossless and frequency independent material under test. In this section, a tolerance analysis is performed to study the case of low loss and frequency-dependent materials. Taking into consideration the low loss materials, the complex relative permittivity can be written as follows

$$\epsilon_{rc} = \epsilon_r (1 - j \tan(\delta)) \quad (6.12)$$

to introduce frequency dependent to the losses, the imaginary part is considered with the dielectric conduction losses [3], where

$$\tan(\delta) = \frac{\sigma}{\omega\epsilon_r\epsilon_0}. \quad (6.13)$$

This leads to generalizing equations (6.5) and (6.6) to be as follows:

$$S_{11} = \Gamma \left[\frac{1 - e^{-2\alpha l} e^{-j2\beta l}}{1 - \Gamma^2 e^{-2\alpha l} e^{-j2\beta l}} \right] \quad (6.14)$$

$$S_{21} = \frac{(1 - \Gamma^2) e^{-2\alpha l} e^{-j\beta l}}{1 - \Gamma^2 e^{-2\alpha l} e^{-j2\beta l}} \quad (6.15)$$

Moreover, the complex value of the reflection coefficient at each interface is $\Gamma = |\Gamma|e^{j\theta_\Gamma}$, where the phase can be related to the material parameters with the following expression

$$\theta_\Gamma = \tan^{-1} \left[\frac{2(1 - \sqrt{\epsilon_r})}{\sqrt{\epsilon_r} \tan(\delta)} \right] + \tan^{-1} \left[\frac{2(1 + \sqrt{\epsilon_r})}{\sqrt{\epsilon_r} \tan(\delta)} \right] \quad (6.16)$$

In this general case, the magnitude of the scattering parameters can be expressed as

$$|S_{11}| = \frac{|\Gamma| \sqrt{1 + e^{-4\alpha l} - 2e^{-2\alpha l} \cos(2\beta l)}}{\sqrt{1 + |\Gamma|^4 e^{-4\alpha l} - 2e^{-2\alpha l} |\Gamma|^2 \cos(2\beta l + \theta_\Gamma)}} \quad (6.17)$$

$$|S_{21}| = \frac{\sqrt{1 + |\Gamma|^4 e^{-4\alpha l} - 2e^{-2\alpha l} |\Gamma|^2 \cos(2\theta_\Gamma)}}{\sqrt{1 + |\Gamma|^4 e^{-4\alpha l} - 2e^{-2\alpha l} |\Gamma|^2 \cos(2\beta l + \theta_\Gamma)}} \quad (6.18)$$

for low loss materials under test the term $e^{-2\alpha l}$ is approaching 1, and the angle of the reflection coefficient equals to $n\pi$, which retrieves the same equations described before in the case of lossless frequency independent materials. Applying the same algorithm to extract the phase constant implies that $2(\beta_{extracted})l$ will be equated by $2n\pi$ or $2(n+1)\pi$. The extracted value of the phase constant through the proposed

algorithm can be expressed as follows

$$\beta_{extracted} = \beta (1 + \Delta\beta/\beta) \quad (6.19)$$

and the error in the extracted value of the phase constant is related to the loss tangent by the following equation

$$\begin{aligned} \Delta\beta/\beta = & \frac{1}{2l\beta} \left\{ \tan^{-1} \left[\frac{2(1-\sqrt{\epsilon_r})\epsilon_r\epsilon_0\omega}{\sigma\sqrt{\epsilon_r}} \right] \right. \\ & \left. - \tan^{-1} \left[\frac{2(1+\sqrt{\epsilon_r})\epsilon_r\epsilon_0\omega}{\sigma\sqrt{\epsilon_r}} \right] \right\} \end{aligned} \quad (6.20)$$

Based on the relation between the relative permittivity and the phase constant the error in the relative permittivity can be proved to have the following expression

$$\Delta\epsilon_r/\epsilon_r = 1 - (1 + \Delta\beta/\beta)^2 \quad (6.21)$$

The previous expression is a function of the frequency and the material conductivity. To study the effect of having lossy and frequency dependent material, Figure 6.3 is plotted for a material of relative permittivity of 1.96, which is the case of RT 5880 LZ standard substrate. It can be depicted from this curve that the error in the real part of the relative permittivity is about 1% in the case of $\sigma = 0.1$ and a frequency of 10 GHz.

Another factor that can affect the measured value of the dielectric constant is the thickness of the sample under test. The proposed algorithm assumes that the sample completely fills the gap above the ridge. In the case of any deviation for the height of the sample, an air gap between the sample and the top ground may occur, or if the sample is thicker, it will be compressed without possible air gaps. In the latter case, the permittivity might differ than the actual one as well to be higher. This

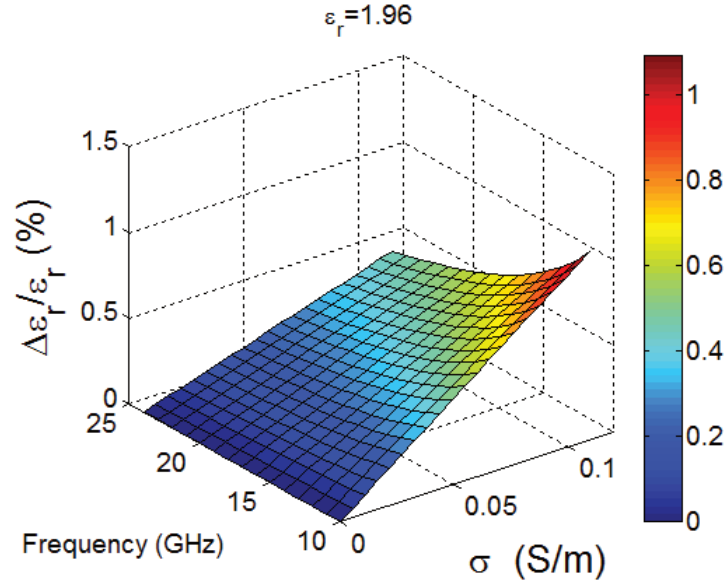


Figure 6.3: The error in the relative permittivity with both the material conductivity and the measurement frequency.

leads to a different effective value of the extracted phase constant, which results in a variation of the effective value of the relative permittivity. The previously described problem has a significant effect on the extracted values of high relative permittivity materials. However, its effect is reduced as the sample dielectric constant decreases. The objective materials to be tested in this work are the textile materials, which generally have a low dielectric constant. In the following part, the case of an air gap above the sample under test (SUT) is considered.

The effect of an air gap above SUT

The existence of an air gap above the sample under test (SUT) results in having a lower measured relative permittivity than the actual value. This occurs when the sample height is slightly less than the gap height. The measured relative permittivity can be expressed as:

$$\epsilon_r^{(m)} = \frac{\epsilon_r(h - h_a) + h_a}{h} \quad (6.22)$$

where h_a represents the air gap height above the sample under test. The percentage error in the relative permittivity value can be expressed as:

$$\frac{\Delta\epsilon_r}{\epsilon_r} = \frac{h_a}{h} \left[1 - \frac{1}{\epsilon_r} \right] \quad (6.23)$$

This expression indicates that an error of 10 % in the height of the sample under test leads to an error of 3 % in the relative permittivity value if the relative permittivity is in the range of 1.5. This error increases to 9 % for samples of relative permittivity around 10. Based on this, the existence of an air gap above the sample under test has a minimal effect because the textile material, generally, have low dielectric constants.

6.1.4 The Relation Between the Effective and the Relative Permittivity

The basic idea of this work is to deploy the RGW in the measurement of the dielectric constant. The available RGW structure in the lab has the dimensions listed in Table 6.1 with the cross section illustrated in Figure 6.4 where all dimensions are indicated in this figure. This cross section has the ridge in the middle surrounded by periodic nails from both sides. The nails and the ridge have the same length. Both the ridge and the nails have the same gap height with the upper ground. Performing many simulations with different values of the relative permittivity and extract the corresponding effective permittivity through the simulation tool, Figure 6.5, can be obtained. This is based on simulating an RGW filled with material of a predetermined dielectric constant and calculate the corresponding effective permittivity. The effective relative permittivity is calculated from the phase constant using the quasi-TEM assumption. The simulation is repeated for many values of the relative permittivity in the range of 1 to 3, while the corresponding effective permittivity is

Table 6.1: The available RGW dimensions in the lab.

The Dimension	The Value (mm)
Ridge width (W_r)	5
Pin height (d)	5
Cell size (a)	6
Gap height (h)	1
Pin width (b)	3

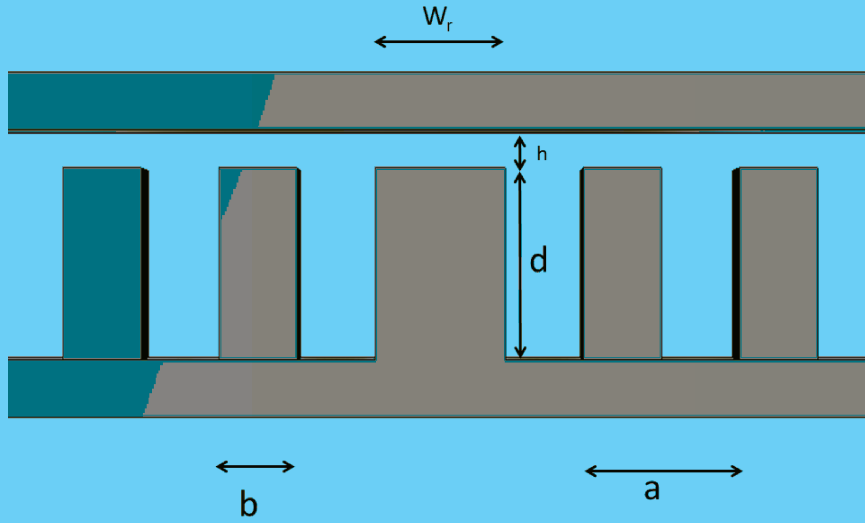


Figure 6.4: The RGW dimensions.

calculated. This curve is generated, specifically, for the RGW with dimensions mentioned in Table 6.1. The curve will be used in the last step of the proposed algorithm to obtain the value of the dielectric constant corresponding to the extracted effective permittivity in each case. The relative permittivity range, in this curve, is below 3. The reason behind this limited range of the dielectric constant values is the reduction of the measurement bandwidth with high values of the relative permittivity, which is discussed, in details, in the subsequent section.

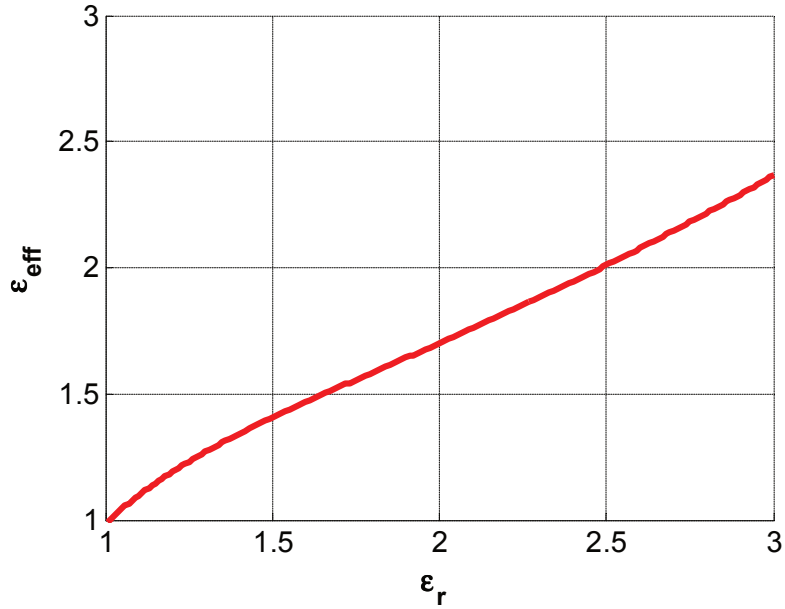


Figure 6.5: The relation between the effective and the relative permittivities.

6.1.5 The Operating Bandwidth of ϵ_r Measurement

The proposed algorithm is based on having single mode inside the middle section, where the SUT is placed. The air filled RGW has the maximum possible operating bandwidth. Figure 6.6 illustrates the dispersion relation of the air filled RGW. The operating bandwidth can be seen in the previous figure to start at 11 GHz and end at 23 GHz. The actual operating bandwidth is slightly less than the bandgap of the periodic cell due to the ridge existence.

Adding any material inside the gap between the ridge and the upper ground decreases the operating bandwidth. Figures 6.7 and 6.8 illustrate the dispersion relation of the ridge gap waveguide partially filled with material of $\epsilon_r = 2$ and 3, respectively. The RGW mode is the quasi-TEM mode, where the dispersion relation is linear in the operating bandwidth. The dispersion relation linearity leads to a straightforward extraction procedure. Moreover, these figures indicate that as the relative permittivity increases, the operating bandwidth decreases. It is evident also that the lower end of the operating bandwidth is constant while the upper limit is going down as the

dielectric constant increases. These figures are extracted for the RGW with the listed dimensions for the available measurement setup. As the proposed algorithm is valid as long as there is a single mode propagating along the ridge in the measurement band, this is a limitation of the extracted value of the relative permittivity using this setup. The objective materials are the textile materials, where the expected range of the relative permittivities is relatively small. The expected value of the relative permittivity is less than 3, and this makes the available setup valid for measuring the dielectric constant of the objective materials. It is important to mention that the limitation here is due to the possible setup. The available range of the measured relative permittivities can be expanded by decreasing the gap height of the RGW used in the measurement procedure.

The previous analysis gives an impression of having some contradiction with the objective of the algorithm as it shows that the operating bandwidth is affected significantly by the dielectric constant of material under test. Although the bandwidth is affected by the filling material, the cell design can be modified to provide sufficient bandwidth initially. Some proposed cells in the literature are able to provide an operating bandwidth ratio of 3 to 1 and even more [29]. The study in the previous part focused on the already fabricated setup to utilize the available resources. However, the algorithm can be applied to better ridge gap waveguide designs.

6.1.6 The Proposed Algorithm Validation

For the validation of the proposed algorithm, the configuration shown in Figure 6.9 is simulated. In this figure, a dielectric filled RGW is placed in between two air filled RGWs. The filling dielectric height is exactly equal to the gap height while the width is equal to the ridge width. The upper ground is plotted in a transparent color in order to show the internal details of the structure and the sample position. In the case of increasing the width, some resonance frequencies are generated within

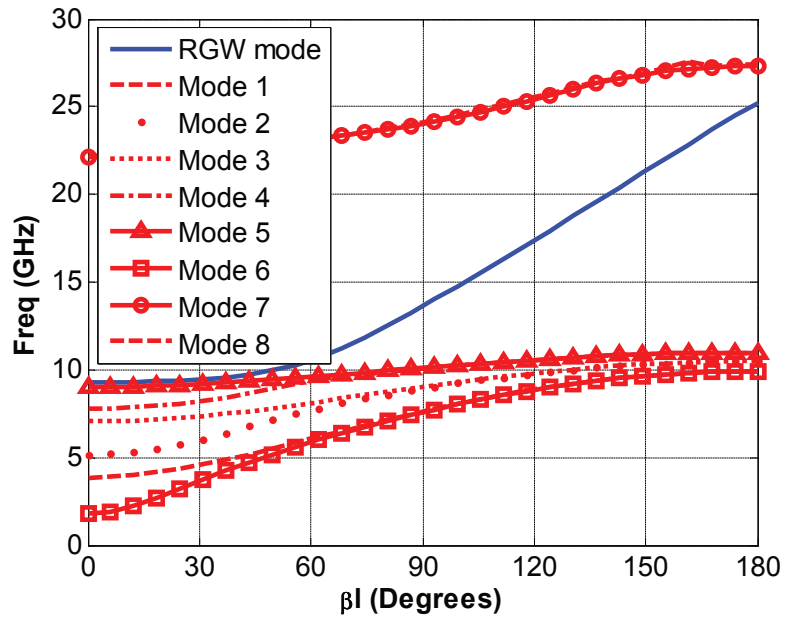


Figure 6.6: The dispersion relation of an air filled RGW in the existence of the ridge.

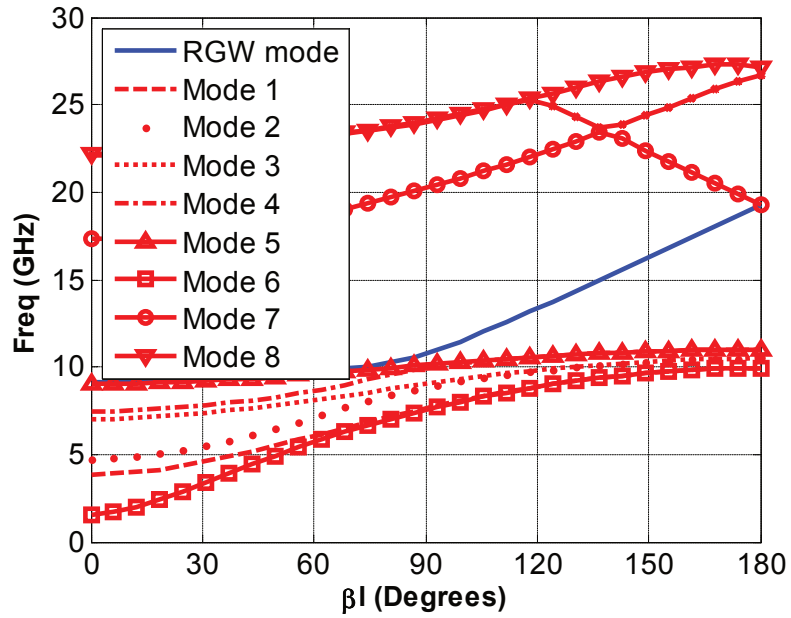


Figure 6.7: The dispersion relation of a partially filled RGW in the existence of the ridge ($\epsilon_r = 2$).

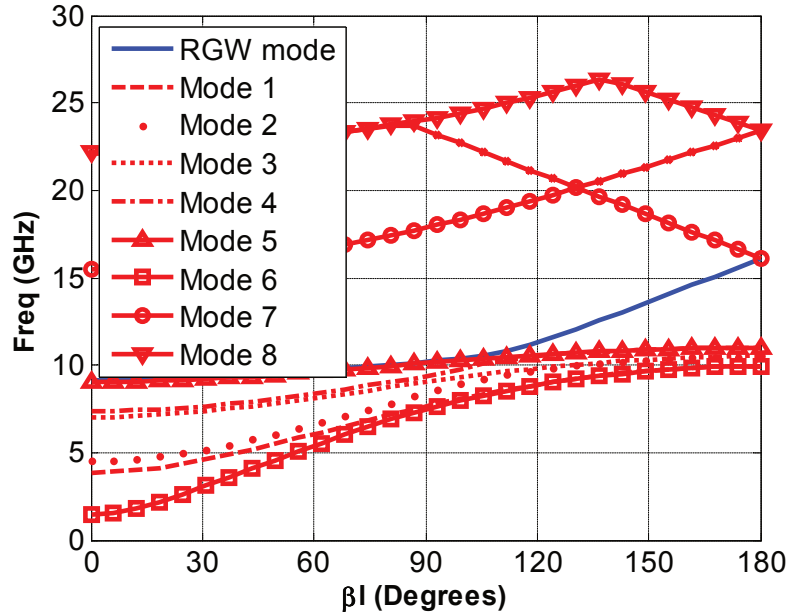


Figure 6.8: The dispersion relation of a partially filled RGW in the existence of the ridge ($\epsilon_r = 3$).

the operating bandwidth which is affecting the simulation results, especially for high dielectric constant filling. Different standard substrates are used to obtain the response. Figure 6.10 shows the scattering parameters of the validation setup with three different Rogers materials RO3003, RO5880 and RO5880 LZ, where the relative permittivities are 3, 2.2 and 1.96 respectively. Applying the proposed algorithm, the dispersion relation for the dielectric filled guide is obtained. The second step is to get the slope of each curve compared to the air filled case, which is the square root of the effective permittivity. The dispersion relations for the RGW filled with dielectric in these different cases are shown in Figure 6.11 compared to the value of $\beta_{air}\sqrt{\epsilon_{eff}}$. The values of the effective permittivities are obtained to be 2.34, 1.82 and 1.66 respectively. Using the curve that relates the effective to relative permittivities in Figure 6.5, the relative permittivities extracted are 2.97, 2.19 and 1.93. The error in extracting the relative permittivity values is less than 2% in the previous three cases.

The second validation step is performed experimentally. The TRL calibration performed using customized Through, Short Circuit, and Line is shown in Figure 6.12. This figure indicates two transitions from coax to RGW are connected to a straight ridge gap waveguide, where the upper ground of the RGW is removed to show the structure details. This figure also shows different guide lengths in order to be deployed in the calibration procedure. A sample of RO5880 LZ standard substrate with the required dimensions is placed on top of the ridge. The validation setup is shown in Figure 6.13. In this figure a piece of the material under test is prepared with the gap height exactly and placed above the ridge. The upper ground is also removed to show the testing configuration. The comparison between the scattering parameter measured and simulated for this setup is illustrated in Figure 6.14. The previous comparison shows a very good agreement between the simulated and the measured scattering parameters; then these parameters are utilized to obtain the effective permittivity through the proposed algorithm in Section 6.1.2. The extracted effective permittivity is 1.65, and the corresponding relative permittivity is 1.92., while the sample has a dielectric constant of 1.96. The percentage error in measuring the relative permittivity, in this case, is 2%. It is important to mention that the methodology used to determine the dielectric constant of these standard substrates is entitled the strip line test [104] as referred to in the data sheet of this specification substrate.

6.1.7 The Relative Permittivity Extraction in Textile Materials

The same procedure was applied in the case of two different textile materials. The selected SUT are based on the suitability of using them at high frequencies. After literature review and dealing with multiple samples in our experiment, it is observed that prior knowledge about material composition is a valuable parameter. There are

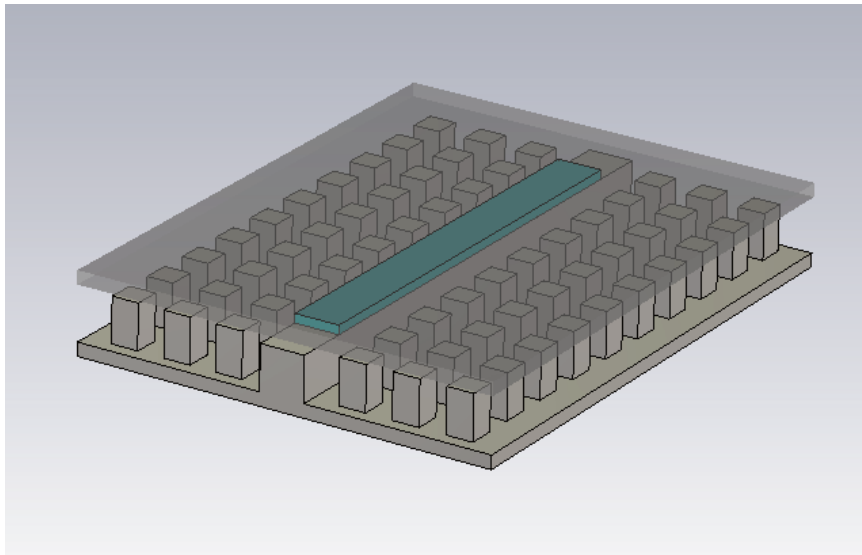


Figure 6.9: The setup validation model.

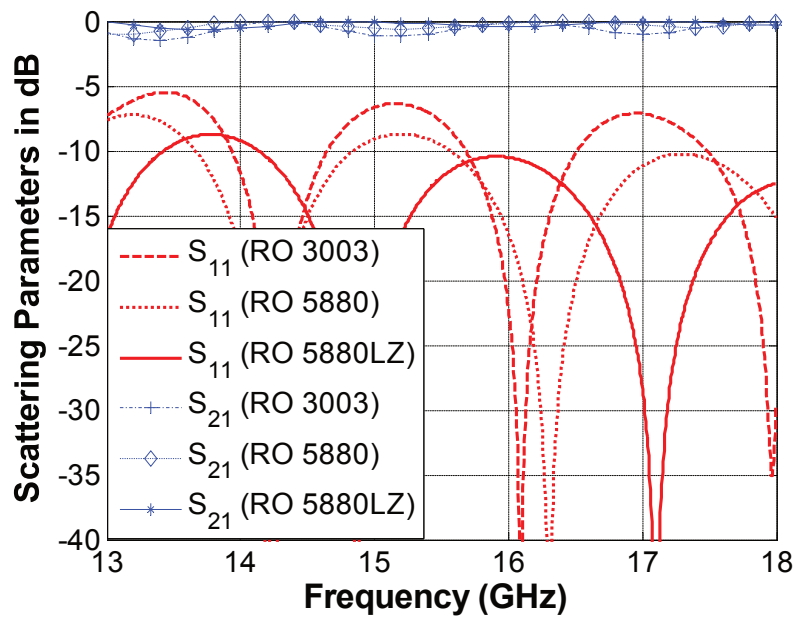


Figure 6.10: The scattering parameters of dielectric filled RGW between two air filled RGWs.

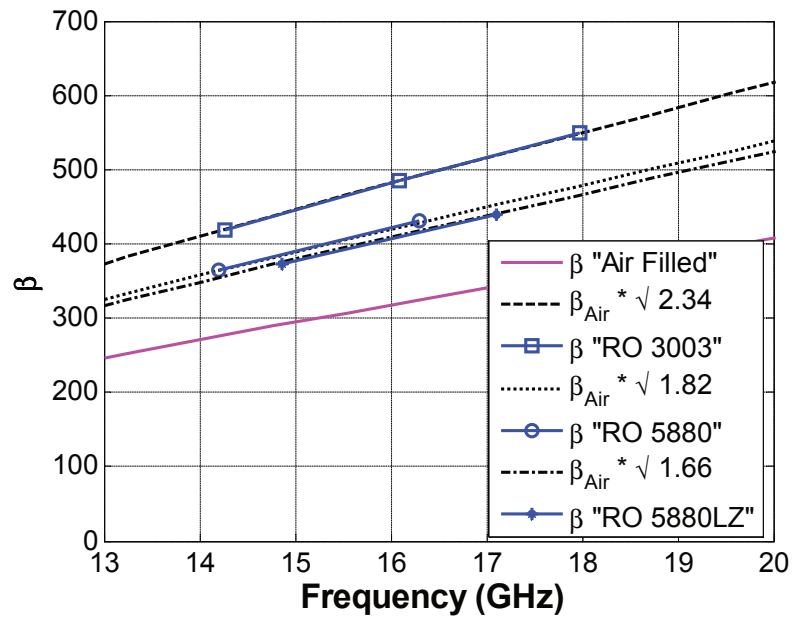


Figure 6.11: The extracted dispersion relation of three standard substrates.

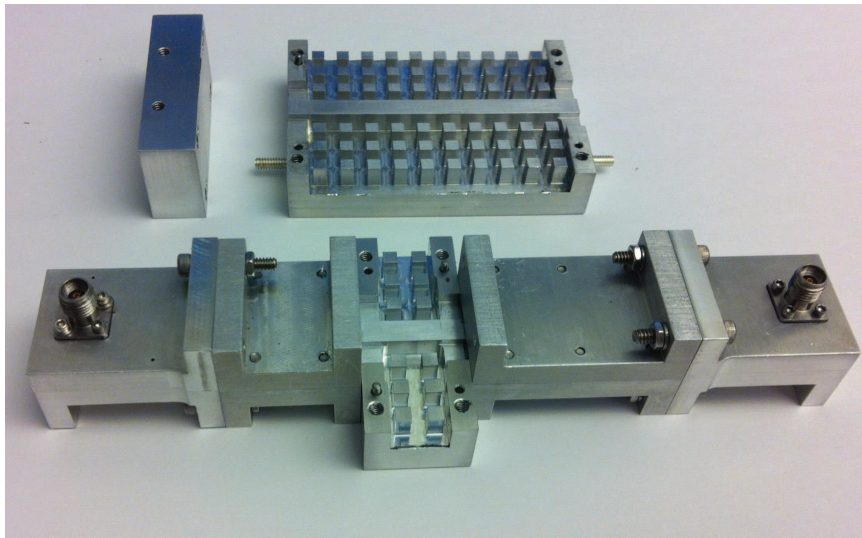


Figure 6.12: The customized TRL calibration kit parts.

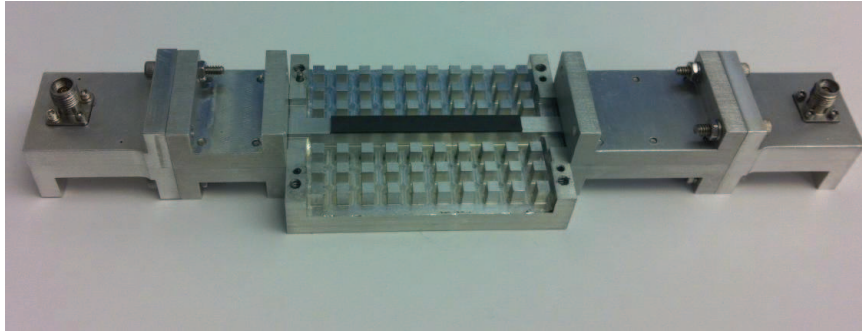


Figure 6.13: The measurement setup with a sample under the test of RO5880 LZ substrate.

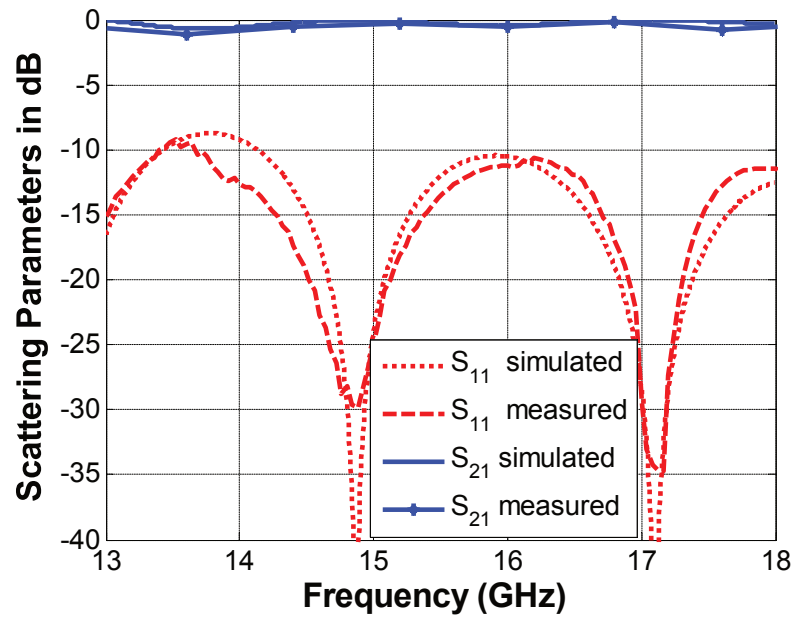


Figure 6.14: Comparison between the simulated & measured scattering parameters of a partially filled RGW with 5880LZ substrate.

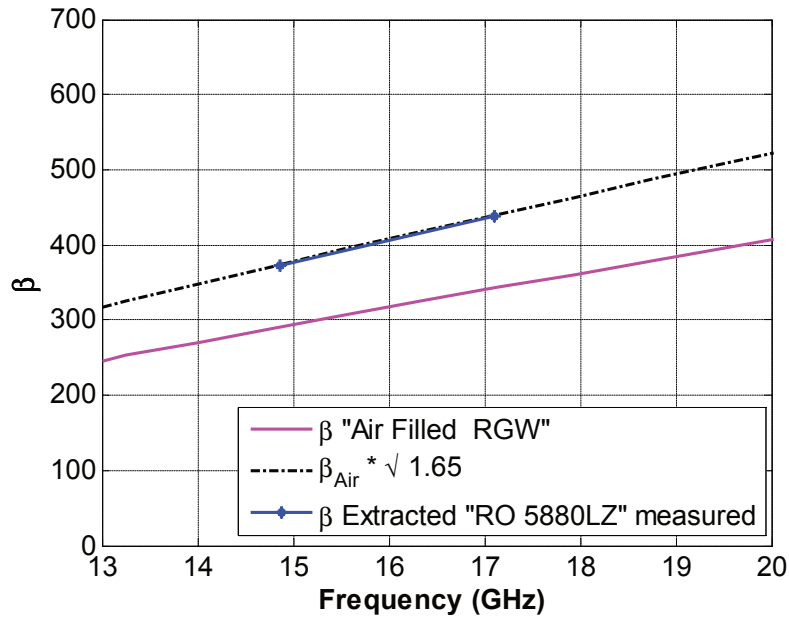


Figure 6.15: The dispersion relation extracted through the measurement setup.

a variety of textile materials available in the local market, but not all materials are suitable for microwave application due to their individual electrical properties.

The conventionally used textile materials for wearable applications in literature have a different composition such as 100 % cotton materials, 100 % polyester materials, 65 % cotton and 35 % polyester material, and 65 % polyester and 35 % cotton materials [105–108]. It is observed that the materials with 100 % polyester are not suitable for antenna designing due to their extra softness and difficult to measure the required thickness in an accurate way. In the RGW, the gap between the ridge and the upper plate is a critical parameter. If the SUT does not have exactly the proper thickness, the overall system performance is deteriorated. The SUT thickness should be accurately measured by some specific tools to ensure the required dimensions suitable for the measurement procedure. The selected materials are shown in Figure 6.16 where Sample 1 has a characteristic composition with 65 % cotton and 35 % polyester while Sample 2 contains 100 % cotton. Both pieces are to be cut exactly to the width of the ridge. They are placed inside the gap above the ridge.

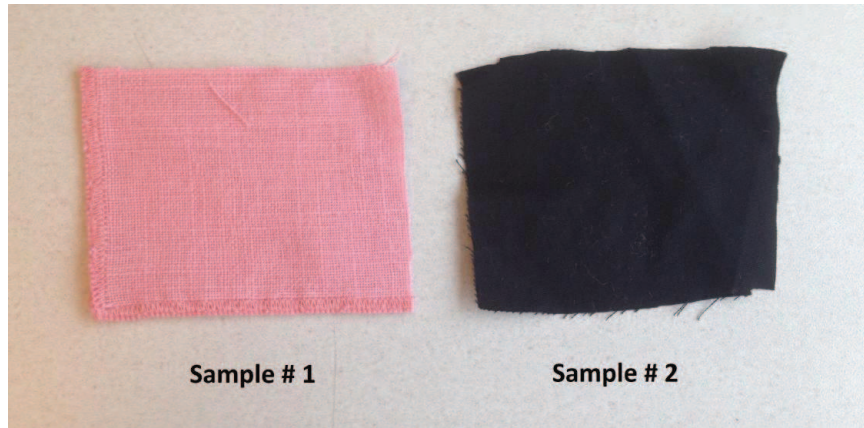


Figure 6.16: The textile samples under test.

The two samples were prepared with the required dimensions to be placed correctly inside the gap of the RGW. Figure 6.17 shows the measurement setup with the two samples. Sample 1 has a pink color, while the black colored material is sample 2. The upper ground of the ridge is removed to show the sample placement. For textile materials of thickness less than 1 mm, stacked layers of the material can be used to construct the required sample. The setup in Figure 6.18 is deployed to measure the scattering parameters of the loaded RGW with the textile materials. After applying the TRL calibration, the scattering parameters of the two samples are shown in Figure 6.19, and the extracted dispersion relations for both samples are shown in Figure 6.20, where the effective permittivities for Sample 1 and 2 are 1.33 and 1.425 respectively. The corresponding values of the relative permittivities are 1.38 and 1.53, which are indicated in Figure 6.21. The same algorithm was applied three times, and the extracted results have a neglected deviation of the nominal values, about 0.1%. This highlighted the repeatability of the proposed algorithm. Another validation step was performed by comparing these results with another extraction procedure based on the resonance technique. The first sample was measured through resonance technique in [109]. The estimated dielectric constant is 1.41, which is very close to the value extracted through the proposed algorithm.

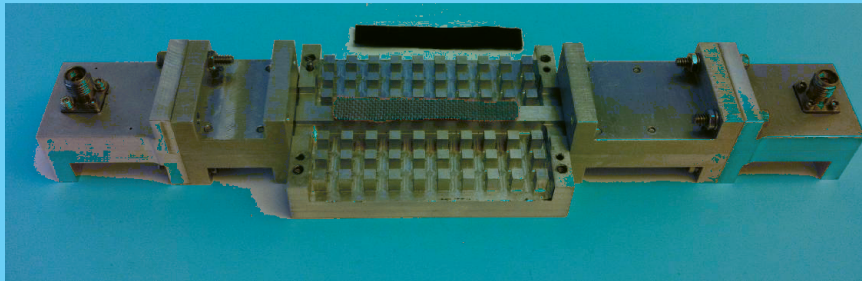


Figure 6.17: The measurement setup with the textile samples.

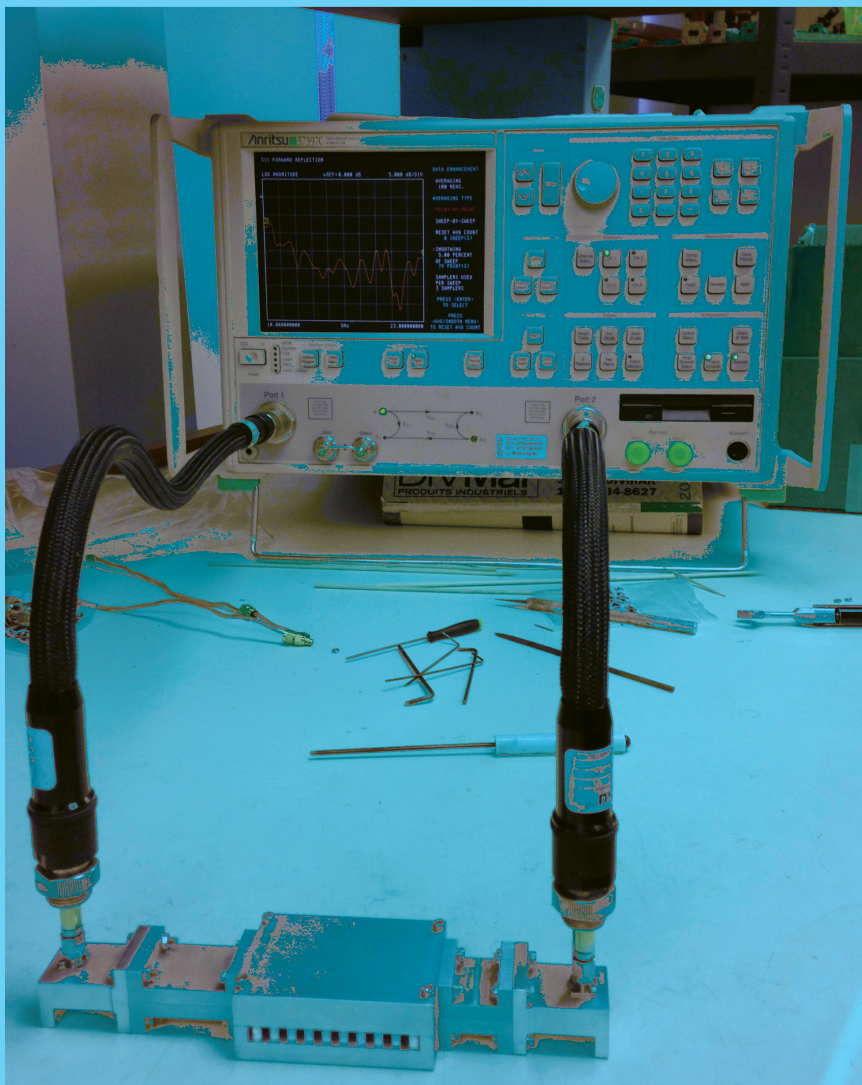


Figure 6.18: The measurement setup of the textile material.

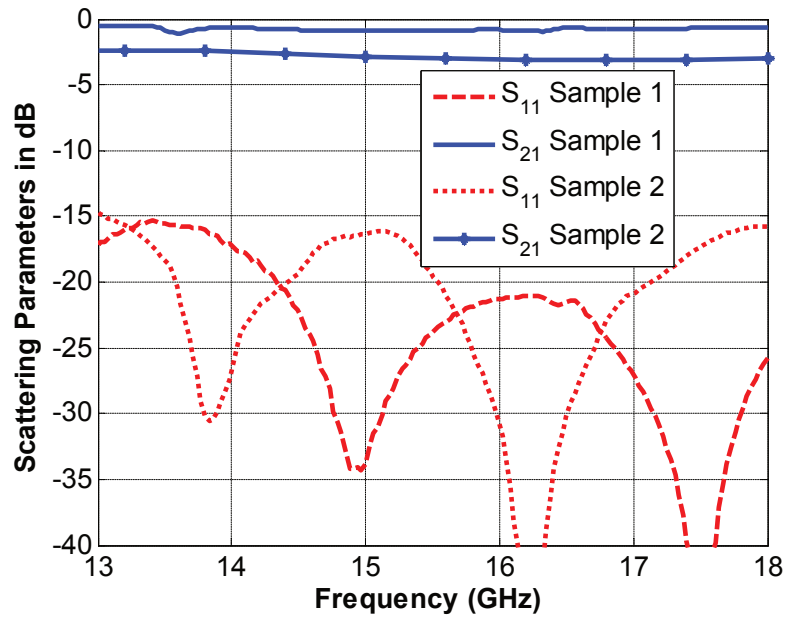


Figure 6.19: The scattering parameters of a partially filled RGW with two different samples of textile materials.

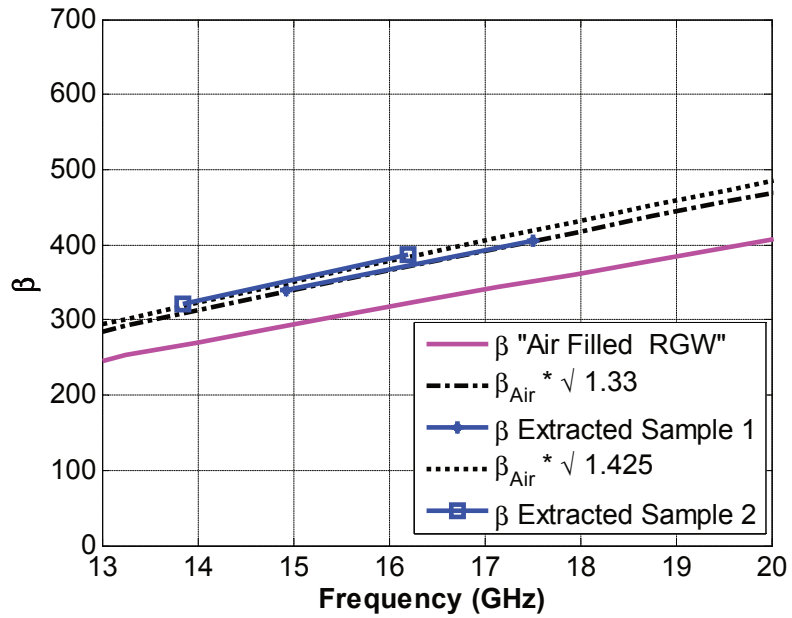


Figure 6.20: The dispersion relation extracted through the measurement setup for two textile material samples.

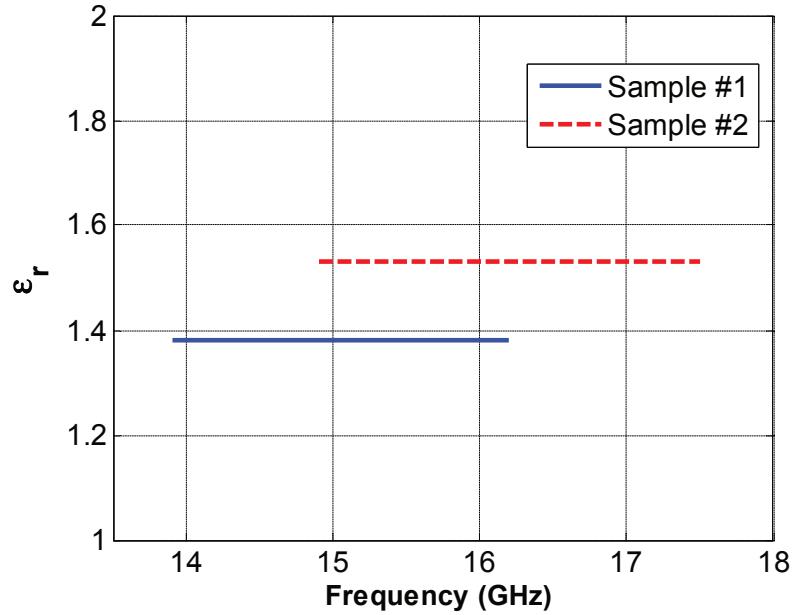


Figure 6.21: The extracted relative permittivities of the textile material samples Vs frequency.

6.1.8 The Uncertainty in the Measured Results

The proposed algorithm is validated with a sample of a well-known dielectric constant. In addition, the measured results are compared with the values obtained by a resonance method, and they are in excellent agreement. However, some points may contribute to some measurement errors. These sources of errors have different effects on the extracted relative permittivity. It can be classified into three categories: The sample electrical properties effect, the sample mechanical properties effect, and the instruments imperfection.

Measurement error due to losses and frequency dependency

As mentioned before, the losses and the frequency dependency lead to an expected error in the measured dielectric constant as shown in Figure 6.3. The max expected error due to both losses and frequency dependency is about 1% as long as the material conductivity is below 0.1 S/m. It is important to mention that these errors

are calculated based on a simple model of the frequency dependency in Equation 6.13. More complicated and accurate models can be considered to generalize the proposed methodology, however, in the application in focus, the results are very close to the results provided by narrow band algorithms based on resonance. This gives an indication of the insignificant effect of the frequency dependence on the extracted results.

Sample Mechanical properties effect

The dimensions of the sample under test has an effect on the extracted value. The sample height effect is studied in section IV, where the dielectric constant percentage error is about 3 % if the sample thickness is reduced by 10 %. The width of the sample under test will have a small contribution as the propagating mode inside the RGW is a quasi-TEM mode with the electric field is confined within the ridge width. It is important to make sure that the sample width is equal to or slightly greater than the ridge width. If it is greater than the required width, some of the fringing fields will be affected by the existence of the dielectric material. This has an insignificant effect on the effective permittivity.

Instruments imperfection

One of the major advantages of the introduced method is the immunity of the instruments imperfections. The presented algorithm depends only on the magnitude of the steady state scattering parameters. There is no need for an accurate time domain measurement or even the scattering parameter phase. The proposed algorithm is able to extract the relative permittivity from the dispersion relation slope. This slope is obtained through the peaks and minima of the scattering parameters magnitude. Most of the errors due to the instruments and the calibration affect the phase of the S-parameters, which is not considered in the presented technique.

6.2 Leaky-wave Antenna Array Fed by RGW

Antennas excited by ridge gap waveguides were firstly proposed in 2012 [110]. The previously mentioned work proposed feeding a two-slot antenna by a ridge gap waveguide T junction. In [23] an RWG structure with profiled ridge to increase the width of the ridge and to act as an H-plane sectoral horn was used to excite an array of long slots with uniform fields. To reduce the grating lobes, the slots were split and separated by a half wavelength after introducing 180° phase shift to one-half of the structure [111]. Here a similar slot arrangement is used, but without the need for a phase shifter.

6.2.1 Magic Tee Design

In order to eliminate the necessity of a frequency varying phase shifter as in [111], a four port magic tee is designed to operate in the Ku-band. The co-linear arms are fed from the H-plane port to achieve the power splitting with out of phase field output or they are supplied from the E-plane port to achieve the power splitting with in-phase fields in both ports. The matching is accomplished by placing a hemisphere in the ground facing of the H-plane port. Figure 6.22(a) illustrates the cross sections of the magic tee circuit with the matching hemisphere while Figure 6.22 (b) shows the 3D structure of the same component. The response of this magic tee circuit is provided in Figure 6.23, which indicates that the magic tee has a matching level of -15 dB for both ports over more than 80% of the Ku-band.

6.2.2 Ridge Gap Waveguide Analysis

As mentioned before, the magic tee circuit was used to feed the RGW to achieve 180° phase shift between the two halves of the RGW. The RGW is designed with cell size to operate in the Ku-band. It can be seen in Figure 6.24 that the unit cell with

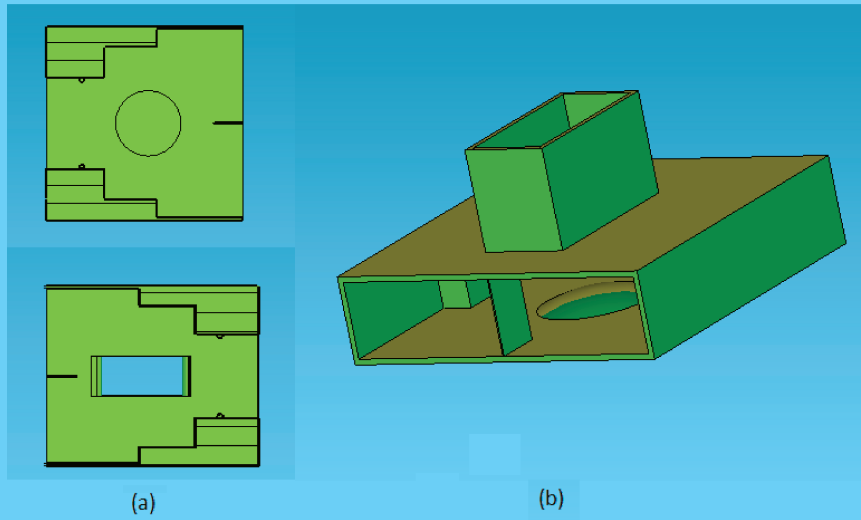


Figure 6.22: The structure of the magic tee component.

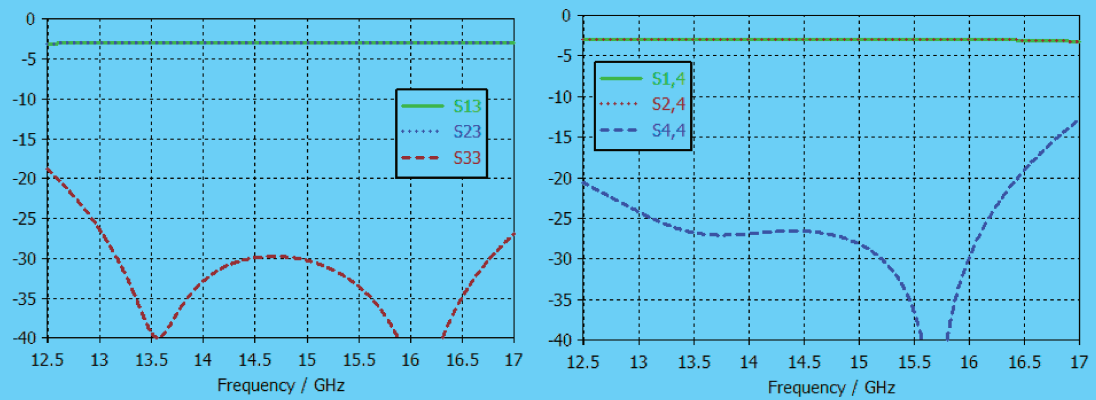


Figure 6.23: The magic tee scattering parameters.

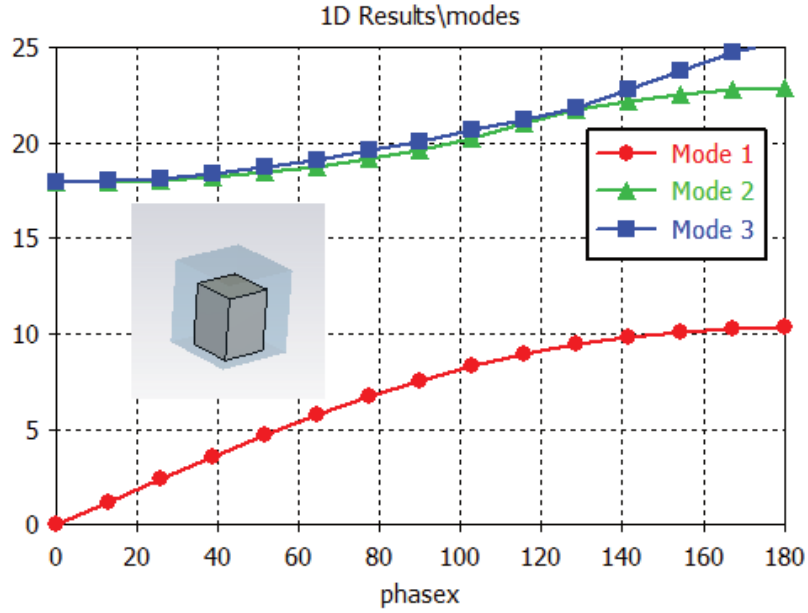


Figure 6.24: The unit cell dispersion diagram.

the dimensions provided in Table 6.2 covers the whole Ku-band. The RGW connected to the magic tee circuit as shown in Figure 6.25(a) where the upper ground is made invisible to illustrate the internal details of the structure, while the field distribution is shown in the same figure part (b). The field distribution plotted in this figure indicates that the phase difference between both halves of the RGW is 180° . Placing the slot array alternating between the two parts of the RGW with half wavelength separation will keep all slots in phase. This feeding mechanism provides wider band compared to similar transitions presented in the literature [112].

Table 6.2: The dimensions of the unit cell design

The Parameter	The Value (inch)	The Parameter	The Value (inch)
Cell width	0.25	Gap Height	0.07
Nail Width	0.15	Nail Height	0.2

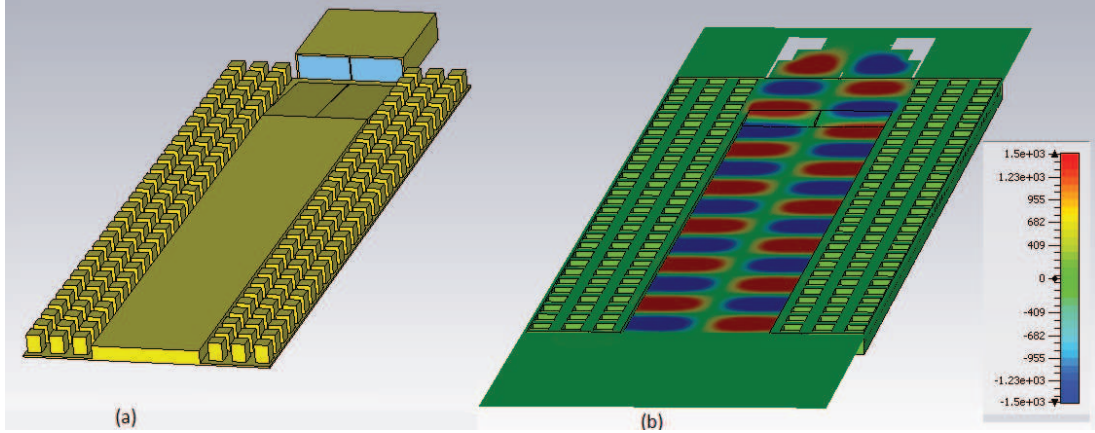


Figure 6.25: The RGW fed by the magic tee (a) 3D structure (b) The field distribution.

6.2.3 The Leaky Wave Slot Array

All slots have the same phase as described in the former section. Moreover, the field distribution in the line is almost uniform due to the RGW propagating mode. The slot widths are gradually increased to compensate the decrease in the amplitude caused by each slot radiation. Increasing the slot width in a successive way provides equal magnitude for all the array elements. Figure 6.26(a) shows the complete structure with the slots placed in the upper ground. The radiation pattern of this leaky-wave slot array is plotted in Figure 6.27.

The return loss of the complete structure, as well as the Gain Vs frequency, is shown in Figure 6.28. To illustrate the frequency scanning of this structure, the radiation patterns of the array are plotted in the Figures 6.29 through 6.32. It is worth mentioning that the worst matching occurs in the case of the broadside beam at a frequency of 13.8 GHz. It is always hard to achieve the matching at the broadside operation. The return loss and the gain plotted in this design indicate that the least matching and the smallest gain occur in the broadside case.

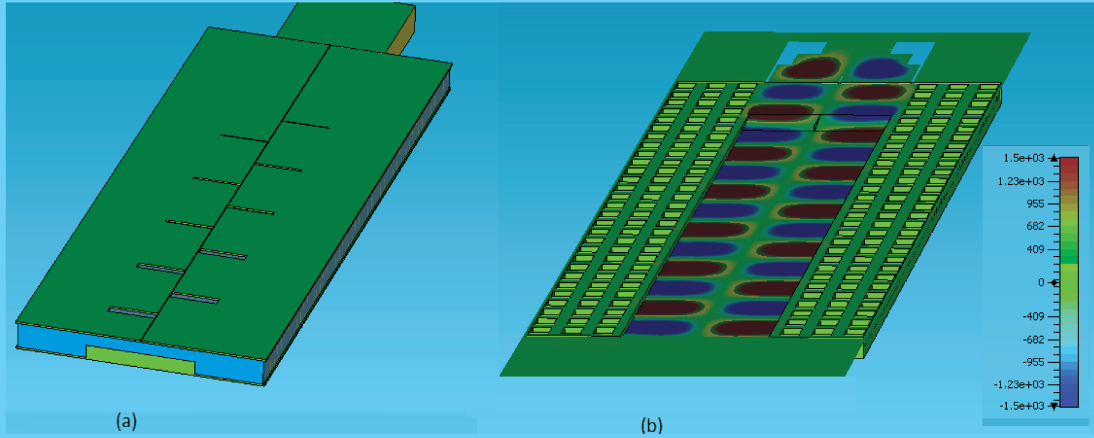


Figure 6.26: The leaky wave slot (a)3D structure (b)Field distribution.

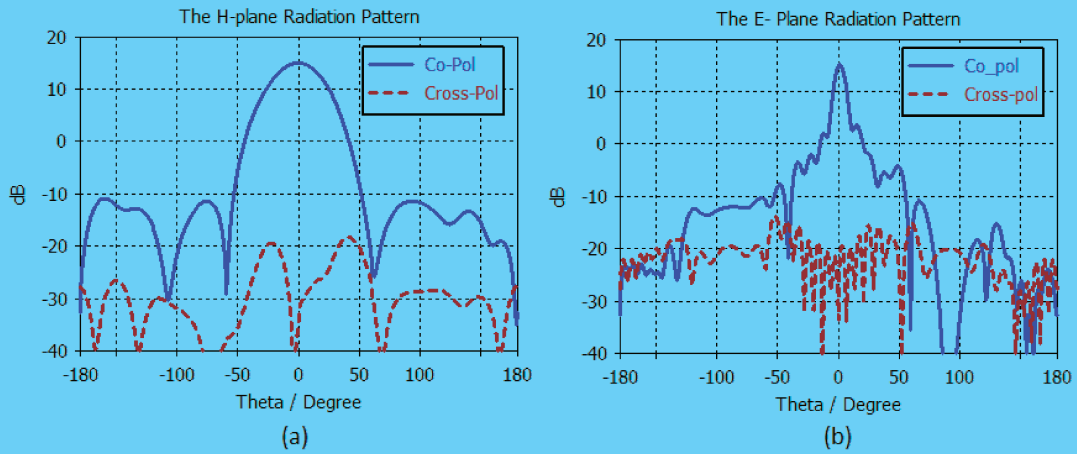


Figure 6.27: The radiation pattern for the whole leaky-wave slot array.

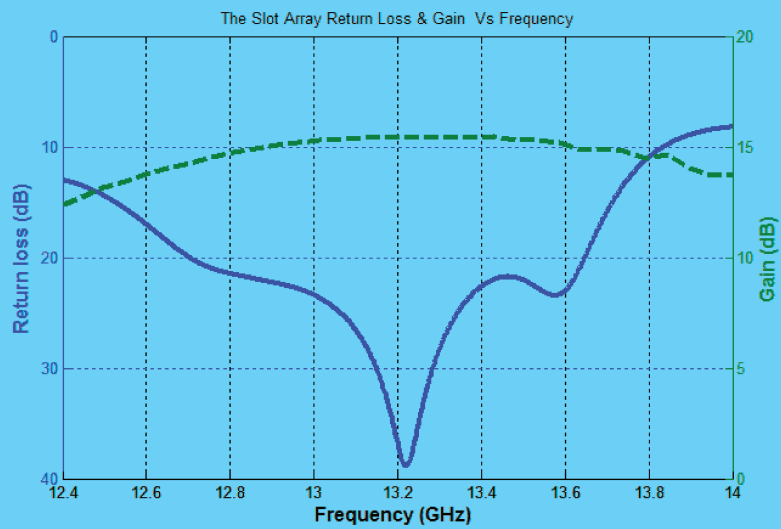


Figure 6.28: The return loss and the array gain vs frequency.

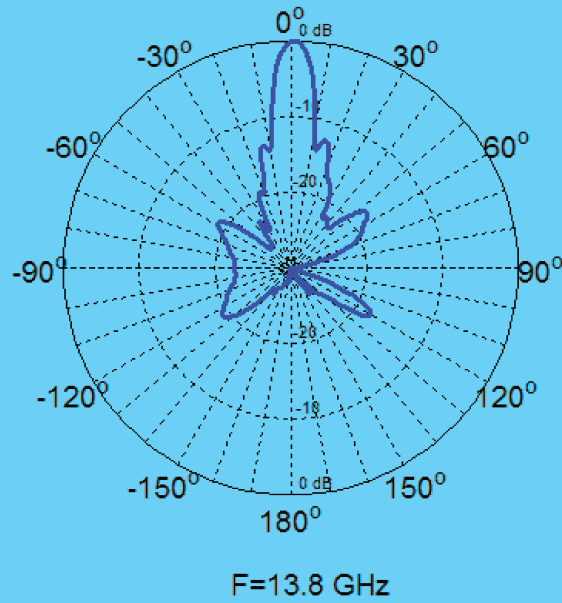


Figure 6.29: The radiation pattern in E-plane.

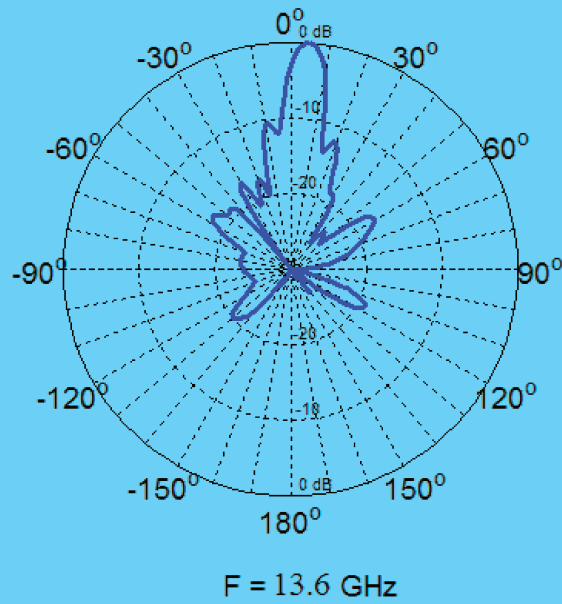
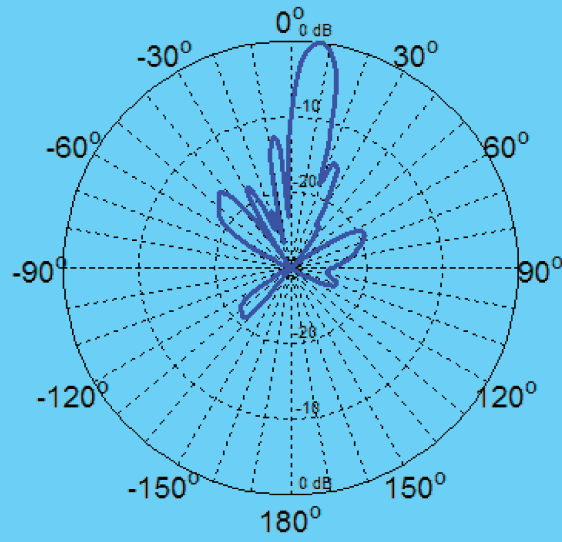
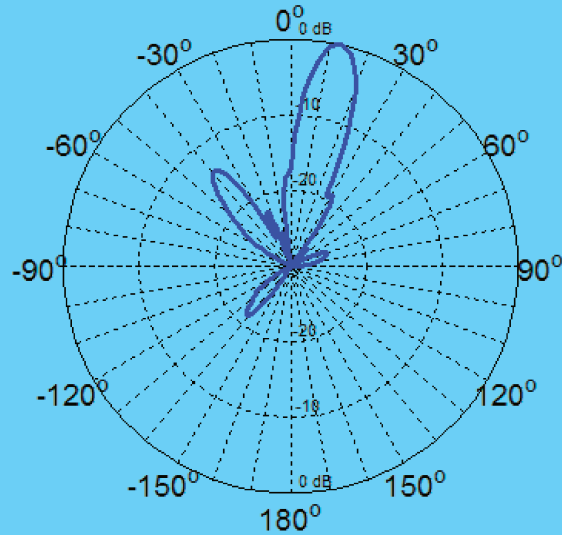


Figure 6.30: The radiation pattern in E-plane.



F = 13.4 GHz

Figure 6.31: The radiation pattern in E-plane.



F = 13.2 GHz

Figure 6.32: The radiation pattern in E-plane.

Chapter 7

Conclusion and Future Work

Recently, a new guiding structure referred to as the ridge gap waveguide (RWG) was developed. The RWG has interesting characteristics that make it suitable for millimeter wave applications. However, the RWG is not one of the standard guiding structures that can be measured directly with the standard connectors and equipment. Therefore, transitions between the RWG and other guiding structures must be developed. In addition, the conventional components that are developed for other technologies must be developed based on the RWG technologies. This thesis has been dealing with some of these requirements.

The first part of this work has proposed transitions showing promising behaviors. Two different transitions have been presented: A coaxial to RGW transition and a microstrip line to RGW transitions. These transitions enable the establishment of measurement setups of devices based on RGW technology. Then, different analysis techniques were introduced to give a more accurate estimation of the RGW bandwidth and a deeper understanding of the meaning of this bandwidth. In this work, a new practical methodology for the dispersion relation extraction has been introduced, which depends only on the two-port scattering parameter measurements of the embedded device under test (DUT). The difference between the unit cell possible

bandwidth and the realized bandwidth has been highlighted to introduce more accurate parameters for different cell comparisons. Moreover, a novel structure of the RGW unit cells has been developed, which is called the grounded printed cone unit cell that is easily fabricated providing wider operating bandwidth. In addition, a new type of the RGW based on using two different gap heights has been introduced.

Based on the designed transitions and the accurate evaluation of the RGW bandwidth, various microwave components have been designed. Three different microwave components have been developed. The first component is a wideband power divider. The introduced power divider has covered 50 % of the X-band, all the Ku-band and 25 % of the K band, which is based on two Chebyshev matching transformers. The second passive component is an RGW hybrid coupler, where the core mathematical formulations, as well as the empirical expressions, have been deployed in the design procedure. The final design has been fabricated and tested through a special test setup for the RGW components with an excellent agreement with the simulation.

A systematic approach to analyzing and design circulators has been developed. The results, based on this approach have been compared with the analytical model that relies on assuming ideal boundary conditions. Two circulator examples have been presented at two different frequencies for mobile and radar applications. The introduced circulators provided a 40% operating bandwidth with a matching and isolation levels of 15 dB.

The final part is related to the applications of the introduced transitions and components. Two different applications have been presented based on RGW technology. The first one is the development of a wideband measurement set up for the relative permittivity. The existence of a single quasi-TEM mode inside the RGW leads to having a simple relation between the dispersion relations of the air filled RGW and the partially filled one. The algorithm has been validated with some standard substrates and has been utilized to measure different textile materials. The second

application is a novel idea of building a leaky-wave slot array fed by RGW structure. The feeding structure enables the separation between the successive split slots by a half wavelength to eliminate the radiation pattern grating lobes without the need of a phase shifter that limits the operating bandwidth. Moreover, more slots in the structure will provide higher gain and a narrower beam in the E-plane.

This work can be extended by exploring other passive devices based on the ridge gap waveguide technology such as the loop couplers and magic tees. Moreover, many nonreciprocal devices have to be designed based on the RGW like the phase shifters and duplexers. These devices enable the deployment of the RGW in future communication systems. In addition, the active components can be a very useful extension of this work. Hence, the full high frequency link can be implemented through the RGW technology, which is the final goal of this work.

Bibliography

- [1] T. K. Sarkar, *Smart Antennas*, 1st ed. New Jersey: Jone Wiley Sons, 2003.
- [2] T. K. Sarkar, J. M. Arthur, M. S. Palma, and D. L. Sengupta, *History of Wireless*, 2nd ed. New Jersey: Jone Wiley Sons, 2006.
- [3] D. Pozar, *Microwave Engineering*, 3rd ed. New York: Jone Wiley Sons, 2004.
- [4] P.-S. Kildal, "Definition of artificially soft and hard surfaces for electromagnetic waves," *Electronics Letters*, vol. 24, no. 3, pp. 168–170, Feb 1988.
- [5] P.-S. Kildal and A. Kishk, "EM modeling of surfaces with stop or go characteristics artificial magnetic conductors and soft and hard surfaces," *ACES Journal Paper*, vol. 18, no. 1, pp. 32–40, March 2003.
- [6] P.-S. Kildal, "Artificially soft and hard surfaces in electromagnetics and their application to antenna design," in *the 23rd European Microwave Conference*, Sept 1993, pp. 30–33.
- [7] Y. Rahmat-Samii and H. Mosallaei, "Electromagnetic band-gap structures: classification, characterization, and applications," in *the Eleventh International Conference on Antennas and Propagation*, vol. 2, 2001, pp. 560–564.
- [8] P.-S. Kildal, E. Alfonso, A. Valero-Nogueira, and E. Rajo-Iglesias, "Local metamaterial-based waveguides in gaps between parallel metal plates," *Antennas and Wireless Propagation Letters, IEEE*, vol. 8, pp. 84–87, 2009.

- [9] E. Rajo-Iglesias, A. Zaman, and P.-S. Kildal, "Parallel plate cavity mode suppression in microstrip circuit packages using a lid of nails," *IEEE Microwave and Wireless Components Letters*, vol. 20, no. 1, pp. 31–33, Jan 2010.
- [10] P.-S. Kildal, A. Zaman, E. Rajo-Iglesias, E. Alfonso, and A. Valero-Nogueira, "Design and experimental verification of ridge gap waveguide in bed of nails for parallel plate mode suppression," *IET Microwaves and Antennas Propagation*, vol. 5, no. 3, pp. 262–270, Feb 2011.
- [11] P.-S. Kildal, E. Rajo-Iglesias, E. Alfonso, A. Valero, and A. Zaman, "Wideband, lowloss, low-cost, quasi-TEM metamaterial-based local waveguides in air gaps between parallel metal plates," in *International Conference on Electromagnetics in Advanced Applications, ICEAA.*, Sept 2009, pp. 588–591.
- [12] A. Zaman, E. Rajo-Iglesias, E. Alfonso, and P.-S. Kildal, "Design of transition from coaxial line to ridge gap waveguide," in *IEEE Antennas and Propagation Society International Symposium, APSURSI*, June 2009, pp. 1–4.
- [13] A. Zaman, P.-S. Kildal, M. Ferndahl, and A. Kishk, "Validation of ridge gap waveguide performance using in-house TRL calibration kit," in *Proceedings of the Fourth European Conference on Antennas and Propagation (EuCAP)*, April 2010, pp. 1–4.
- [14] M. Sorkherizi, A. Khaleghi, and P.-S. Kildal, "Direct-coupled cavity filter in ridge gap waveguide," *IEEE Transactions on Components, Packaging and Manufacturing Technology*, vol. 4, no. 3, pp. 490–495, March 2014.
- [15] E. Alfonso, M. Baquero, P. Kildal, A. Valero-Nogueira, E. Rajo-Iglesias, and J. Herranz, "Design of microwave circuits in ridge-gap waveguide technology," in *IEEE MTT-S International Microwave Symposium Digest (MTT)*, May 2010, pp. 1–1.

- [16] A. Zaman, P.-S. Kildal, M. Ferndahl, and A. Kishk, "Design of a coplanar waveguide to ridge gap waveguide transition via capacitive coupling," in *6th European Conference on Antennas and Propagation (EUCAP)*, March 2012, pp. 3524–3528.
- [17] A. A. Kishk, A. U. Zaman, and P.-S. Kildal, "Numerical prepackaging with PMC lid efficient and simple design procedure for microstrip circuits including the packaging," *ACES Journal Paper*, vol. 27, no. 5, May 2012.
- [18] Y. Tikhov, I. S. Song, J. H. Won, and J. P. Kim, "Compact broadband transition from double-ridge waveguide to coaxial line," *Electronics Letters*, vol. 39, no. 6, pp. 530–532, March 2003.
- [19] M. Bialkowski, "Analysis of a coaxial-to-waveguide adaptor including a descended probe and a tuning post," *IEEE Transactions on Microwave Theory and Techniques*, vol. 43, no. 2, pp. 344–349, Feb 1995.
- [20] N. Rui-Xing, L. En, G. Gao-Feng, and W. Yi, "Simulation and design of 18 to 40 GHz ridge waveguide to coaxial transition," in *IEEE International Conference on Microwave Technology Computational Electromagnetics (ICMTCE)*, May 2011, pp. 183–185.
- [21] S. B. Cohn, "Properties of ridge waveguide," *Proceedings of the IRE*, vol. 35, no. 8, pp. 783–788, Aug 1947.
- [22] J. Whinnery and H. Jamieson, "Equivalent circuits for discontinuities in transmission lines," *Proceedings of the IRE*, vol. 32, no. 2, pp. 98–114, Feb 1944.
- [23] M. Al Sharkawy and A. Kishk, "Long slots array antenna based on ridge gap waveguide technology," *IEEE Transactions on Antennas and Propagation*, vol. 62, no. 10, pp. 5399–5403, Oct 2014.

- [24] M. AlSharkawy and A. A. Kishk, "Wideband beam-scanning circularly polarized inclined slots using ridge gap waveguide," *IEEE Antennas and Wireless Propagation Letters*, vol. 13, pp. 1187–1190, 2014.
- [25] S. Shams and A. Kishk, "Ridge gap waveguide to microstrip line transition with perforated substrate," in *Radio Science Meeting (Joint with AP-S Symposium), USNC-URSI*, July 2014, pp. 215–215.
- [26] A. Zaman, T. Vukusic, M. Alexanderson, and P.-S. Kildal, "Design of a simple transition from microstrip to ridge gap waveguide suited for MMIC and antenna integration," *IEEE Antennas and Wireless Propagation Letters*, vol. 12, pp. 1558–1561, 2013.
- [27] B. Molaei and A. Khaleghi, "A novel wideband microstrip line to ridge gap waveguide transition using defected ground slot," *IEEE Microwave and Wireless Components Letters*, vol. 25, no. 2, pp. 91–93, Feb 2015.
- [28] A. Zaman and P.-S. Kildal, "Packaging of MMIC by using gap waveguide and design of a microstrip to ridge gap waveguide transition," in *Asia-Pacific Microwave Conference Proceedings (APMC)*, Nov 2013, pp. 10–12.
- [29] S. Shams and A. Kishk, "Double cone ultra wideband unit cell in ridge gap waveguides," in *IEEE Antennas and Propagation Society International Symposium (APSURSI)*, July 2014, pp. 1768–1769.
- [30] Y. Li and K.-M. Luk, "Wideband perforated dense dielectric patch antenna array for millimeter-wave applications," *IEEE Transactions on Antennas and Propagation*, vol. 63, no. 8, pp. 3780–3786, Aug 2015.
- [31] A. Zaman, V. Vassilev, P.-S. Kildal, and A. Kishk, "Increasing parallel plate stop-band in gap waveguides using inverted pyramid-shaped nails for slot array

- application above 60 GHz,” in *Antennas and Propagation (EUCAP), Proceedings of the 5th European Conference on*, April 2011, pp. 2254–2257.
- [32] A. Polemi and S. Maci, “Closed form expressions for the modal dispersion equations and for the characteristic impedance of a metamaterial-based gap waveguide,” *IET Microwaves, Antennas Propagation*, vol. 4, no. 8, pp. 1073–1080, Aug 2010.
- [33] M. Silveirinha, C. Fernandes, and J. Costa, “Electromagnetic characterization of textured surfaces formed by metallic pins,” *IEEE Transactions on Antennas and Propagation*, vol. 56, no. 2, pp. 405–415, Feb 2008.
- [34] M. Bosiljevac, A. Polemi, S. Maci, and Z. Sipus, “Analytic approach to the analysis of ridge and groove gap waveguides - comparison of two methods,” in *Proceedings of the 5th European Conference on Antennas and Propagation (EUCAP)*, April 2011, pp. 1886–1889.
- [35] W. Gwarek and M. Celuch-Marcysiak, “A generalized approach to wide-band s-parameter extraction from FDTD simulations applicable to evanescent modes in inhomogeneous guides,” in *IEEE MTT-S International Microwave Symposium Digest*, vol. 2, May 2001, pp. 885–888.
- [36] W. Gwarek and M. Celuch Marcysiak, “Wide-band s-parameter extraction from FDTD simulations for propagating and evanescent modes in inhomogeneous guides,” *IEEE Transactions on Microwave Theory and Techniques*, vol. 51, no. 8, pp. 1920–1928, Aug 2003.
- [37] R. E. Collin, *Foundations For Microwave Engineering*, 2nd ed. New York: McGraw-Hill, 1992.
- [38] C. Caloz and T. Itoh, *Electromagnetic metamaterial: transmission line theory and microwave applications*, 3rd ed. New York: John Willy Sons, 2005.

- [39] A. Grbic and G. Eleftheriades, “Periodic analysis of a 2-D negative refractive index transmission line structure,” *IEEE Transactions on Antennas and Propagation*, vol. 51, no. 10, pp. 2604–2611, Oct 2003.
- [40] C. Caloz and T. Itoh, “Positive/negative refractive index anisotropic 2-D metamaterials,” *IEEE Microwave and Wireless Components Letters*, vol. 13, no. 12, pp. 547–549, Dec 2003.
- [41] D. Hirst and R. Hogg, “The design of precision standing-wave indicators for measurements in waveguides,” *Journal of the Institution of Electrical Engineers - Part IIIA: Radiocommunication*, vol. 94, no. 14, pp. 589–595, March 1947.
- [42] P. J. Allen, “An automatic standing wave indicator,” *Electrical Engineering*, vol. 67, no. 11, pp. 1082–1082, Nov 1948.
- [43] R. Medhurst and S. Pool, “Correction factors for slotted measuring lines at very high frequencies,” *Proceedings of the IEE - Part III: Radio and Communication Engineering*, vol. 97, no. 48, pp. 223–230, July 1950.
- [44] E. Alfonso, P.-S. Kildal, A. Valero-Nogueira, and M. Baquero, “Study of the characteristic impedance of a ridge gap waveguide,” in *IEEE Antennas and Propagation Society International Symposium, APSURSI*, June 2009, pp. 1–4.
- [45] E. Alfonso, M. Baquero, A. Valero-Nogueira, J. Herranz, and P.-S. Kildal, “Power divider in ridge gap waveguide technology,” in *Proceedings of the Fourth European Conference on Antennas and Propagation (EuCAP)*, April 2010, pp. 1–4.
- [46] A. Berenguer, M. Baquero-Escudero, D. Sanchez-Escuderos, and F. Vico, “Rigorous method for calculating gap waveguides impedance using transmission line theory,” in *the 8th European Conference on Antennas and Propagation (EuCAP)*, April 2014, pp. 2508–2512.

- [47] H. Raza, J. Yang, P.-S. Kildal, and E. Alfonso, “Resemblance between gap waveguides and hollow waveguides,” *IET Microwaves and Antennas Propagation*, vol. 7, no. 15, pp. 1221–1227, December 2013.
- [48] M. Sorkherizi and A. Kishk, “Lowloss planar bandpass filters for millimeter-wave application,” in *IEEE MTT-S International Microwave Symposium (IMS)*, May 2015, pp. 1–4.
- [49] J. Rigden and S. Macmillan, *Encyclopedia of Physics*. Simon & Schuster, 1996.
- [50] A. D. MacDonald, *Microwave Breakdown in Gases*. New York: John Wiley and Sons Inc, 1966.
- [51] J. Helszajn, *Ridge waveguides and passive microwave components, IEE Electromagnetic Waves Series 49*, 2000th ed. Bodmin, Cornwall, England: MPG books Limited, 1966.
- [52] J. Pyle, “The cutoff wavelength of the TE₁₀ mode in ridged rectangular waveguide of any aspect ratio,” *IEEE Transactions on Microwave Theory and Techniques*, vol. 14, no. 4, pp. 175–183, Apr 1966.
- [53] Z. Talepour, S. Esmaili, and A. Khaleghi, “Ridge gap waveguide antenna array using integrated coaxial power divider,” *Loughborough Antennas Propagation Conference (LAPC)*, pp. 1–5, Nov 2015.
- [54] W. A. Tyrrell, “Hybrid circuits,” *Proceedings of the IRE*, pp. 1294–1306, Nov 1947.
- [55] L. Cutrona, “The theory of biconjugate networks,” *Proceedings of the IRE*, pp. 827–832, July 1951.
- [56] H. Riblet, “The short-slot hybrid junction,” *Proceedings of the IRE*, vol. 40, no. 2, pp. 180–184, Feb 1952.

- [57] H. J. Riblet, "A mathematical theory of directional couplers," *Proceedings of the IRE*, vol. 35, no. 11, pp. 1307–1313, Nov 1947.
- [58] S. E. A. R. K. Gupta and W. J. Getsinger, "Impedance-transforming 3-dB 90 hybrids," pp. 1303–1307, Dec 1987.
- [59] S. B. Cohn, "The re-entrant cross section and wide-band 3-dB hybrid couplers," *IEEE Transactions on Microwave Theory and Techniques*, vol. 11, no. 4, pp. 254–258, Jul 1963.
- [60] A. L. T. L. M. F. Boccardi, R. W. Heath and P. Popovski, "Five disruptive technology directions for 5G," *IEEE Communications Magazine*, pp. 74–80, February 2014.
- [61] T. Imai, K. Kitao, N. Tran, N. Omaki, Y. Okumura, M. Sasaki, and W. Yamada, "Development of high frequency band over 6 GHz for 5G mobile communication systems," in *2015 9th European Conference on Antennas and Propagation (EuCAP)*, May 2015, pp. 1–4.
- [62] J. F. Carlson and A. E. Heins, "reflection of an electromagnetic plane wave by an infinite set of plates," *Quart. Appl. Math.*, pp. 313–329, January 1947.
- [63] C. L. Hogan, "The ferromagnetic faraday effect at microwave frequencies and its applications: The microwave gyrator," *The Bell System Technical Journal*, vol. 31, no. 1, pp. 1–31, Jan 1952.
- [64] A. G. Fox, S. E. Miller, and M. T. Weiss, "Behavior and applications of ferrites in the microwave region," *The Bell System Technical Journal*, vol. 34, no. 1, pp. 5–103, Jan 1955.

- [65] B. A. Auld, "The synthesis of symmetrical waveguide circulators," *IRE Transactions on Microwave Theory and Techniques*, vol. 7, no. 2, pp. 238–246, April 1959.
- [66] M. A. Treuhaft, "Network properties of circulators based on the scattering concept," *Proceedings of the IRE*, vol. 44, no. 10, pp. 1394–1402, Oct 1956.
- [67] P. R. Mason, "Analysis of four-port circulators using non-reciprocal phase shifters and directional couplers," *Proceedings of the Institution of Electrical Engineers*, vol. 110, no. 5, pp. 869–880, May 1963.
- [68] G. S. Heller, "Ferrites as microwave circuit elements," *Proceedings of the IRE*, vol. 44, no. 10, pp. 1386–1393, Oct 1956.
- [69] P. J. Allen, "The turnstile circulator," *IRE Transactions on Microwave Theory and Techniques*, vol. 4, no. 4, pp. 223–227, October 1956.
- [70] B. Owen and C. E. Barnes, "The compact turnstile circulator," in *International Microwave Symposium, G-MTT*, May 1970, pp. 388–392.
- [71] H. N. Chait and T. R. Curry, "Y circulator," *Journal of Applied Physics*, vol. 30, no. 4, 1959.
- [72] J. H. S. U. MILANO and L. DAVIS, "A Y-junction strip-line circulator," *IRE Transactions on Microwave Theory and Techniques*, vol. 8, no. 3, pp. 346–351, May 1960.
- [73] J. B. Davies, "An analysis of the m-port symmetrical H-Plane waveguide junction with central ferrite post," *IRE Transactions on Microwave Theory and Techniques*, vol. 10, no. 6, pp. 596–604, November 1962.

- [74] B. A. Auld, "The synthesis of symmetrical waveguide circulators," *IRE Transactions on Microwave Theory and Techniques*, vol. 7, no. 2, pp. 238–246, April 1959.
- [75] H. Bosma, "On stripline Y-circulation at UHF," *IEEE Transactions on Microwave Theory and Techniques*, vol. 12, no. 1, pp. 61–72, Jan 1964.
- [76] B. Hershenov, "X-band microstrip circulator," *Proceedings of the IEEE*, vol. 54, no. 12, pp. 2022–2023, Dec 1966.
- [77] Y. Konishi, "Lumped element Y circulator," *IEEE Transactions on Microwave Theory and Techniques*, vol. 13, no. 6, pp. 852–864, Nov 1965.
- [78] R. H. Knerr, C. E. Barnes, and F. Bosch, "A compact broad-band thin-film lumped-element L-band circulator," *IEEE Transactions on Microwave Theory and Techniques*, vol. 18, no. 12, pp. 1100–1108, Dec 1970.
- [79] T. Miyoshi and S. Miyauchi, "The design of planar circulators for wide-band operation," *IEEE Transactions on Microwave Theory and Techniques*, vol. 28, no. 3, pp. 210–214, Mar 1980.
- [80] D. C. Webb, "Design and fabrication of low-cost ferrite circulators," in *the 25th European Microwave Conference*, vol. 2, Sept 1995, pp. 1191–1200.
- [81] A. M. Hussein, M. M. Ibrahim, and S. E. Youssef, "Impedance matrix formulation of stripline circulators," *Canadian Electrical Engineering Journal*, vol. 5, no. 3, pp. 9–11, July 1980.
- [82] G. Bittar and G. Veszely, "A general equivalent network of the input impedance of symmetric three-port circulators (short paper)," *IEEE Transactions on Microwave Theory and Techniques*, vol. 28, no. 7, pp. 807–808, Jul 1980.

- [83] U. Goebel and C. Schiebllich, "A unified equivalent circuit representation for H- and E-Plane junction circulators," in *13th European Microwave Conference*, Sept 1983, pp. 803–808.
- [84] N. Mohsenian, T. J. Delph, and D. M. Bolle, "Finite element analysis applied to gyroelectrically loaded waveguiding structures," in *IEEE MTT-S International Microwave Symposium Digest*, June 1985, pp. 631–634.
- [85] H. S. Newman and C. M. Krowne, "Analysis of ferrite circulators by 2-D finite-element and recursive green's function techniques," *IEEE Transactions on Microwave Theory and Techniques*, vol. 46, no. 2, pp. 167–177, Feb 1998.
- [86] J. Lenge, G. Steinwachs, I. Gieseke, and D. Schulz, "FDTD modeling and analysis of microstrip circulators," in *the 28th European Microwave Conference*, vol. 2, Oct 1998, pp. 289–294.
- [87] W. D'Orazio and K. Wu, "Substrate-integrated-waveguide circulators suitable for millimeter-wave integration," *IEEE Transactions on Microwave Theory and Techniques*, vol. 54, no. 10, pp. 3675–3680, Oct 2006.
- [88] X. Jiang, C. J. You, and Z. Shao, "A compact x-band circulator with embedded feed line based on substrate integrated waveguide," in *International Conference on Computational Problem-solving (ICCP)*, Oct 2013, pp. 58–60.
- [89] L. E. Davis, K. Xie, B. J. Climer, K. D. Newsome, and N. E. Priestley, "Design and measurement of ferrite coupled line circulators," in *IEEE MTT-S International Microwave Symposium Digest*, vol. 3, June 1999, pp. 1153–1156 vol.3.
- [90] L. E. Davis and R. Sloan, "Semiconductor junction circulators," in *IEEE MTT-S International Microwave Symposium Digest*, June 1993, pp. 483–486 vol.1.

- [91] D. Kother, B. Hopf, T. Sporkmann, I. Wolff, and S. Koblowski, "MMIC circulators covering the frequency range from L- to W-band," in *25th European Microwave Conference*, vol. 2, Sept 1995, pp. 1186–1190.
- [92] D. K. Linkhart, *Microwave Circulator Design*. Artech House Inc., 1989.
- [93] J. Helszajn, *The Stripline Circulators: Theory and Practice*. Wiley-IEEE Press, 2008.
- [94] F. Horner, T. Taylor, R. Dunsmuir, J. Lamb, and W. Jackson, "Resonance methods of dielectric measurement at centimetre wavelengths," vol. 93, no. 63, pp. 149–150, March 1946.
- [95] K. Foulds, "Resonant-cavity measurements of the relative permittivity of a D.C. discharge," *Proceedings of the IEE - Part C: Monographs*, vol. 102, no. 2, pp. 203–216, September 1955.
- [96] K. Champlin and R. Krongard, "The measurement of conductivity and permittivity of semiconductor spheres by an extension of the cavity perturbation method," *IRE Transactions on Microwave Theory and Techniques*, vol. 9, no. 6, pp. 545–551, November 1961.
- [97] P. Clarricoats, "A new waveguide method for measuring permittivity," *Proceedings of the IEE - Part B: Electronic and Communication Engineering*, vol. 109, no. 23, pp. 858–862, 1962.
- [98] S. Roberts and A. Von Hippel, "A new method for measuring dielectric constant and loss in the range of centimeter waves," *Journal of Applied Physics*, vol. 17, no. 7, 1946.

- [99] P. Clarricoats, "A new waveguide method for measuring the permittivity of dielectric slabs," *Proceedings of the IEE - Part C: Monographs*, vol. 109, no. 16, pp. 401–405, September 1962.
- [100] B. Bianco and M. Parodi, "Measurement of the effective relative permittivities of microstrip," *Electronics Letters*, vol. 11, no. 3, pp. 71–72, February 1975.
- [101] E. Mueller, "Measurement of the effective relative permittivity of unshielded coplanar waveguides," *Electronics Letters*, vol. 13, no. 24, pp. 729–730, November 1977.
- [102] M. Afsar, J. Chamberlain, and G. W. Chantry, "High-precision dielectric measurements on liquids and solids at millimeter and submillimeter wavelengths," *IEEE Transactions on Instrumentation and Measurement*, vol. 25, no. 4, pp. 290–294, Dec 1976.
- [103] A. Talai, F. Steinheusser, A. Bittner, U. Schmid, R. Weigel, and A. Koelpin, "A permittivity characterization method by detuned ring-resonators for bulk materials up to 110 GHz," in *44th European Microwave Conference (EuMC)*, Oct 2014, pp. 124–127.
- [104] N. Das, S. Voda, and D. M. Pozar, "Two methods for the measurement of substrate dielectric constant," *IEEE Transactions on Microwave Theory and Techniques*, vol. 35, no. 7, pp. 636–642, Jul 1987.
- [105] B. Ivsic, D. Bonafacic, and J. Bartolic, "Considerations on embroidered textile antennas for wearable applications," *IEEE Antennas and Wireless Propagation Letters*, vol. 12, pp. 1708–1711, 2013.
- [106] N. Rais, P. Soh, F. Malek, S. Ahmad, N. Hashim, and P. Hall, "A review of wearable antenna," in *Loughborough Antennas Propagation Conference, LAPC*, Nov 2009, pp. 225–228.

- [107] M. Scarpello, I. Kazani, C. Hertleer, H. Rogier, and D. Vande Ginste, "Stability and efficiency of screen-printed wearable and washable antennas," *IEEE Antennas and Wireless Propagation Letters*, vol. 11, pp. 838–841, 2012.
- [108] K. Koski, L. Sydanheimo, Y. Rahmat-Samii, and L. Ukkonen, "Fundamental characteristics of electro-textiles in wearable UHF RFID patch antennas for body-centric sensing systems," *IEEE Transactions on Antennas and Propagation*, vol. 62, no. 12, pp. 6454–6462, Dec 2014.
- [109] M. M. Tahseen and A. Kishk, "Wideband textile-based conformal antennas for WLAN band using conductive thread," in *EUCAP Conference, Davos*, 2016.
- [110] A. Zaman and P.-S. Kildal, "Slot antenna in ridge gap waveguide technology," in *6th European Conference on Antennas and Propagation (EUCAP)*, March 2012, pp. 3243–3244.
- [111] M. AlSharkawy and A. Kishk, "Frequency scanning long slots array in a ridge gap waveguide technology," in *IEEE Conference on Antenna Measurements Applications (CAMA)*, Nov 2014, pp. 1–2.
- [112] M. Al Sharkawy and A. Kishk, "Design of waveguide to ridge gap waveguide transition using probe excitation," in *8th European Conference on Antennas and Propagation (EuCAP)*, April 2014, pp. 946–949.